# Fretting Fatigue of Ti-6Al-4V: Experimental Characterization and Simple Design Parameter

A Thesis
Presented to
The Academic Faculty

by

Neil Robert Lovrich

In Partial Fulfillment
of the Requirements for the Degree
Master of Science in Mechanical Engineering

Georgia Institute of Technology

July 2004

Fretting Fatigue of Ti-6Al-4V: Experimental Characterization and Simple Design Parameter

Approved:

Richard W. Neu, Chairman

W. Steven Johnson

David L. McDowell

Date Approved: June 30, 2004

## ACKNOWLEGEMENT

There are many people that I would like to thank for making this all possible. Foremost, I must thank my advisor Dr. Richard Neu for all his help and assistance throughout this project. His guidance has been remarkable and I am truly grateful for all of his hard work. I also appreciate the contributions from my other committee members, Dr. W. Steven Johnson and Dr. David McDowell. I would like to thank former students John Pape, Jon Wallace, and Dana Swalla for laying the groundwork for the fretting fatigue program here at Georgia Institute of Technology. I would also like to thank the members of the Mechanics of Materials Research Group for their support, assistance, and friendship. I must also thank my family, especially my parents, for their constant encouragement and for always believing in me. Finally, I would like to express my appreciation to Research Applications, Inc for their support of this project.

## TABLE OF CONTENTS

## LIST OF TABLES

## LIST OF FIGURES

## SUMMARY

Fretting fatigue occurs when there is a small amplitude oscillatory movement between two contacting surfaces while the bodies are undergoing fatigue loading. Fretting fatigue conditions can substantially reduce the fatigue life of a component. Many engineering components such as Ti-6Al-4V gas turbine engine disks in military aircraft commonly experience fretting fatigue conditions that can potentially lead to catastrophic failure of critical components.

The aim of this study is to characterize the behavior of Ti-6Al-4V under fretting fatigue conditions. Experiments are performed to analyze the influence of stress amplitude, stress ratio, and contact geometry. The effect of surface treatments such as low plasticity burnishing on the fretting fatigue life is also explored. The experimental results are being used to validate a proposed crack nucleation life prediction model. The proposed model utilizes a crack nucleation parameter H that is based on the strength of the singular stress field at the contact boundary. An advantage of this singular parameter is that neither a coefficient of friction nor the location of the stick/slip boundary needs to be determined. These two parameters are often difficult to define with certainty *a priori*. H is also independent of geometry making it well suited for use as a design parameter for designing structural joints and other fitted connections between components.

# CHAPTER I

# INTRODUCTION

Fatigue is the term that is used to describe the damage and failure of engineering materials that undergo cyclic loading. A material's strength under fatigue is often much lower than its strength under monotonic loading conditions. Fretting is the term that is used to describe the condition where materials in contact experience small amplitude oscillatory movements in relation to each other. When these conditions are present individually, they are fairly well understood and can be properly accounted for in design. However, the interaction of fretting and fatigue loading results in a dramatic decrease in strength. This condition, appropriately called fretting fatigue, is less understood and is often responsible for premature failure of engineering components.

Fretting fatigue is a complicated phenomenon that is affected by the interaction of a number of factors. These factors include relative slip amplitude, normal and tangential stresses at the contact, bulk fatigue stresses, microstructure, and surface conditions of the materials in contact. Due to severity and incomplete understanding of the factors in fretting fatigue, frequent inspection intervals are necessary to prevent failures due to fretting fatigue. These service measures are especially important for critical aircraft components such as gas turbine engine disks, a place where fretting fatigue is known to occur.

Surface treatments have been shown to increase fretting fatigue life of components. They work by causing a layer of compressive stresses to form in the surface. This layer resists crack initiation, thus, extending the life of a component. A

relatively new process that has been especially effective in improving fretting fatigue life is low plasticity burnishing (LPB). It is desired to quantify the resistance to fretting fatigue that this treatment provides to a material.

This investigation is centered on characterizing the fretting fatigue behavior of Ti-6Al-4V, due to its common application as a material in aircraft gas turbine engine disks. Experimental data is used to help create models that can predict fretting fatigue crack nucleation. A model that predicts crack nucleation based on the strength of the singular stress field at the contact boundary is being explored due to its unique advantages. This model uses a parameter that requires neither a coefficient of friction nor the location of the stick/slip boundary to be determined. Both of these parameters are often difficult to define without investigation. The goal of the experimental aspect of this research is to validate such a model. This model could then be used as a design parameter for designing structural joints and other fitted connections between components.

# CHAPTER II

# LITERATURE REVIEW

## 2.1 Overview

Fretting is a small amplitude oscillatory movement which occurs between two contacting surfaces. This oscillatory movement often results in the formation of oxide debris and, thus, is called 'fretting wear' or 'fretting corrosion'. In many cases, the cause of this movement is due to one of the members being placed under cyclic fatigue loading. The situation where a fatigue loading is present is much more destructive and is called 'fretting fatigue' (Waterhouse, 1992). Fretting fatigue is a widespread problem which has detrimental affects on a broad range of engineering components.

Waterhouse (1992) provided a summary of the history of fretting fatigue. Eden, Rose, and Cunningham were the first to report evidence of fretting in 1911. They noticed brown oxide debris formed in the steel grips of their fatigue machine. In 1927, Tomlinson was the first to actually study the fretting process. He designed machines that produced small amplitude rotational movement between two materials. He was able to conclude that damage could be caused by relative movements as small as 125 nm. In 1941, Warlow-Davies became the first to examine the effect that fretting could have on fatigue properties. He performed his tests by first applying fretting damage to a specimen and then conducted fatigue tests on the same specimen. He discovered a decrease of fatigue strength by 13-17%. Later work by McDowell studied the simultaneous action of fretting and fatigue. His work suggested that fretting fatigue was much more dangerous, reducing the strength by factors of 2-5.

It has been well documented that there are many contributing factors that combine to influence fretting fatigue damage. Some of these factors include (Waterhouse, 1992; Hills and Nowell, 1994; Waterhouse and Lindley, 1994; Fouvry et al., 1996; and Lindley, 1997):

- cyclic stress amplitude
- cyclic slip displacement amplitude
- cyclic frequency, waveform, and hold periods
- normal contact pressure
- coefficient of friction
- environmental conditions
- residual stresses in the contacting surfaces caused by prior surface modification techniques
- microstructural changes and phase transformations

Fretting fatigue failures are known to occur in many engineering applications. Failures are of great concern in steam or gas turbine engines. They often occur in the seating of a turbine disk on the drive shaft in land-based turbines or in the dove-tail section where the blade attaches to the disk in aircraft engines. Another common failure location is in the joints of fatigue loaded structures, such as in rivets of aircraft wings or in splines and keyways of shafts in couplings. Some other examples include cables, ropes, and bio-implant devices (Suresh, 1998).

## 2.2 Mechanics of Fretting Fatigue

The primary area of concern in fretting fatigue is the region of contact between two bodies. Figure 2.1 shows two bodies in contact under an applied normal force, $P$, and tangential force, $Q$. The dotted lines outline the region of material that would overlap if the two bodies could go through each other.

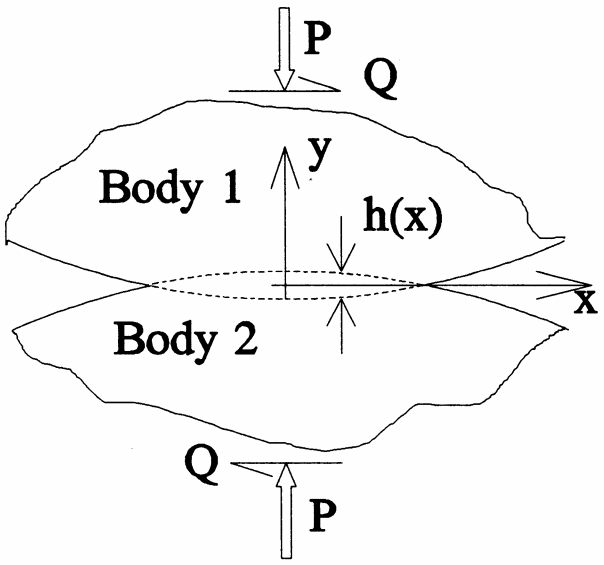


Figure 2.1: Contact between two elastically deformable bodies under a normal load, P, and a tangential force, Q (Hills and Nowell, 1994).

The case of two parallel, elastic cylinders can be reduced to a plane solution. Hertzian contact theory (Johnson, 1985) can be used to express the contact half width, $a$, as

$$a = \left( \frac{4R}{\pi E^*} \cdot \frac{P}{l} \right)^{1/2} \tag{2.1}$$

where $P$ is the normal load, $l$ is the length of the cross section in the z-direction, $R$ is an effective radius defined as

$$R = \left( \frac{1}{R_1} + \frac{1}{R_2} \right)^{-1} \tag{2.2}$$

where $R_1$ and $R_2$ are the radii of the cylinders, and $E^*$ is the effective elastic constant defined as

$$E^* = \left( \frac{1-\nu_1^2}{E_1} + \frac{1-\nu_2^2}{E_2} \right)^{-1} \tag{2.3}$$

The Hertz pressure distribution is given by

$$p(x) = \frac{p_0}{a}\sqrt{a^2 - x^2} \tag{2.4}$$

where the maximum contact pressure, $p_0$, is represented by

$$p_0 = \frac{2P}{\pi a l} \tag{2.5}$$

where $P$ is the normal load, $l$ is the length of the cross section in the z-direction, and $a$ is half the width of the contact area.

When a tangential force, $Q$, is applied, a shear traction distribution is generated at the interface. It is assumed that the bodies are elastically the same and that no slip occurs (ideally stick). Two bodies that are in a stick condition have no relative motion. Figure 2.2 shows two cylinders in contact under an applied normal force, $P$, and tangential force, $Q$.

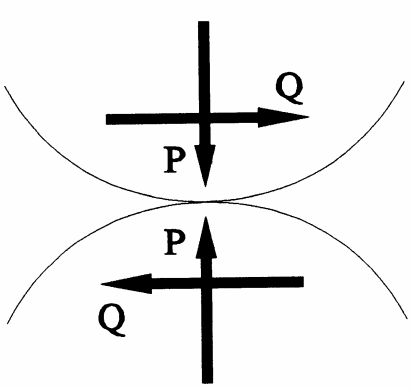


Figure 2.2: Contact of two cylindrical bodies under a normal force, P, and a tangential force, Q (Hills and Nowell, 1994).

The shear traction, $q$, is given as (Hills and Nowell, 1994)

$$q(x) = \frac{1}{\pi\sqrt{a^2 - x^2}} \cdot \frac{Q}{l} \tag{2.6}$$

and is shown plotted in Figure 2.3 (a). At $x = \pm a$, the shear traction goes to infinity. Thus, the stress field is singular at these points, often called the edge of contact.

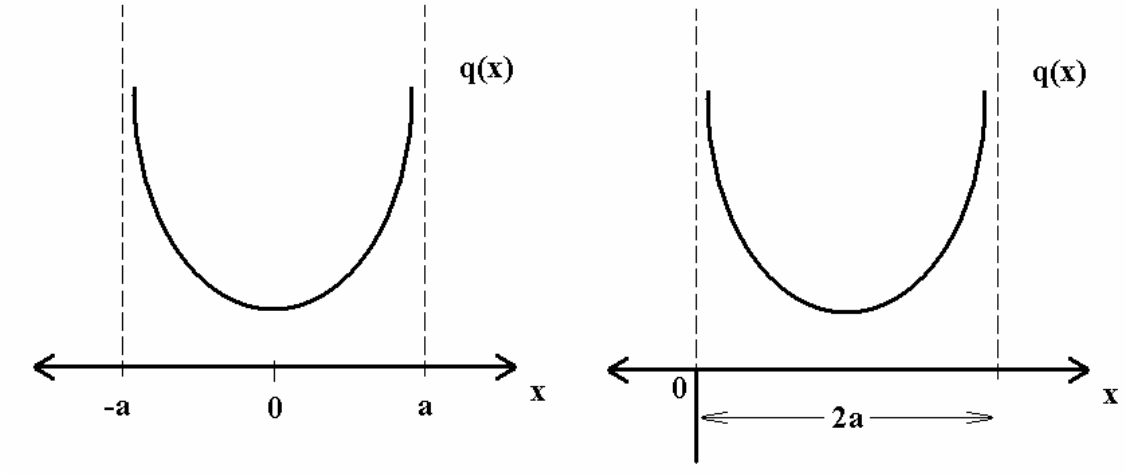


(a) (b)

Figure 2.3: Shear tractions for two cylinders in contact under complete stick (a) with center point zeroed on x-axis and (b) with end point starting at zero.

Later, we will be interested in the strength of the singular points. For convenience, the origin of the coordinate system is shifted as shown in Figure 2.3 (b) so that the origin is at the point of the singularity. The shear traction distribution for stick conditions becomes

$$q(x) = \frac{1}{\pi\sqrt{a^2 - (x-a)^2}} \cdot \frac{Q}{l} \tag{2.7}$$

which can be reduced to

$$q(x) = \frac{1}{\pi\sqrt{2ax - x^2}} \cdot \frac{Q}{l} \tag{2.8}$$

Under gross sliding conditions, the shear traction distribution is

$$q(x) = \mu p(x) \tag{2.9}$$

where the coefficient of friction, $\mu$, can be found from the forces transmitted,

$$\mu = \frac{Q}{P} \tag{2.10}$$

In regions where $Q < \mu P$, partial slip or stick conditions are present at the contact interface. Theoretically, stick is only possible if $Q = 0$ or $\mu = \infty$, though near stick conditions that are described well by the stick solution ($\mu = \infty$) are possible. Two bodies that are in partial slip have regions of both stick and slip along the interface existing simultaneously. The solution of the tractions along the interface is given by the classical Cattaneo-Mindlin (1949) problem. To obtain this solution, it is assumed that a slip zone exists at the edge of contact where shear traction goes to infinity. The boundary between slip and stick is defined at $x = \pm c$. Thus, the stick zone is represented in Figure 2.4 as the region extending from -c to c, while the area of contact extends from -a to a. Assuming q(x) has a similar form as in completely stick and gross slip conditions, and ensuring

tangential force is in equilibrium with the shear traction, a normalized stick zone can be estimated (Hills and Nowell, 1994)

$$\frac{c}{a} = \sqrt{1 - \left|\frac{Q}{\mu P}\right|} \tag{2.11}$$

With the shear traction distribution shown in Figure 2.5 for different $\mu$, this is a very valuable formula (Johnson, 1985; Hills and Nowell, 1994). It can obviously be used to find the ratio of the width of the stick zone to the width of the contact area for a known coefficient of friction. However, after determining the size of the stick and slip regions by examining the fretting scars of a specimen, Equation 2.11 can also be used to estimate the coefficient of friction in the slip regions by solving for $\mu$. Figure 2.5 illustrates how increasing the tangential force, $Q$, for a constant $\mu$ and $P$, will cause the stick region to get smaller and smaller until gross sliding occurs at $\frac{Q}{\mu P} = 1$.

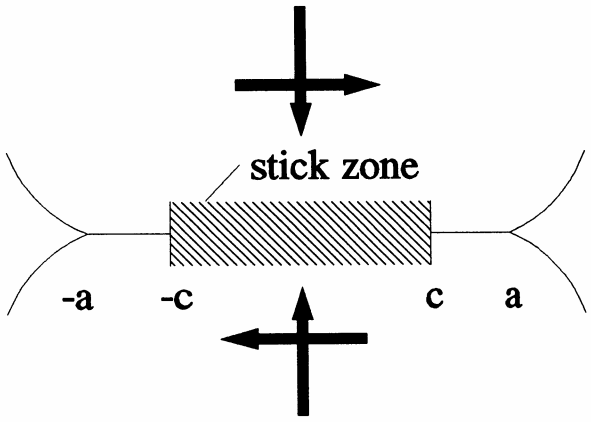


Figure 2.4: Stick and slip regions for the contact of cylinders in partial slip (Hills and Nowell, 1994).

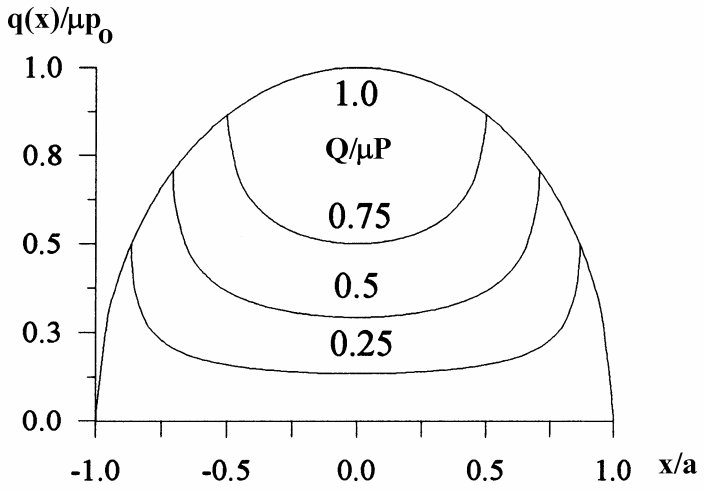


Figure 2.5: Shear traction distributions for a range of values of tangential force, Q (Hills and Nowell, 1994).

During fretting fatigue testing, the tangential force varies cyclically. Figure 2.6 shows the dependence of the shear tractions on the tangential loading during different points in a cycle. The shaded region in Figure 2.6 (b) represents the stick zone. Initially, the tangential force, Q, increases from 0 to $Q_{max}$ (point A in Figure 2.6). At point B (Figure 2.6), the load has decreased infinitesimally from its maximum value. The change of direction causes instantaneous stick over the entire contact width. As Q continues to decrease to point C in Figure 2.6, the normal pressure is insufficient to prevent relative slip, leading to reverse slip at the edges of the contact. At point D in Figure 2.6, the tangential force has been fully removed, creating additional reverse slip as required for self-equilibrium of the shear tractions. Finally, at point E in Figure 2.6 when the load is fully reversed and $Q = -Q_{max}$, the shear traction distribution is also fully reversed (Hills and Nowell, 1994).

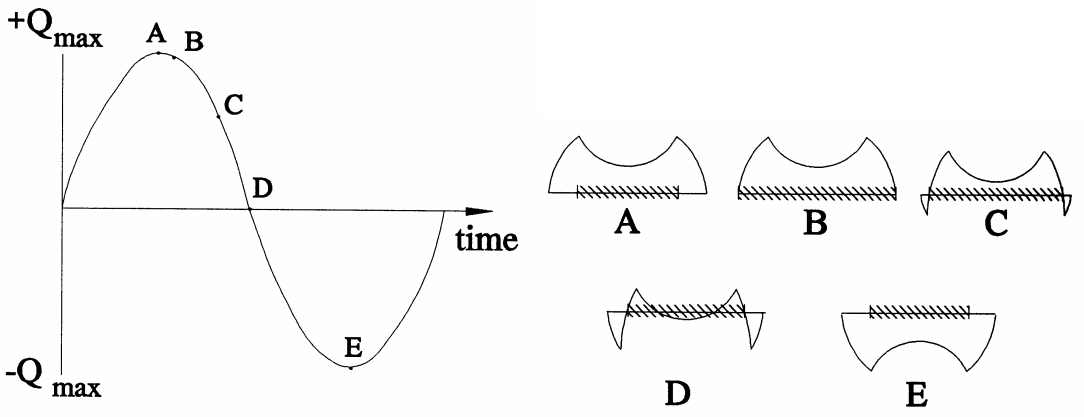


(a) (b)

Figure 2.6: Tangential loading history and shear tractions during the fretting fatigue loading cycle (Hills and Nowell, 1994).

Typical fretting fatigue conditions also include the presence of a bulk stress to one of the bodies. Figure 2.7 shows a schematic of a typical fretting fatigue condition with an applied bulk stress, $\sigma$. The bulk stress causes the stick zone to shift its position as shown in Figure 2.8. The shifting of the position of the stick zone produces an increase of the in-plane stress component, $\sigma_{xx}$, at the trailing edge of the contact. This is the edge of the larger slip region. If larger values of bulk stress are applied, one edge of the stick zone approaches the edge of contact and if the load is increased enough, reverse slip will take place at one edge of contact as shown in Figure 2.8 (b).

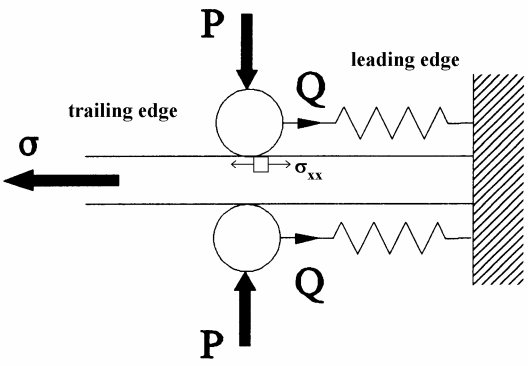


Figure 2.7: Fretting fatigue experimental configuration showing bulk applied stress and normal and tangential forces from the contacting bodies for cylindrical pads on a flat specimen (Hills and Nowell, 1994).

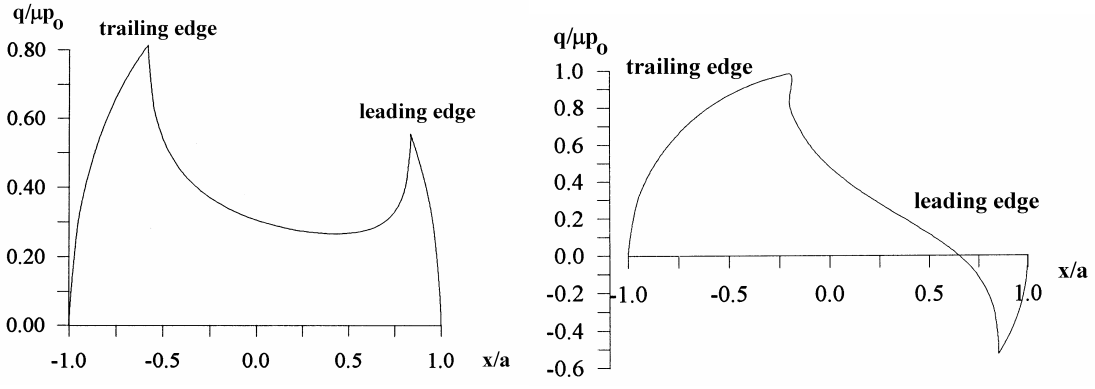


(a) (b)

Figure 2.8: Shear traction distributions caused by the application of a bulk tension together with a tangential force for (a) medium ($\frac{Q}{\mu P} = 0.5$, $\frac{\sigma}{\mu p_0} = 0.5$) and (b) high ($\frac{Q}{\mu P} = 0.5$, $\frac{\sigma}{\mu p_0} = 2.0$) bulk tension (Hills and Nowell, 1994).

## 2.3 Fretting Fatigue in Titanium Alloys

Several factors can affect crack nucleation under fretting fatigue. These factors can be grouped into three categories: the loading conditions, the surface contact conditions, and the operating environment. The relevant loading conditions include the normal contact pressure, the contact slip amplitude, and the bulk applied stress amplitude and mean stress. The surface contact conditions include the chemical composition of the contact region, surface roughness, residual surface stresses, and any coatings or lubricants on the surface (Wallace, 2001).

### 2.3.1 Bulk Loading Effects

Fretting fatigue can cause substantial decreases in fatigue life as compared to smooth specimen fatigue. For Ti-6Al-4V, the knock down factor is often greater than 50%, as shown in Figure 2.9. The effect is also strongest in the high cycle regime. The relative slip conditions can also affect fretting fatigue life. Figure 2.10 compares the effects of gross nominal relative slip and partial slip conditions. The United Technology Research Center (UTRC) fretting fatigue data was in gross slip which led to longer lives compared to the Purdue and Georgia Tech tests which had a smaller amount of relative slip, causing them to be in a partial slip condition. In addition to the tests having different relative slip conditions, the tests also used different contact geometries. The UTRC tests were conducted with flat pads on flat specimens, and the Purdue tests were conducted with cylindrical pads on flat specimens. The cylindrical on flat condition of the Purdue tests led to a higher maximum contact pressure and, thus, a more critical partial slip condition. The Georgia Tech tests were conducted with a flat and cylindrical pad simultaneously on a flat specimen. However, in all cases the dominant fatigue crack

nucleated at one of the cylindrical contacts suggesting that a more critical condition was present at the cylindrical contacts (Wallace, 2001).

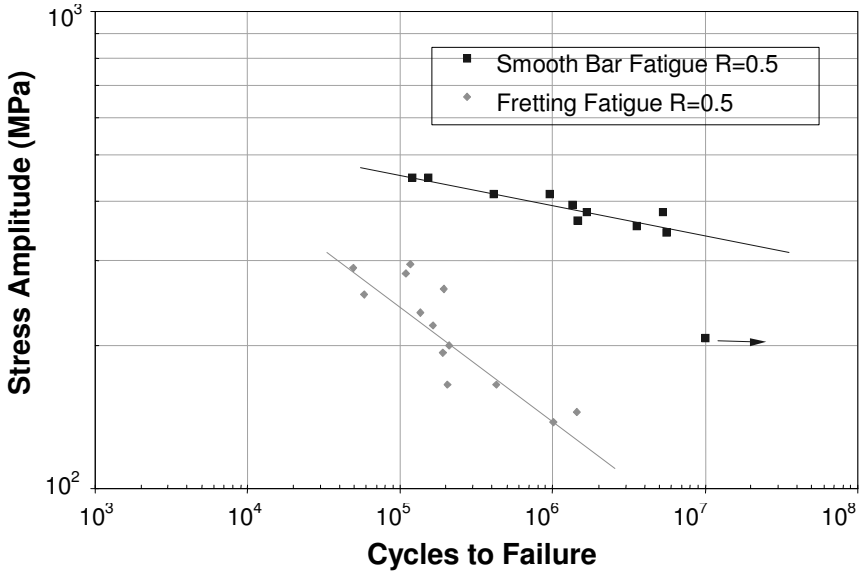


Figure 2.9: Comparison of fretting fatigue lives versus smooth non-fretting fatigue lives for Ti-6Al-4V (f = 20 Hz, flat contact with pressure = 200 MPa) (Anton, 1999).

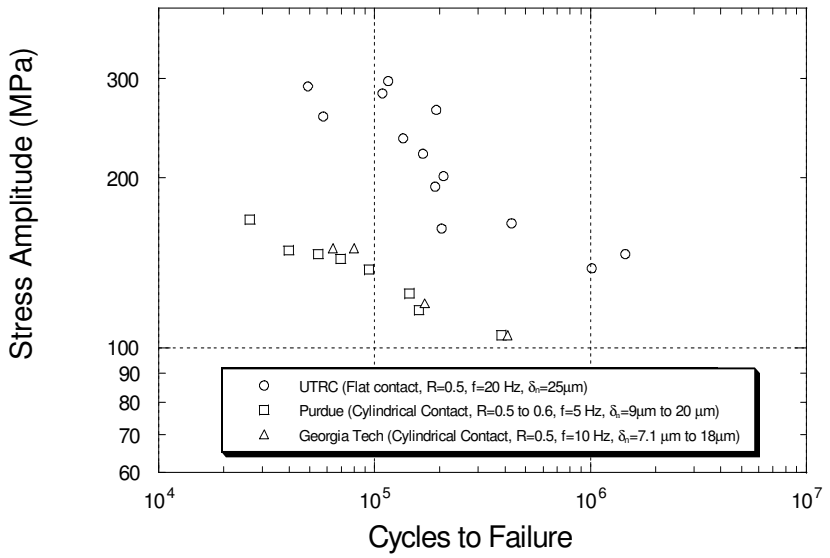


Figure 2.10: Effect of relative slip conditions on fretting fatigue lives (Anton, 1999; Farris et al., 2000; Wallace, 2001).

### 2.3.2 Environmental Effects

Wharton and Waterhouse (1979) have shown that environmental conditions can have substantial effects on fretting fatigue lives. They performed fretting fatigue tests on Ti-6Al-4V in environments of laboratory air, 1% NaCl solution, dried liquid paraffin, dry deoxidized argon, and humidified argon. The general trends are illustrated in Figure 2.11. The corrosive environments can be beneficial through the formation of a corrosive layer that acts as a solid lubricant. This solid lubricant offers some protection by hindering the initiation of fretting fatigue cracks due to the reduction in frictional force range, which is due to reduction in coefficient of friction, leading to higher fatigue strengths at $10^7$ cycles. However, at high stresses and short lives, the corrosive environment negatively affected the crack propagation rates resulting in shorter fatigue lives. Overall, the effect of corrosive environments is considerably smaller than fretting itself.

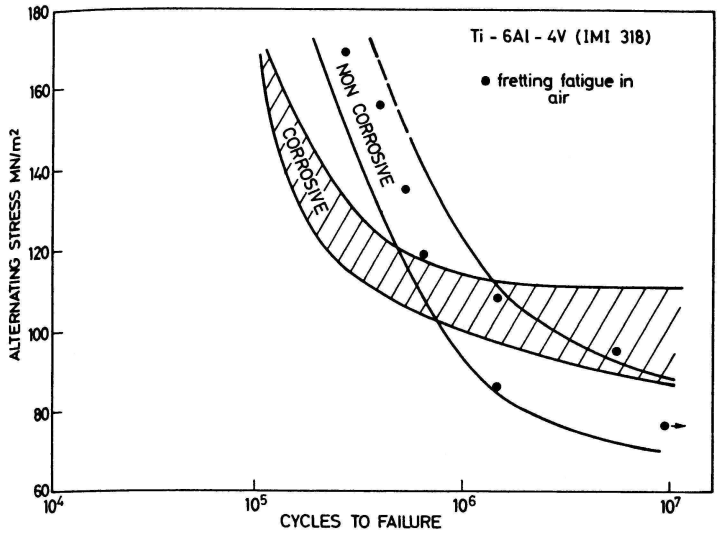


Figure 2.11: Comparison of fretting fatigue of Ti-6Al-4V under non-corrosive and corrosive environments consisting of NaCl, humid argon, dry argon, and parafin (f = 50 Hz, mean stress = 247 MN/m$^2$, flat contact with pressure of 32 MPa) (Wharton and Waterhouse, 1980).

### 2.3.3 Influence of Contact Pressure

A reasonable amount of research has been performed on the influence of contact pressure. Lutynski et al. (1982) concluded that a variation in the normal pressure has relatively little effect on fatigue life for the range considered in this test program. However, at very low contact pressures, the fatigue life decreases drastically as contact pressure increases, but the fatigue life does reach a minimum at a relatively low pressure of 20 MPa (Nakazawa et al., 1992; Hoeppner and Goss, 1974). Further increase in contact pressure has very little effect on the fatigue life as shown in Figure 2.12. Wallace's (2001) work with Ti-6Al-4V also supported this trend for contact pressures within this range. He found that even a substantial increase of contact pressure of 69 MPa to 128 MPa has a very insignificant affect on fretting fatigue life. Work done by Iyer and Mall (1999) suggests that an additional regime may exist at exceptionally high contact pressures in the range of 300 to 700 MPa. In this regime, the fretting fatigue life again decreases as contact pressure increases.

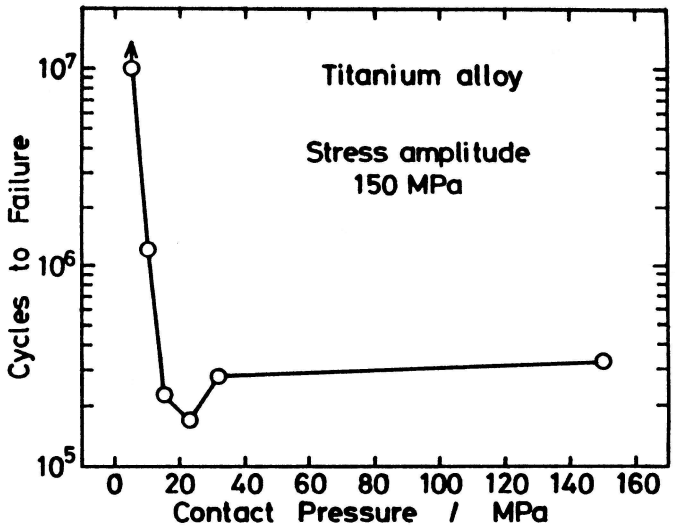


Figure 2.12: Effect of contact pressure on the fretting fatigue life of Ti-6Al-4V (f = 20 Hz, $\sigma_a$ = 150 MPa, R = 0.1, with flat contact geometry) (Nakazawa et al., 1992).

### 2.3.4 Experimental Monitoring of Ti-6Al-4V

In fretting fatigue experiments, the relative slip between contacting surfaces is a parameter commonly used to monitor the fretting conditions. Figure 2.13 shows the typical effect that relative slip has on the wear and fatigue life of fretted components. Notice in the figure that the wear volume loss increases monotonically with the slip amplitude and it does this at a higher rate under gross slip conditions. However, the fatigue life is most severely affected in the partial slip region which is where the fatigue cracks are nucleated at the contact surface when repeated sliding occurs. Under gross sliding, the rapid removal of material can cause the cracks to disappear, thus causing an increase in fatigue life. Experiments performed by Van Stone et al. (1999) and characterized by Glaeser and Lawless (2001) on Ti-6Al-4V showed that nominal relative slip values well above 30 μm result in a gross slip or fretting wear condition with longer lives. Additionally, nominal relative slip ranges well below 3 μm cause a stick condition which also leads to longer fatigue lives. This behavior correlated well with the trends illustrated in Figure 2.13.

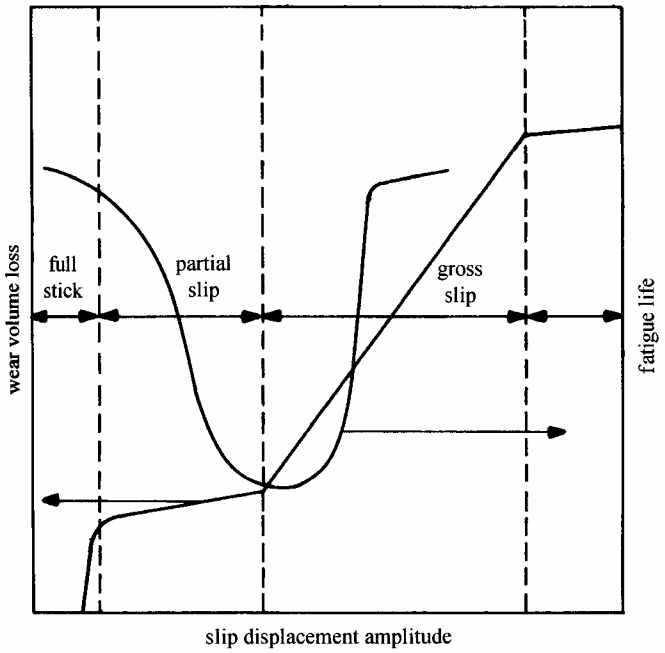


Figure 2.13: Schematic representing the effect of relative slip amplitude on fretting wear and fretting fatigue life (Suresh, 1998, adapted from Vingsbo and Soderberg, 1988).

Prior studies on Ti-6Al-4V on Ti-6Al-4V fretting have reported values for the coefficient of friction between 0.5 and 0.95 (Anton, 1999; Harish et al., 1999). This fairly large range of values can be attributed to variable surface conditions such as surface roughness or environment, as well as the method for experimentally monitoring the frictional force. Wallace (2001) also reported values within this range. He calculated values for the coefficient of friction ranging from 0.74 to 0.88.

Pape (1998) and Wallace (2001) monitored the frictional force range during fretting fatigue testing. During the majority of the life of each of their tests, the frictional force range remained fairly constant. However, toward the end of each test, there was a characteristic drop in the frictional force range caused by the growth of cracks. This was due to the fact that as a crack propagates from the edge of a fretting pad, the load in the specimen is transferred around the crack. This causes a reduction in load near the area of

contact, and a smaller amount of load is then transferred by the frictional forces through the pads. Thus, they defined the cycles to crack initiation as the amount of cycles required for the rapid decline in frictional force range to occur as shown in Figure 2.14. This type of decline typically indicated the growth of a crack of a length in the range of 0.5 to 1 mm. This definition for cycles to crack initiation is also used in this study.

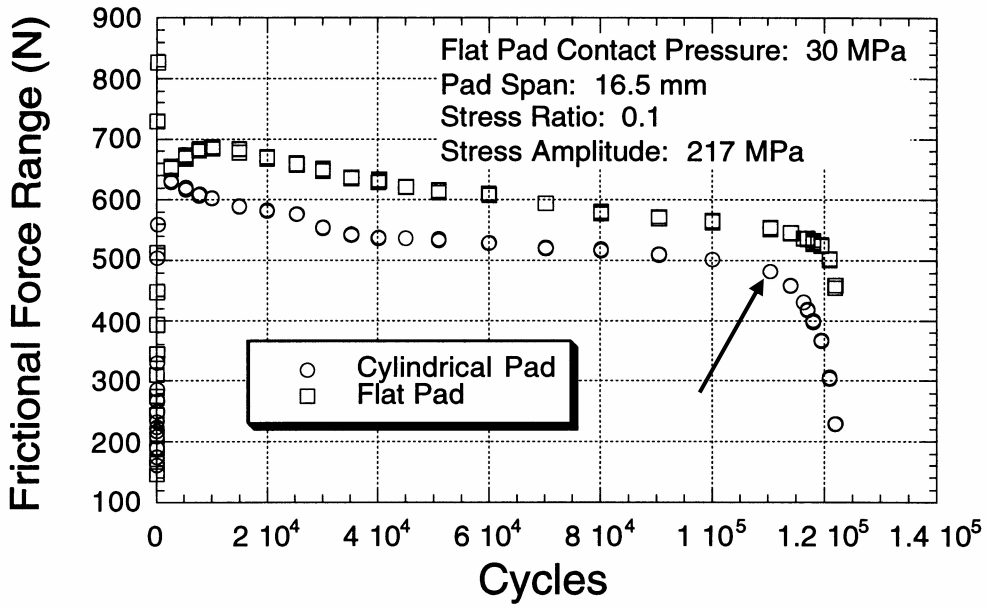


Figure 2.14: Plot of frictional force range vs. cycles for a fretting fatigue test (Pape, 1998). The cycles to crack initiation for this test is 110,000 as indicated by the arrow.

## 2.4 Microstructural Properties of Ti-6Al-4V

Titanium is considered an allotropic element since it can exist in more than one crystallographic state. Pure titanium exists as a hexagonal close-packed (HCP) crystalline structure, called the alpha phase. For Ti-6Al-4V, at temperatures above 980ºC, the alpha phase transforms into a body-centered cubic (BCC) crystalline structure, called the beta phase. Alloying elements can stabilize the beta phase so that both alpha and beta can exist at room temperature. In Ti-6Al-4V, the aluminum serves as the alpha stabilizer and the vanadium stabilizes the beta phase (Wallace, 2001).

The alpha and beta phases in a material can have significant affect on the properties of an alloy. Alpha alloys cannot be strengthened by heat treatment. However, their resistance to heat causes them to have good weldability. In general, they have poorer forgeability and more limited forging temperature ranges than alpha-beta or beta alloys. Beta alloys have high hardenability and excellent forgeability. The fracture toughness of an aged beta alloy is normally higher than that of an alpha-beta alloy of similar yield strength. However, beta alloys also have higher density, lower creep strength, lower tensile ductility, and lower weldability. Since Ti-6Al-4V consists of an alpha-beta microstructure, its properties can be optimized for a specific application by utilizing the right combination of the alpha and beta phases. Figure 2.15 shows six possible microstructures of Ti-6Al-4V (Donachie, 2000).

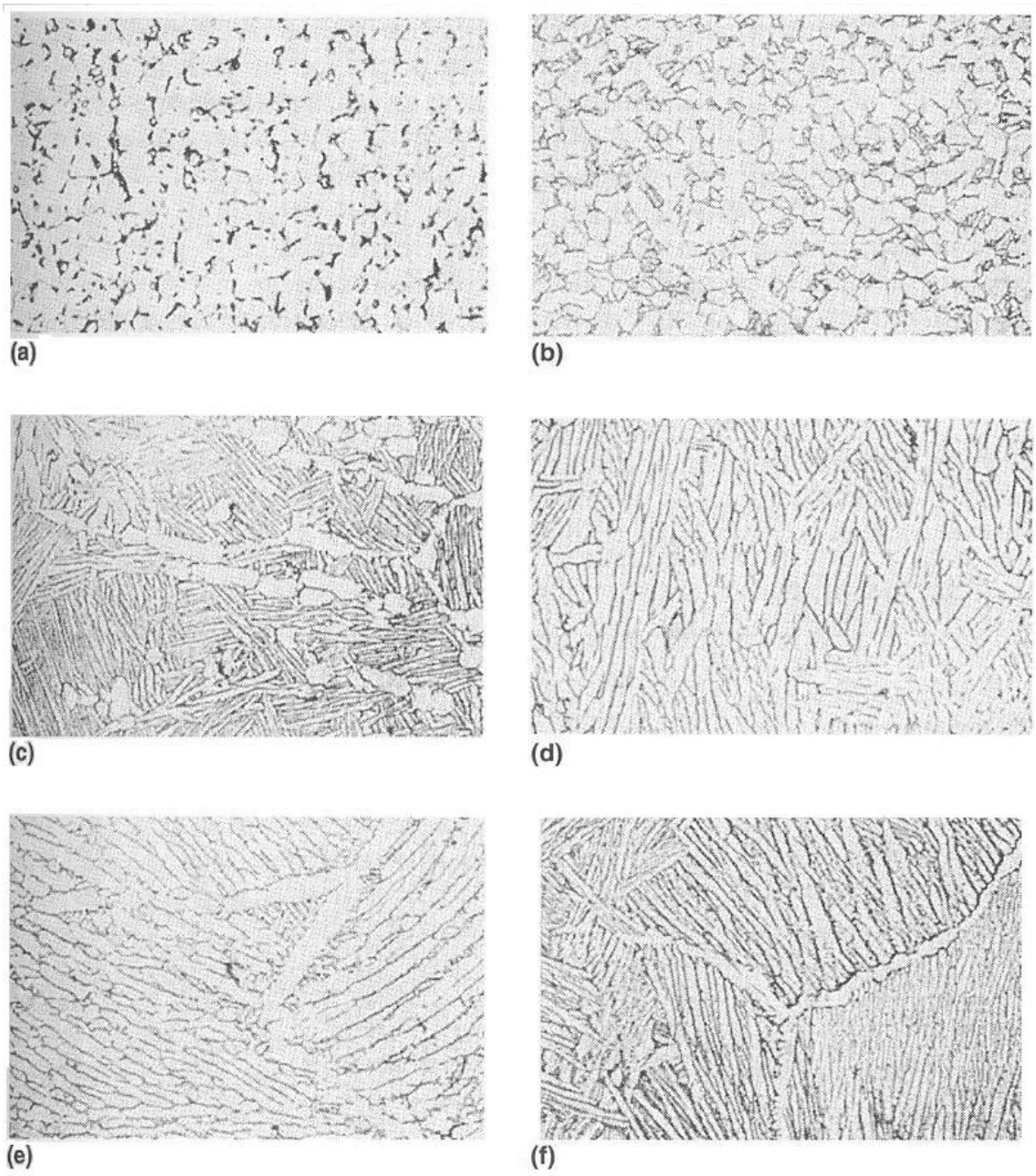


Figure 2.15: Microstructure of Ti-6Al-4V in representative metallurgical conditions. (a) Equiaxed alpha and a small amount of intergranular beta. (b) Equiaxed and acicular alpha and a small amount of intergranular beta. (c) Equiaxed alpha in an acicular alpha (transformed beta) matrix. (d) Small amount of equiaxed alpha in an acicular alpha (transformed beta) matrix. (e) Plate-like acicular alpha (transformed beta); alpha at prior beta grain boundaries. (f) Blocky and plate-like acicular alpha (transformed beta); alpha at prior beta grain boundaries.

Microstructure has a strong influence on high cycle fatigue strength. Figure 2.16 shows the differences of fatigue strength for bi-modal, fine equiaxed, fine lamellar, coarse equiaxed, and coarse lamellar microstructures. The range of fatigue strength varies by as much as 200 MPa with the bi-modal microstructure having the highest fatigue strength and the coarse lamellar having the lowest.

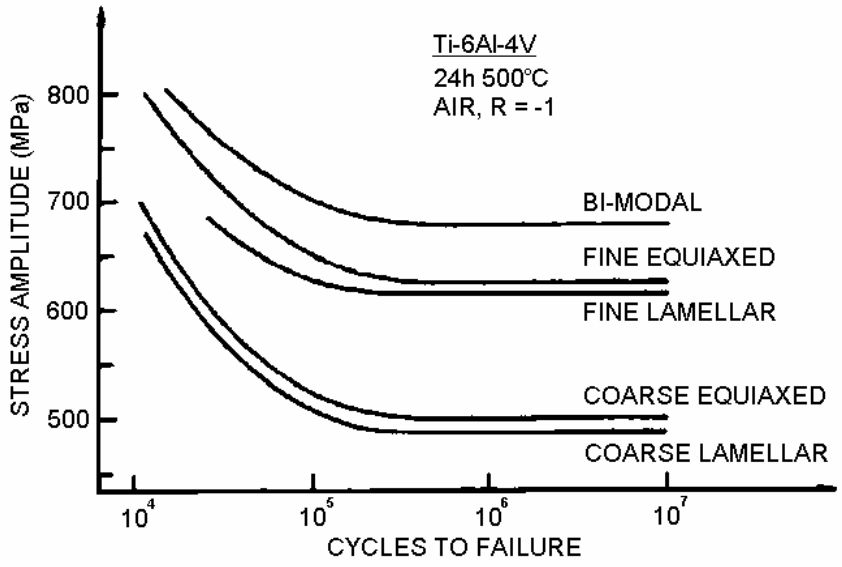


Figure 2.16: Influence of microstructure on high cycle fatigue strength of Ti-6Al-4V (Jaffee and Lutjering, 1987).

## 2.5 Surface Treatments

Surface treatments have been shown to greatly improve the overall life of engineering components that undergo fretting fatigue loading. There are three major principles behind the types of treatments that are commonly used in cases of dry friction where conventional lubricants cannot be maintained. The first principle is to apply a low friction coating on the contacting surface. The next principle is to apply a soft coating that easily shears away, creating a protective layer between the surfaces of the 'structural' material. The final principle is to induce a compressive stress in the surface which resists the initiation and growth of fatigue cracks. In some engineering components, such as jet engine turbine blades, all three of these approaches are used.

Lowering the coefficient of friction between two components reduces the frictional force between the components, thus reducing the amount of damage that is present. This can be achieved by applying hard coatings such as TiN, or diamond coatings. This method is most effective for conditions where gross slip is present (Blanpain et. al, 1995). Liu Dao-Xin et al. (2001) studied the use of another similar coating, $MoS_2$, on Ti-6Al-4V. Under conditions of gross slip, they showed that this film is even better than shot peening in improving fretting fatigue life.

Another method to improve fretting fatigue life is to apply a soft, ductile coating on the components that can easily shear. The resulting debris that is created from shearing forms a layer between the contacting surfaces preventing abrasive wear and initial welding which can occur during fretting. This debris can help decrease the coefficient of friction which also improves the fretting fatigue strength. An example of such a coating used on Ti-6Al-4V is CuNiIn (Fu et al., 1998).

The last major family of surface treatments involves introducing a compressive stress in the surface layer, typically through a cold working process, which helps improve the fatigue life of components including those that undergo fretting fatigue conditions. Three common cold working processes that can be employed in dovetail applications are shot peening, laser shock peening, and low plasticity burnishing. The principle behind these processes is that it creates a compressive layer in the surface of the material that delays fatigue crack initiation and more importantly, retards small crack propagation by closing up small surface cracks and thus reducing the fatigue crack growth driving force. However, a problem with many surface treatments is that if a component is exposed to high operating temperatures, the compressive layer often relaxes, minimizing the effect of the surface treatment. Too much plastic deformation in the surface treatment process has been shown to be a major factor in the relaxation of compressive residual stresses at elevated temperatures. Thus, the most desirable process would create a deep compressive layer with minimal cold work. Figure 2.17 compares the residual stresses and percent of cold work produced by each of the three common cold working methods (Prevey et al., 2002). Each method shown in Figure 2.17 is discussed in more detail in the following sections.

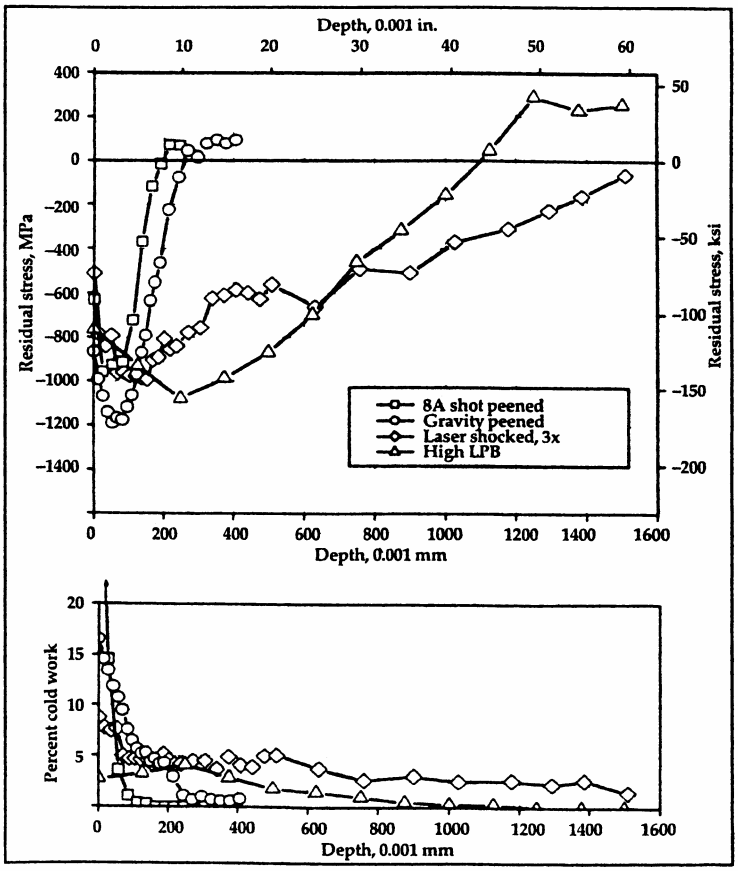


Figure 2.17: A comparison of the residual stresses and percent cold work produced by shot peening, laser shock peening, and low plasticity burnishing in IN718 (Prevey et al., 2002).

### 2.5.1. Shot Peening

Shot peening is a process where a metallic material is bombarded with small steel, glass, or ceramic balls leaving a uniformly dimpled surface. The magnitude and depth of the residual stress is controlled by the shot size and the peening intensity. Shot peening is an inexpensive and popular process, although it does have some disadvantages. The process causes substantial plastic deformation due to repeated bombardments. This can lead to reduced ductility and durability of the surface of the material. Additionally, if the shot peening is too severe, the material will become brittle with higher notch sensitivity (Namjoshi et al., 2002).

### 2.5.2. Laser Shock Peening

The laser shock peening (LSP) process works on the principle that a laser hits a material, generating local heat which creates a shock wave sufficient to cause plastic deformation in the surface layer. The laser is scanned along the surface of a component. Several passes are made with the laser, generally on the order 1 to 5 passes. LSP is capable of forming a layer much deeper than shot peening, yet with much less cold work (Martinez et al., 2003).

### 2.5.3 Low Plasticity Burnishing

In low plasticity burnishing (LPB), a smooth, free-rolling spherical ball under a normal force makes a single pass over the surface of a material leaving a residual compressive stress in the surface. A fluid is used to support the ball and to prevent it from touching the retaining spherical socket. The ball is free to roll on the surface of the material and its only mechanical contact is with this surface. One limitation of the process is that the surface must be in the line of sight of the ball. A schematic of the process is shown in Figure 2.18. This process is capable of producing a very deep layer of high magnitude compressive stress while creating minimal plastic deformation, a quality which makes it very suitable for high temperature applications (Prevey et al., 2002). In addition, the resulting surfaces are smoother than those obtained in shot peening or LSP processes. The surface of a specimen that was treated with LPB can be seen in Figure 2.19. Figure 2.20 shows results of fretting fatigue testing on electropolished (ELP), shot peened, and LPB treated specimens (Shepard et al., 2003). These tests were conducted under constant amplitude 4-point bend loading on a fatigue machine that was modified with a bridge-type fretting device. The fretting bridge used

pins to create cylindrical contact geometry. Both types of surface treated specimens showed substantial improvement in fatigue life. However, the LPB treated specimens clearly showed greater improvement than the shot peened specimens.

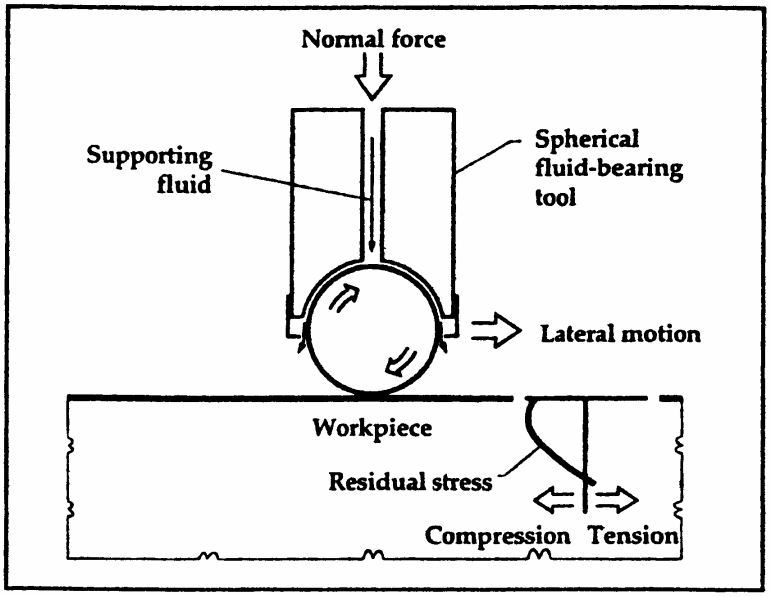


Figure 2.18: Schematic of Low Plasticity Burnishing Process (Prevey et al., 2002).

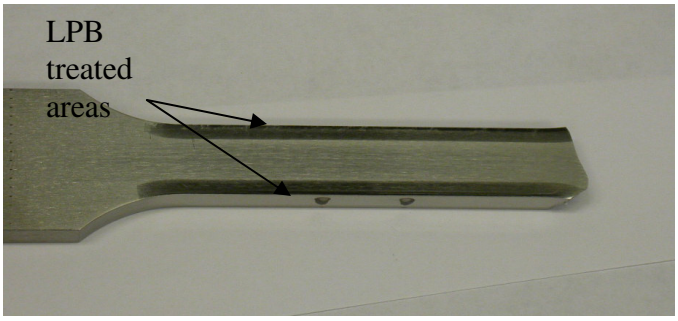


Figure 2.19: Specimen treated with Low Plasticity Burnishing. The darker areas indicate the smoother finish resulting from the LPB treatment.

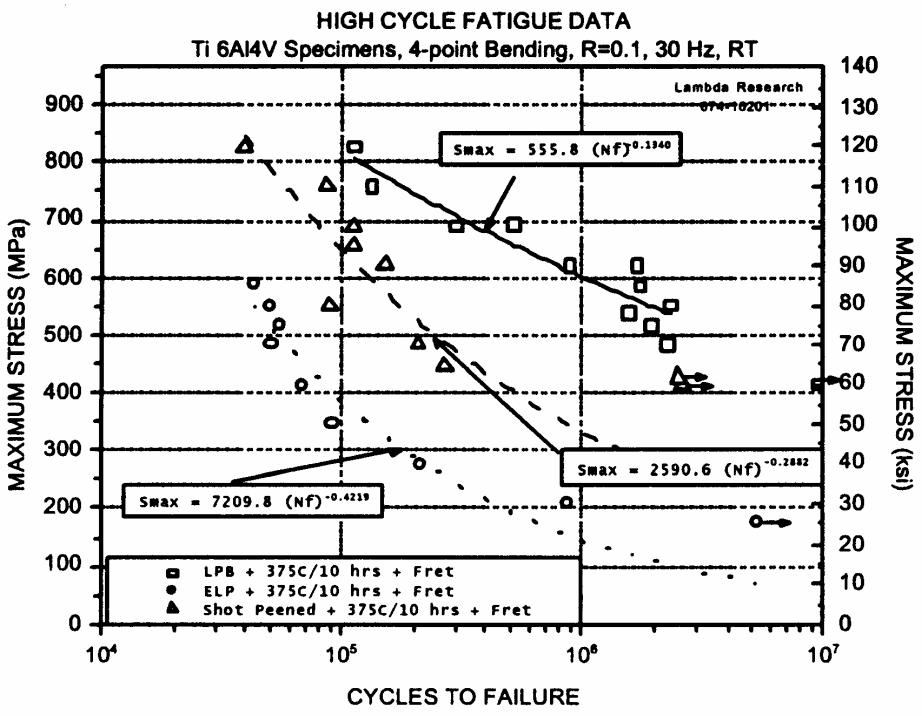


Figure 2.20: Comparison of fretting HCF data for electropolished (ELP), shot peened, and LPB treated specimens (Shepard et al., 2003).

## 2.6 Life Prediction Models

Many life prediction models have been introduced that attempt to predict the nucleation or propagation of fretting fatigue cracks. Some models can also effectively predict the location and orientation of a dominant fretting fatigue crack. Life prediction models are usually based on the four following general approaches. The critical point approach theorizes that fretting fatigue damage initiates at a specific point. A scalar is used to describe this point where crack initiation occurs due to a maximum stress or strain. The critical plane parameters rely on the idea that the critical damage accumulation depends on both the normal and shear strain along a specific plane. Critical plane parameters are averaged over the fretting fatigue process zone. Singularity parameters use a similar approach as the critical plane parameters, but use a much simpler scalar term for the driving force parameter. Finally, there are the crack growth approaches. Here, the models assume that a crack is present and then predict the life based on the growth of the crack.

### 2.6.1 Critical Point Approaches

Critical point approaches theorize that damage due to fretting fatigue initiates at a point of critical stress or strain. It uses a scalar to calculate this critical location. A well known example of this approach was derived by Ruiz et al. (1984). By analyzing the contacting surfaces of a dovetail joint between blades and discs in gas turbines, they concluded that the surface damage due to fretting depends on the work done by the frictional force between the contacting bodies. Thus, they proposed a fretting fatigue parameter which combines the effect of stress and fretting damage given as

$$\kappa_1 = \tau\delta \tag{2.12}$$

where $\tau$ is the shear stress at the maximum load and $\delta$ is the relative slip amplitude between the bodies. The peak value of this parameter correlated well with severely damaged areas along the contact surface. However, this parameter could not reliably predict the location of the initiation of the main fretting crack because crack nucleation in fretting fatigue can also depend on the maximum tangential stress on the interface (Namjoshi et al., 2002). Thus, Ruiz et al. proposed a modified parameter which could capture the location of crack nucleation

$$\kappa_2 = (\sigma_T)_{\max} (\tau\delta)_{\max} \tag{2.13}$$

where $\sigma_T$ is the maximum tangential stress and $\tau\delta$ is the maximum frictional work. The magnitude of this parameter is determined at each point along the interface. This model offers the advantages of being a simple scalar parameter that captures two of the main drivers for crack formation in fretting. These two main drivers are the maximum tangential stress along the interface and the energy dissipated. Still, this parameter has some weaknesses. The frictional work term, $\tau\delta$, is found rather arbitrarily. Also, although it can be used to capture the location of crack nucleation, it is unable to determine its orientation.

The Smith-Watson-Topper (SWT) parameter corrects for the effects of contact and the effects of the mean stress or strain ratio so that the behavior of Ti-6Al-4V under fretting fatigue can be compared with material undergoing plain fatigue. This parameter is given as

$$\sigma_{\max}\varepsilon_a = \frac{(\sigma_f')^2}{E}(2N_i)^{2b'} + \sigma_f'\varepsilon_f'(2N_i)^{b'+c'} \tag{2.14}$$

where $\sigma_{\max}$ is the maximum stress, $\varepsilon_a$ is the total strain amplitude, $\sigma_f^{'}$ is fatigue strength coefficient, $E$ is the elastic modulus, $N_i$ is number of reversals to crack initiation, $b'$ is the fatigue strength exponent, $\varepsilon_f^{'}$ is the fatigue ductility coefficient, and $c'$ is the fatigue ductility exponent. The SWT parameter also predicts the location of crack initiation to be at the trailing edge of contact which is the experimentally observed location (Lykins et al., 2000).

### 2.6.2 Critical Plane Parameters

There are multiple critical plane parameters that can be used to predict crack initiation in fretting fatigue. These approaches hypothesize that the combination of the range in normal or shear strain along with the normal stress acting perpendicular to this plane is responsible for the critical damage. Their common characteristic is that they use a combination of the maximum shear stress amplitude and the amplitude of the normal stress acting on the plane where the maximum shear stress amplitude occurs (Neu et al., 1999). These parameters usually average stresses or strains over a volume, area, or line (i.e., the fretting fatigue process zone) as compared to a localized approach that calculates stresses or strains at a point. These approaches require that a critical location be predetermined so that the process volume can be taken around that point. Three examples of this type of parameter are the Shear Stress Range (MSR), modified Smith-Watson-Topper (SWT) parameter, and Findley (F) parameter (Naboulsi and Mall, 2003).

The MSR parameter hypothesizes that fretting fatigue crack nucleation is related to the maximum shear stress range. The parameter considers all possible planes averaged over a finite volume. To find the MSR parameter, first an analytical or finite element analysis is performed to calculate the maximum shear stress on all planes at all points in

the contact region. Next, the plane where the magnitude of the shear stress range is at a maximum is determined at all points. Then, the critical location and corresponding critical plane are determined where the shear stress range is a maximum. Finally, the shear stress ratio effect on this critical plane is taken into consideration and the MSR parameter can be given by

$$MSR = \tau_{\max}(1 - R_{\tau})^{m} \tag{2.15}$$

where $\tau_{\max}$ is the maximum shear stress on the critical plane, $R_{\tau}$ is the shear stress ratio on the critical plane, and $m$ is a fitting parameter (Naboulsi and Mall, 2003).

A modified SWT parameter that is based on a critical plane approach was proposed by Szolwinski and Farris (1996) that used the same form as Equation 2.14. This parameter hypothesizes that crack initiation occurs on a plane where the maximum product of normal strain amplitude, $\varepsilon_a$, and maximum normal stress, $\sigma_{\max}$, occurs. This means that the normal strain amplitude and the maximum normal stress are no longer necessarily the principal strain amplitude or the maximum principal stress at a given point, but are instead the strain range and maximum stress normal to the critical plane. The value, location, and critical plane orientation of this parameter are given by the overall maximum of this parameter.

The F parameter hypothesizes that fretting fatigue crack nucleation is related to both the shear stress amplitude and the maximum stress normal on the maximum shear plane. The parameter relates the shear stress amplitude, $\Delta\tau$, and the maximum stress normal on the maximum shear plane, $\sigma_n^{\max}$, as shown in Equation 2.16.

$$F = \Delta\tau + k\sigma_n^{\max} \tag{2.16}$$

The value for the multiplying factor $k$ is determined by fitting fatigue life data empirically. This parameter is also calculated at all points along the planes where the maximum values occur, yielding the location and the critical plane (Naboulsi and Mall, 2003).

### 2.6.3 Singularity Parameters (Asymptotic Approaches)

A singularity exists in the stress field at the edge of contact due to the shear traction. The stress field associated with the singularity can be written in the form (see Figure 2.21)

$$\tau = \frac{H}{r^{\lambda}} \tag{2.17}$$

where $H$ is the intensity of the singularity, $\lambda$ is the order of the singularity, $r$ is the distance from the singular point, and $\tau$ is the relevant stress component, which in this case is the shear stress along the contact interface (i.e., the shear traction). From Equation 2.8,

$$\tau = \frac{1}{\pi\sqrt{2ax - x^2}} \cdot \frac{Q}{l} \tag{2.18}$$

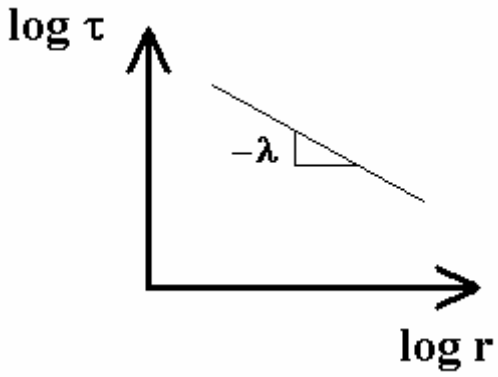


Figure 2.21: Relationship of the singularity parameters very near the singularity.

As $x \to 0$ (singular point), the $x^2$ term becomes insignificant. The equation can then be written as

$$\tau = \frac{1}{\pi\sqrt{2a}} \cdot \frac{Q}{l} \cdot \frac{1}{\sqrt{x}} \tag{2.19}$$

since $x = r$, $\lambda = \frac{1}{2}$ and

$$H = \frac{1}{\pi\sqrt{2a}} \cdot \frac{Q}{l} \tag{2.20}$$

Substituting for the contact half width, *a*, from Hertz theory (Equation 2.1),

$$H = \frac{1}{\pi\sqrt{2}\left(\frac{4R}{\pi E^*} \cdot \frac{P}{l}\right)^{1/4}} \cdot \frac{Q}{l} \tag{2.21}$$

With further simplification, the intensity of the singularity for 2D line contact is

$$H = \frac{Q}{2(\pi l)^{3/4}} \left(\frac{E^*}{RP}\right)^{1/4} \tag{2.22}$$

Ahmad and Santhosh (2004) proposed that the fretting fatigue driving force is associated with the strength of the singular stress field at the contact boundary. The hypothesis is that the propensity for crack formation is related to the singular stress field that would be generated at the contact boundary if microslip was not allowed to occur. It is assumed that the amount of microslip will also be related to the singular stress field. This analysis leads to the identification of a fretting fatigue life 'controlling parameter'. Since the stress field near the contact boundary is similar to that of the tip of a crack under Mode II loading, the general form of the parameter can be written

$$H = F\tau_\infty\sqrt{\pi\ell} \tag{2.23}$$

where $F$ is the geometry factor, $\tau_\infty$ is the remote shear stress, and $\ell$ is a function of P (the normal or contact force). He considers the special case of a line contact between bodies with surfaces that each have a constant radius ($R_{1c}$ and $R_{2c}$) at the contact boundary $O_1$ as shown in Figure 2.22, using finite element analysis (FEA) to determine the singular field, which can be used to determine the singular stress field for any general loading configuration. A typical mesh used in the analysis is shown in Figure 2.23. Maximum and minimum values of the stress intensity factors, $H_{max}$ and $H_{min}$, are then considered as parameters related to the time or load cycles ($N_i$) at crack nucleation due to fretting fatigue.

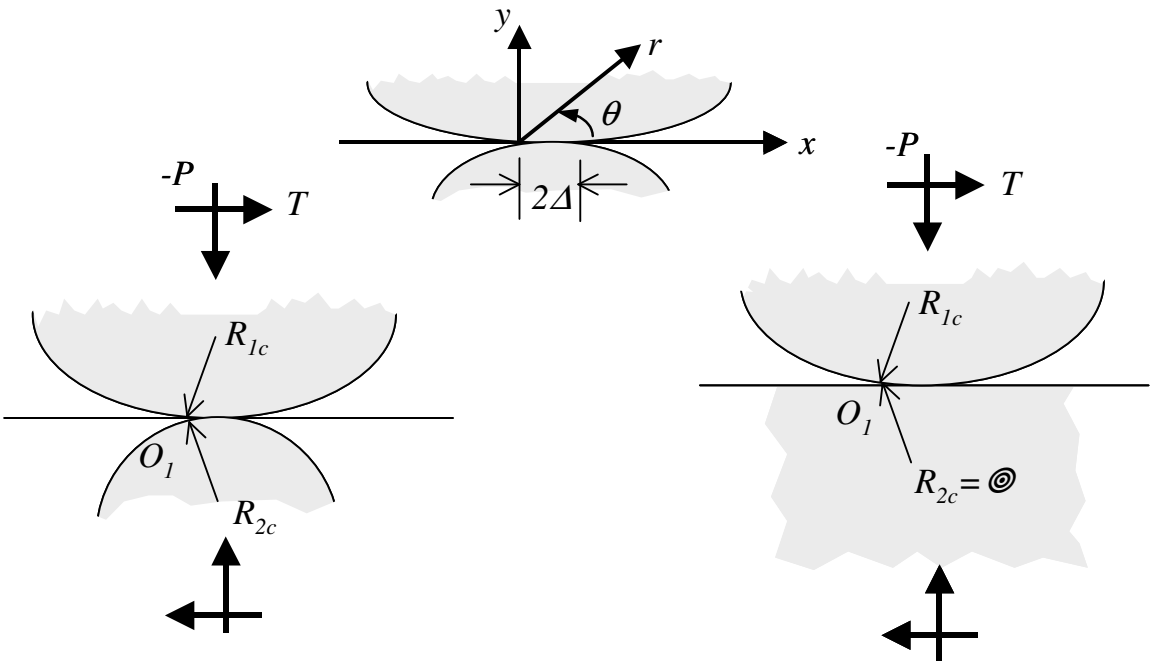


Figure 2.22: Planar forced contact of surfaces with constant radii and sliding forces (Ahmad and Santhosh, 2004).

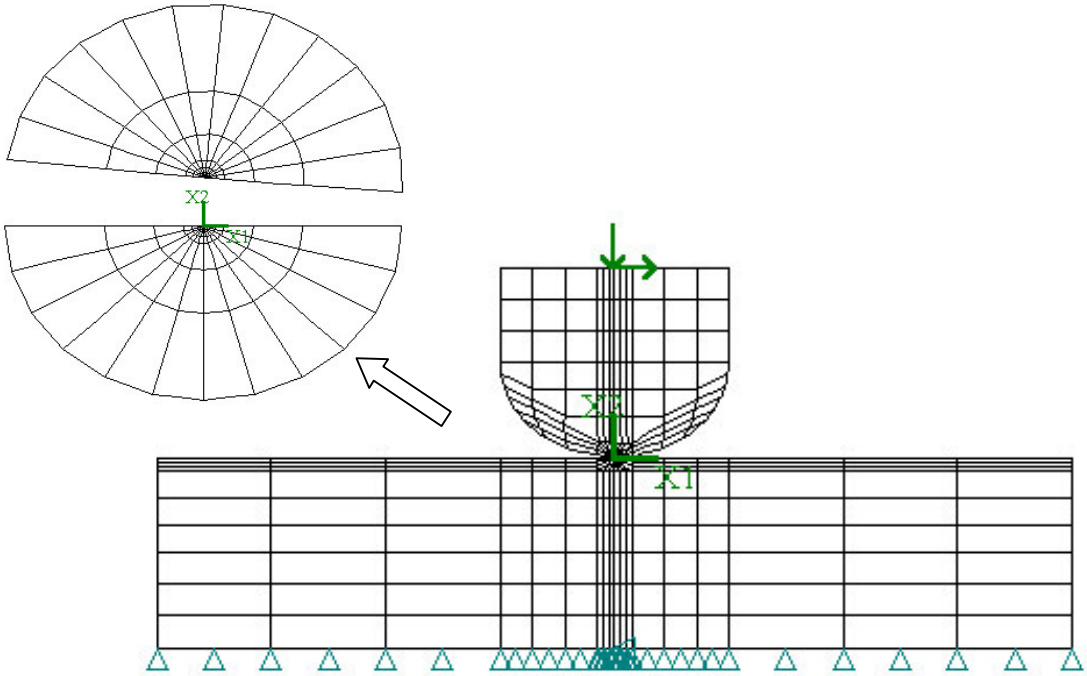


Figure 2.23: Finite element mesh in a typical analysis (Ahmad and Santhosh, 2004).

Hattori (2003) has also analyzed the singular stress field at the contact boundary using numerical techniques to calculate the stress distribution. In his work, he determined both the order of the singularity, $\lambda$, and the intensity of the stress singularity, H, as a regression fit of the stress distributions near the contact edge to Equation 2.17. He proposed a criterion for crack initiation $H_C$ that depends on both H and $\lambda$, which relates to the plain fatigue limit and the threshold stress intensity factor range ($\Delta K_{th}$) of a material. This makes it possible to estimate the stress amplitude that causes fretting crack initiation.

An H-based model has benefits over other proposed models. First, it is a scalar parameter that characterizes the magnitude of the stress field near the edge of contact. Additionally, neither a coefficient of friction nor the boundary between stick and slip is

required in order to calculate H. These two parameters are often unknown *a priori* and are difficult to estimate, leaving much uncertainty in the results if needed to perform analysis. H is also independent of geometry and is relatively simple to determine, thus making it more suited for use as a design metric for joints and other fitted connections.

The H-based model does have some disadvantages. The model essentially assumes contact is in stick and does not capture microslip. It essentially assumes that the magnitude of H will relate to the amount of microslip, which eliminates the more difficult step of determining microslip. This may be reasonable if microslip is small, but not if the microslip occurs over a good portion of the contact. The model would not be applicable to gross slip fretting conditions, although those conditions would likely lead to a wear situation anyway. Also, the amount of plastic deformation present at the edge of contact must be small compared to the size of the singular stress field.

### 2.6.4 Crack Growth Approaches

Models based on fracture mechanics can be used to predict the crack propagation behavior in fretting fatigue. These approaches can be useful to predict crack 'initiation' since fretting can cause damage in the form of small cracks to develop early causing the cycles to crack 'initiation' to be dominated by microcrack growth. Using this method, the fretting forces are taken directly into account through their affect on the stress field and the stress intensity factors in the fretting region (Faanes and Fernando, 1994).

The crack tip stress intensity factor (SIF) for fretting fatigue is directly influenced by three forces: the cyclic axial force in one of the bodies, normal load at the interface, and the frictional force at the interface. In the analysis, it is assumed that the crack is located at the trailing edge of contact since that is where fretting cracks normally

nucleate. Typically, the SIFs due to the axial force, $K_{ax,\max}$, and the fretting loads, $K_{Q,\max}$ and $K_{P,\max}$, are evaluated individually and then are combined using the principle of superposition to form the total SIF,

$$K_{total} = K_{ax,\max} + K_{Q,\max} + K_{P,\max} \tag{2.24}$$

The total SIF can be applied to crack growth models such as the basic Paris' law,

$$\frac{da}{dN} = C(\Delta K)^m \tag{2.25}$$

where $\frac{da}{dN}$ is the crack growth rate, $\Delta K$ is the stress intensity range, and $C$ and $m$ are material constants. In most cases, the effect of small cracks also needs to be taken into account (Nicholas et al., 2003). A fracture mechanics approach has been shown to predict both finite life when crack 'initiation' is controlled primarily by crack propagation as well as the fretting fatigue limit using threshold SIFs. However, a disadvantage of this method is the need to assume an initial crack length and orientation, which can be a very arbitrary process (Faanes and Fernando, 1994).

Golden and Grandt (2004) have successfully used a crack growth model that examines both the time for fatigue crack initiation and fatigue crack propagation. Their model is useful when long propagation lives exist and can be used to predict conditions under which cracks arrest. The predicted lives showed good correlation with results from fretting fatigue experiments performed on Ti-6Al-4V.

Giannakopoulos et al. (2000) developed a 'crack analogue' model that recognized the similarities between contact mechanics and fracture mechanics. They demonstrated their hypotheses by examining the singular stress field associated with the classical punch problem. They showed that the asymptotic elastic stress and strain fields around the

region at the edge of contact are identical to those given by linear elastic fracture mechanics for analogous geometries. Thus, their model makes it possible to unify fretting fatigue and classical fatigue crack growth models based on classical fracture mechanics.

# CHAPTER III

# MATERIAL

## 3.1 Material

One of the most commonly used titanium alloys is Ti-6Al-4V. This alloy is known for its excellent combination of high specific strength, toughness, and corrosion resistance. However, the material has been shown to be very susceptible to fretting fatigue. Despite this shortcoming, the material's high strength-to-weight ratio at moderate temperatures makes it desirable for critical rotating components in gas-turbine engines such as fan and low pressure compressor disks and blades (Antoniou and Radtke, 1997).

The fretting fatigue tests were performed on material that was part of a series of plates that were forged for the U.S. Air Force High Cycle Fatigue Program. All fretting specimens and fretting pads where machined from two plates of Batch #2 labeled #11 and #14. The dimensions of the plates are 40.6 cm (16 in) by 15.2 cm (6 in) by 2.0 cm (0.8 in). The plates have the following mechanical properties: $\sigma_{YS}$ = 930 MPa (134.9 ksi), $\sigma_{UTS}$ = 978 MPa (141.8 ksi), E = 118 GPa (17.1 Msi), $\nu$ = 0.361 (Eylon, 1998). The typical microstructure, shown in Figure 3.1, consists of equiaxed 60% primary alpha phase and 40% secondary alpha and beta lamellar phase. The forging process caused the alpha grains to be slightly elongated and weak crystallographic texture to be present. The microstructure of the plate exhibited no substantial differences between the middle sections and the far-end zones (Eylon, 1998).

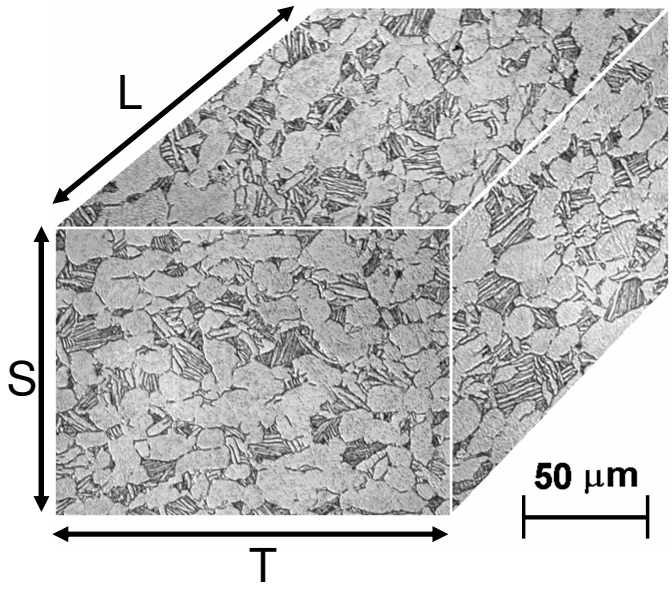


Figure 3.1: Ti-6Al-4V microstructure where L, T, and S are the longitudinal, transverse, and short transverse directions, respectively (Cortez et al., 2000).

### 3.2 Mechanical Properties

The cyclic stress-strain behavior of the HCF Program Ti-6Al-4V material for various strain ratios can be seen in Figure 3.2. A Ramgood-Osgood relationship, $\sigma = K'\varepsilon^{n'}$, can be used to describe the cyclic response of the material where $K'$ = 855 MPa and $n'$ = 0.0149. The cyclic yield strength is 797 MPa indicating that the material cyclically softened from its monotonic yield strength of 930 MPa.

Smooth bar fatigue data, also known as plain fatigue ($K_t$ = 1.0), for several stress ratios are shown in Figure 3.3 (Dunyak, 1999). The Walker equation (3.1) can be used to collapse all of the data to a single equivalent stress curve. The equivalent stress, defined as the equivalent zero-to-tension (R = 0) stress range, is defined as (Walker, 1970; summarized by Dowling, 1999),

$$S_{eq} = S_{\max}^{1-\gamma} \Delta S^{\gamma} \tag{3.1}$$

where $S_{max}$ is the maximum bulk stress, $\Delta S$ is the bulk stress range, and $\gamma$ is a constant. This equation can also be written in terms of R ($= S_{\max} / S_{\min}$) and $S_{max}$,

$$S_{eq} = S_{\max} (1 - R)^{\gamma} \tag{3.2}$$

This definition is consistent with that used in the U.S. Department of Defense publication MIL-HDBK-5G (2003). A regression analysis was performed using the Walker equation, and the constant, $\gamma$, was found to be 0.272 for the data in Figure 3.3. The Walker equation can be adapted to give an equivalent completely reversed nominal stress amplitude, $S_{ar}$,

$$S_{ar} = S_{\max}^{1-\gamma} S_a^{\gamma} \tag{3.3}$$

where $S_a$ is the stress amplitude. In this form, it is clear that the Walker Equation is a generalized version of the Smith-Watson-Topper (SWT) parameter (Equation 3.4) and is equivalent to the SWT parameter when $\gamma$ is equal to 0.5 (Dowling, 1999).

$$S_{ar(SWT)} = \sqrt{S_{\max} S_a} \tag{3.4}$$

Table 3.1 lists estimates for plain (smooth specimen) fatigue limits at $10^7$ cycles based on stress amplitude for this data. The table demonstrates the strong effect that stress ratio has on fatigue life for plain fatigue.

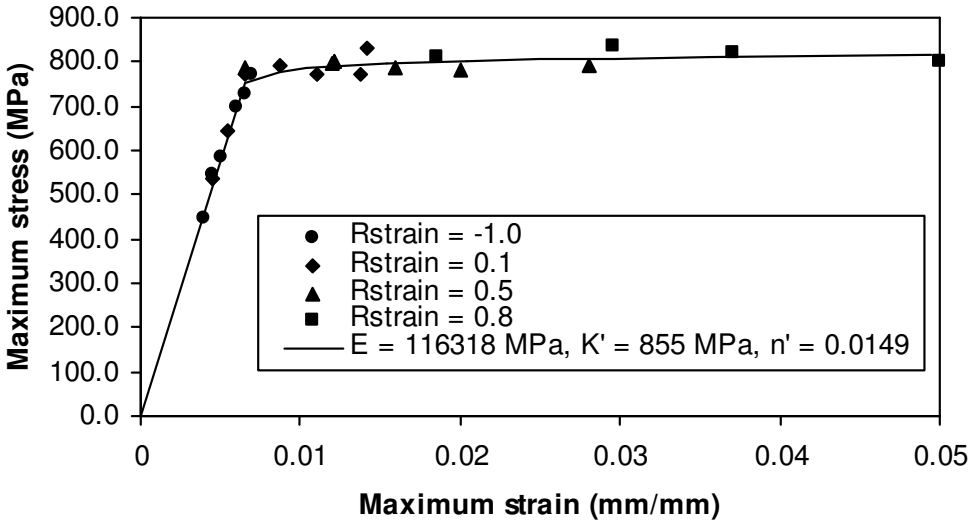


Figure 3.2: Cyclic stress-strain curve for Ti-6Al-4V (Dunyak, 1999).

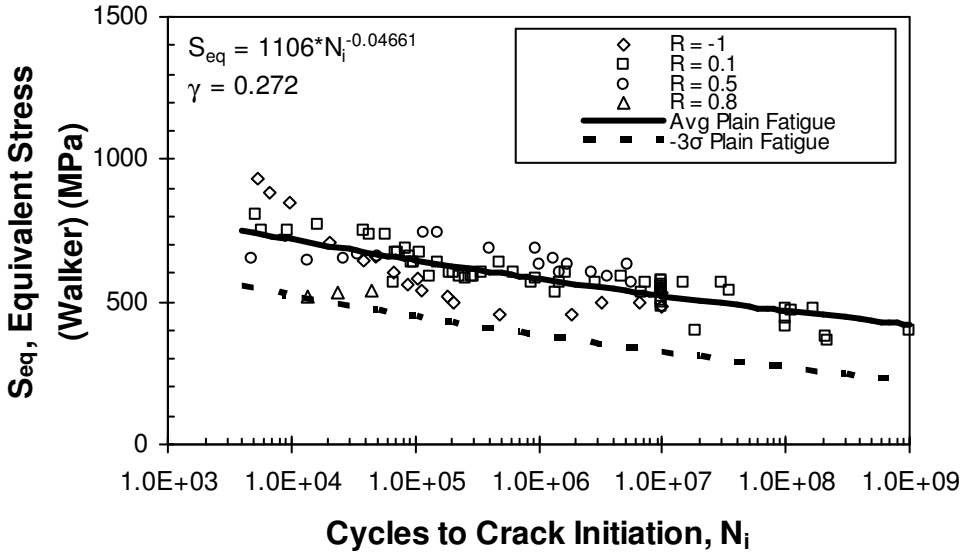


Figure 3.3: Smooth bar fatigue data for Ti-6Al-4V (Dunyak, 1999).

Table 3.1: Estimates for plain (smooth specimen) fatigue limits at $10^7$ cycles based on stress amplitudes for different stress ratios.

| Stress Ratio, R | Stress Amplitude (MPa) |
|---|---|
| -1 | 400 |
| 0.1 | 220 |
| 0.5 | 165 |
| 0.8 | < 80 |

# CHAPTER IV

# EXPERIMENTAL PROCEDURE

## 4.1 Fretting Fatigue Testing Apparatus Design

A 'bridge-type' configuration was used for the fretting fatigue testing that was based on a design by Pape (1997). A simple schematic of this type of configuration is shown in Figure 4.1. This type of configuration is effective in creating the desired condition of a small amplitude relative slip between a contact pad and specimen while the specimen is undergoing fatigue loading. It is also relatively easy to use and has the ability to monitor the useful fretting fatigue parameters. This design was chosen because it is very capable of creating and controlling the necessary fretting fatigue conditions and is less expensive than other types of fretting fatigue test devices. The actual testing apparatus used in this study was designed by Wallace (2001).

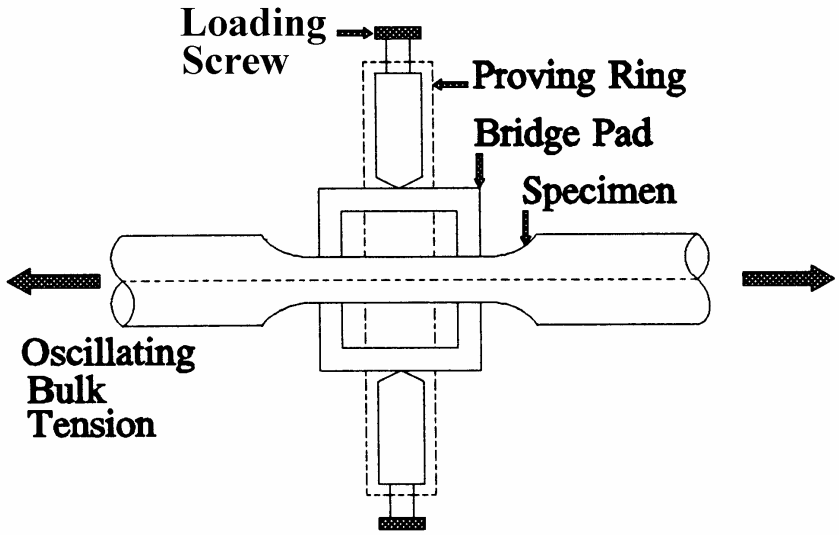


Figure 4.1: Schematic of bridge apparatus attached to fatigue specimen (Hills and Nowell, 1994).

The regions of contact created by the fretting pads and the specimen are shown in Figure 4.2. Both flat and cylindrical fretting pad contact geometries were used in the test program although only one type of geometry was used in each test. The flat fretting pads contained two flat contact feet each with a 4 mm contact width and the cylindrical pads contained two cylindrical contact feet each with a 50 mm radius. The amplitude of relative slip is proportional to the bulk stress amplitude applied to the fatigue specimen and the distance between the fretting pad feet.

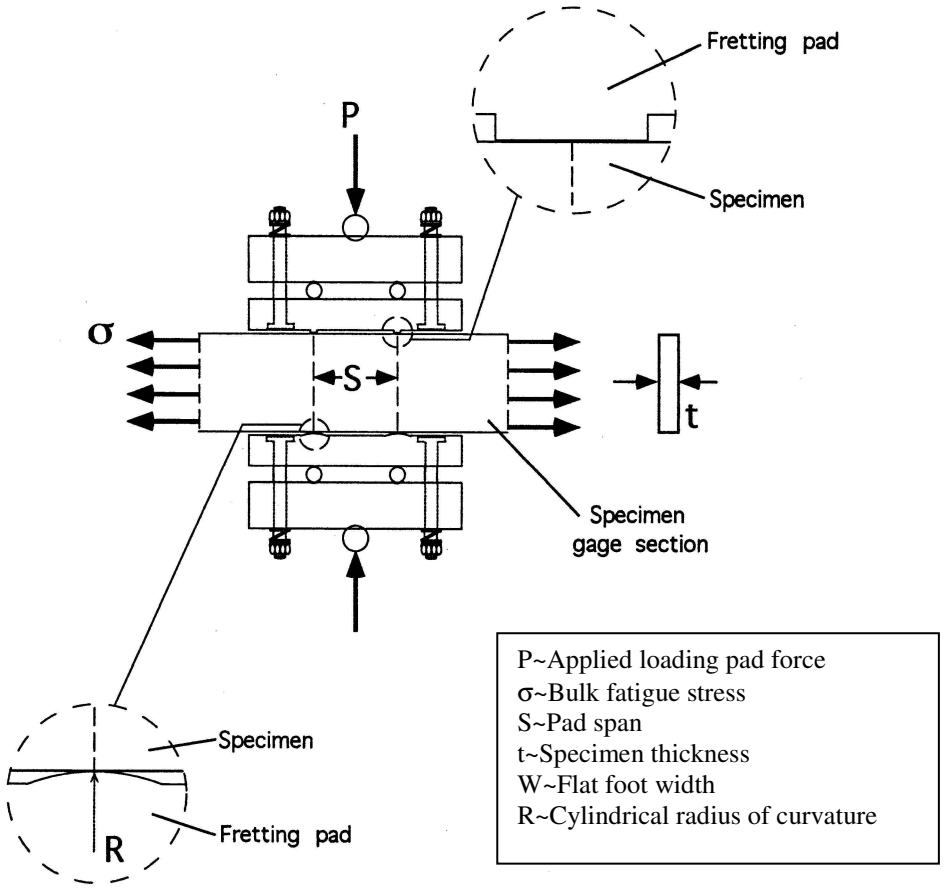


Figure 4.2: Fretting pad and specimen assembly showing flat and cylindrical contact geometry (Pape, 1997).

The size and geometry of the proving ring determines the maximum normal load that can be applied. A closed form solution for determining the maximum tensile stress due to the bending of a ring from opposing, diametric point loads is given by Pilkey (1997) as

$$\sigma_{\max} = K_t \left[ \frac{P}{2h(R_2 - R_1)} \left[ 1 + \frac{3(R_2 + R_1)\left(1 - \frac{2}{\pi}\right)}{R_2 - R_1} \right] \right] \tag{4.1}$$

where P is the opposing normal point load, h is the width of the ring, $R_1$ is the inner radius of the ring, $R_2$ is the outer radius of the ring, and $K_t$ is the stress concentration factor of the ring which is related to the ratio of the inner and outer radii. A high strength 4140 steel heat treated to a hardness of 48 HRC was chosen for the ring material. Using Equation 4.1 and a tensile yield strength of 1378 MPa, this material would be capable of a maximum normal load of 16.78 kN. The maximum normal load during testing was 4.89 kN (1100 lbs) which safely falls below the critical load of the ring (Wallace, 2001).

Two important parameters in characterizing fretting fatigue are the nominal and relative slip values. Under the assumption of idealized frictionless contact and an idealized rigid fretting bridge, the nominal relative slip amplitude can be given by

$$\delta_n = \frac{\sigma_a}{E} S \tag{4.2}$$

where $\sigma_a$ is the bulk stress amplitude, S is the fretting pad span (see Figure 4.2), and E is the elastic modulus. The true relative slip amplitude, which accounts for elastic deformation in the fretting bridge, can be approximated by

$$\delta_t = \left( \frac{\sigma_a}{E} - \varepsilon_a^{ext} \right) S \tag{4.3}$$

where $\frac{\sigma_a}{E}$ is the bulk specimen axial strain amplitude and $\varepsilon_a^{ext}$ is the fretting pad extensional strain amplitude. $\varepsilon_a^{ext}$ is found by dividing the strain amplitude measured on the fretting pad by the bending correction factor, $C_B$, which was determined during frictional force calibration tests, as described in the next paragraph.

The frictional force between the fretting pad feet and the specimen is given by

$$F_t = \varepsilon^{pad} \frac{EBD}{C_B} \tag{4.4}$$

where $\varepsilon^{pad}$ is the strain at the underside of the pad, E is the elastic modulus of the fretting pad material, B and D are the fretting pad thickness and height, respectively, and $C_B$ is a bending correction factor. This correction factor was found to be 4.49 for flat fretting pads and 5.06 for cylindrical fretting pads. The factors were found experimentally in a process that used a split specimen which allowed the entire axial load to be transferred through the two pads. The calibration process used to calculate these factors is described in detail in section 4.3.

## 4.2 Fretting Fatigue Specimen and Fretting Pad Preparation

The dimensions of the fretting fatigue specimens and the flat and cylindrical contact fretting pads were chosen so that the fretting fatigue characteristics such as nominal relative slip, contact pressure, and cyclic loading were representative of actual conditions in aircraft engine components. The dimensions of the fretting fatigue specimens, cylindrical contact fretting pads, and flat contact fretting pads can be seen in Figures 4.3, 4.4, and 4.5, respectively. The fretting fatigue specimens were designed in a dogbone shape to reduce the likelihood of failure in the grips of the testing machine. The specimens and the fretting pads were prepared by Cincinnati Testing Laboratories, Inc., Cincinnati, Ohio. The specimens were machined from Ti-6Al-4V plates that were forged for the U.S. Air Force HCF program. The flat and cylindrical contact pads were prepared using a low stress grind process with a 600 grit surface finish aligned with the longitudinal axis of the specimen. 48 cylindrical contact fretting pads, 16 flat contact fretting pads, and 18 fretting fatigue specimens were machined from plate #11. An additional 12 fretting specimens were machined from plate #14. The location and orientation where each of the specimens and pads was removed from the plates can be seen in Figure 4.6.

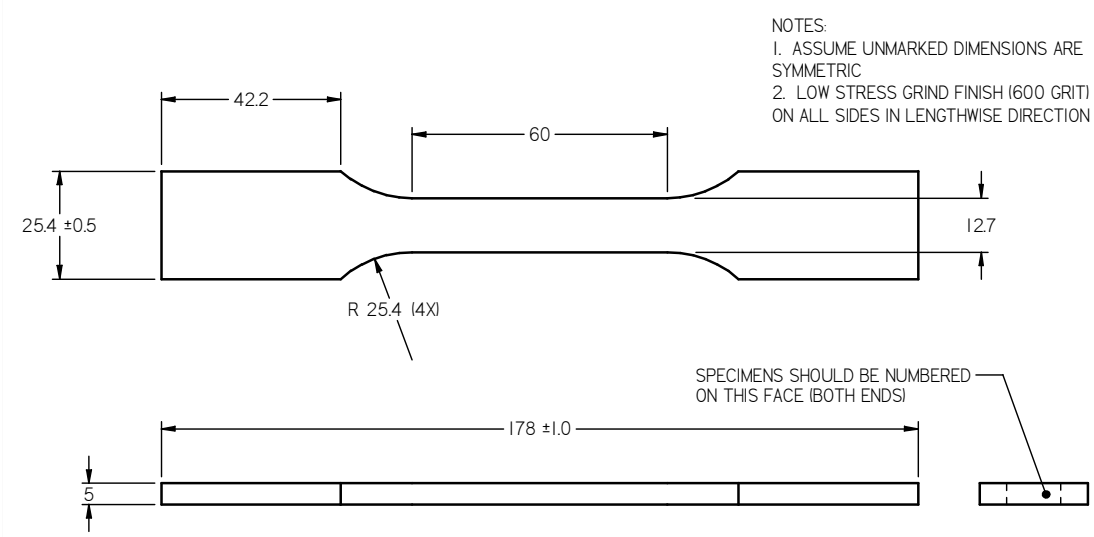


Figure 4.3: Dogbone fretting specimen.

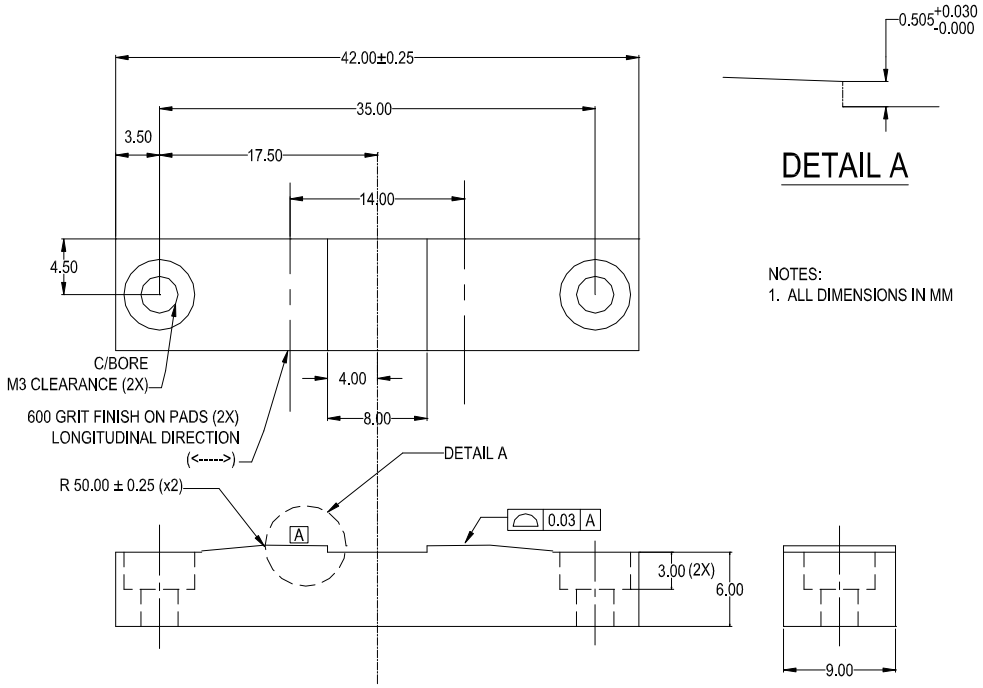


Figure 4.4: Cylindrical fretting pad.

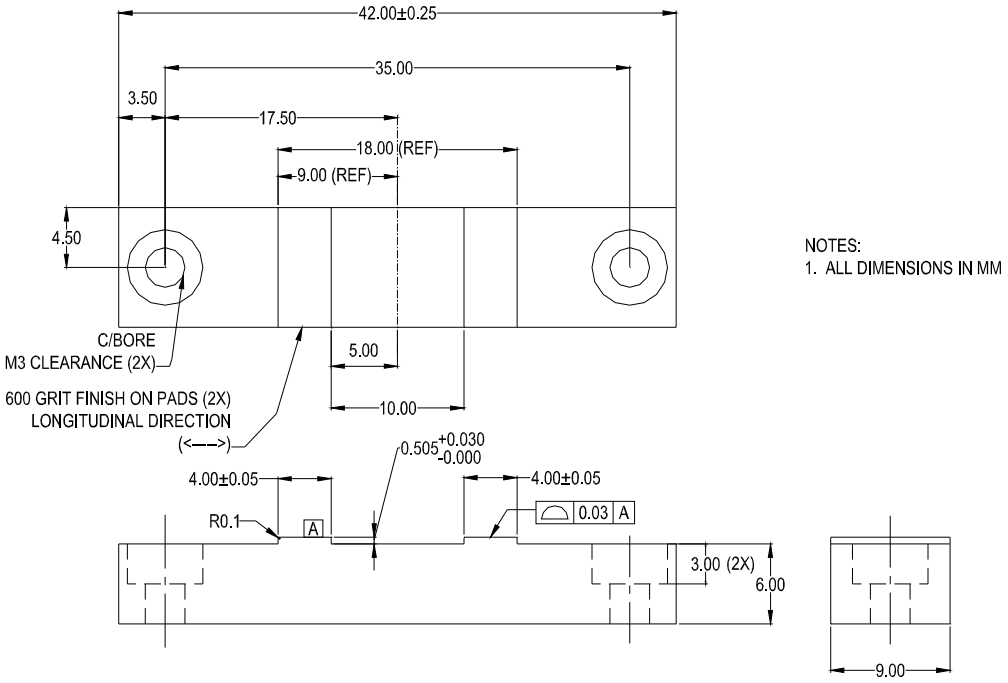


Figure 4.5: Flat fretting pad.

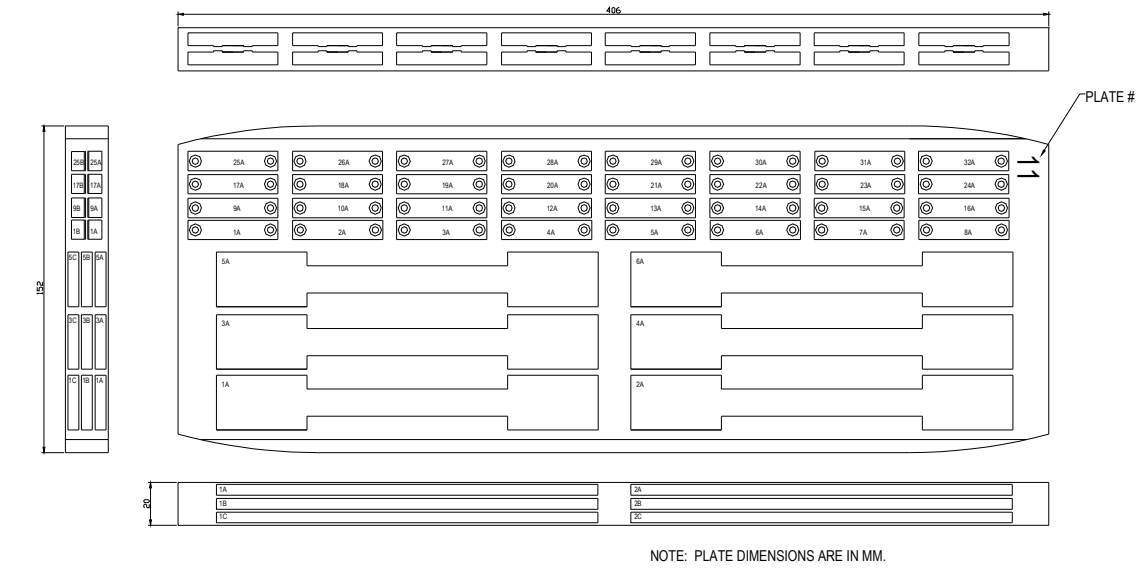


(a)

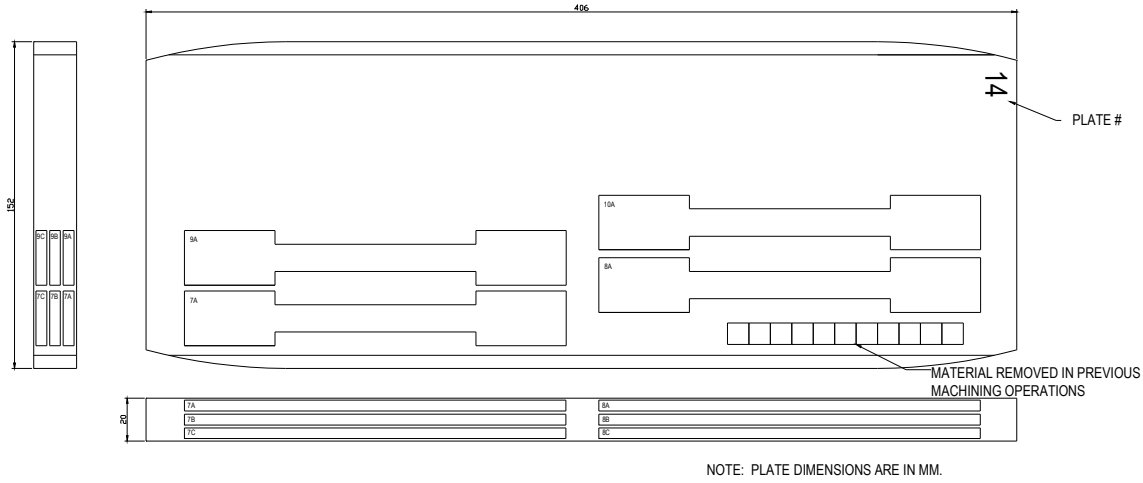


(b)

Figure 4.6: Layout of specimens for (a) plate #11 and (b) plate #14.

Due to limitations in the machining process, the edges of the fretting specimens do not form a perfect corner (i.e., some rounding is present). A typical specimen was sectioned and examined with a Starrett Sigma HB400 optical comparator. The actual dimensions of the corners in the gage section are shown in Figure 4.7. This small amount of rounding meant that even though the fretting pads were wider than the fretting specimens, the fretting scars that resulted from testing did not span the entire width of the fretting specimen since they were not in contact. The results shown in Figure 4.7 are typical of all fretting specimens.

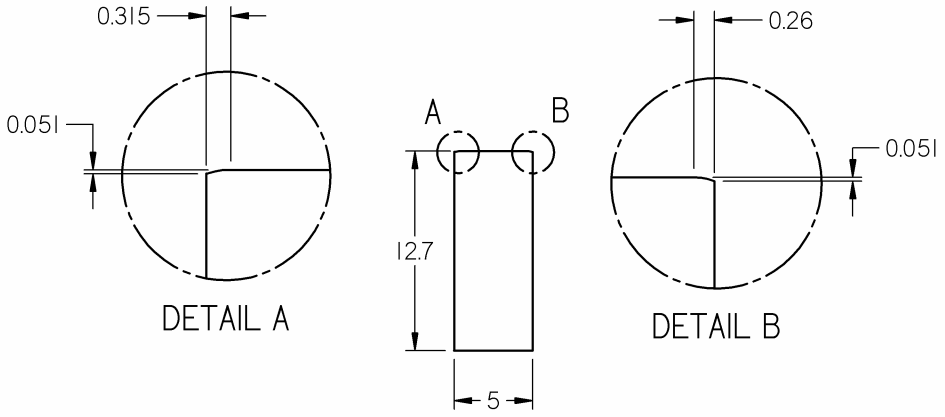


Figure 4.7: Cross section view of the gage section of fretting specimen 7B (dimensions in mm).

### 4.3 Tangential Force Calibration

During testing, a tangential force is created between the fretting pad feet and the specimen surface due to friction. In order to measure this force, strain gages are bonded to the underside of the fretting pad between the contact feet. The strain measured by the gages on the pads is a result of both axial and bending forces in the pad. Therefore, calibration tests are necessary to determine the amount of force that is caused by the bending of the pad.

The calibration procedure is performed using a split specimen shown in Figure 4.8. The fretting bridge is clamped onto either side of the split in the specimen. Thus, all axial force applied to the specimen is transmitted through the fretting pad. Each end of the split specimen contains a hole for attaching to a support at the top end (in our case, a creep test frame) and to a weight platform at the bottom end as shown in Figure 4.9. A metal wire approximately 1/8" in diameter is used to hang the specimen from a creep frame. Weights are added to the platform hung from the bottom end in 10 lb increments and the corresponding voltage obtained from the strain gages is recorded. The process is repeated multiple times for both the cylindrical and the flat fretting pads. The voltages are converted to strain (1 mV = 1 $\mu\varepsilon$) and the resulting data is used to determine the bending correction factor in Equation 4.4. The average value from the trials is used in the analysis of the experimental data.

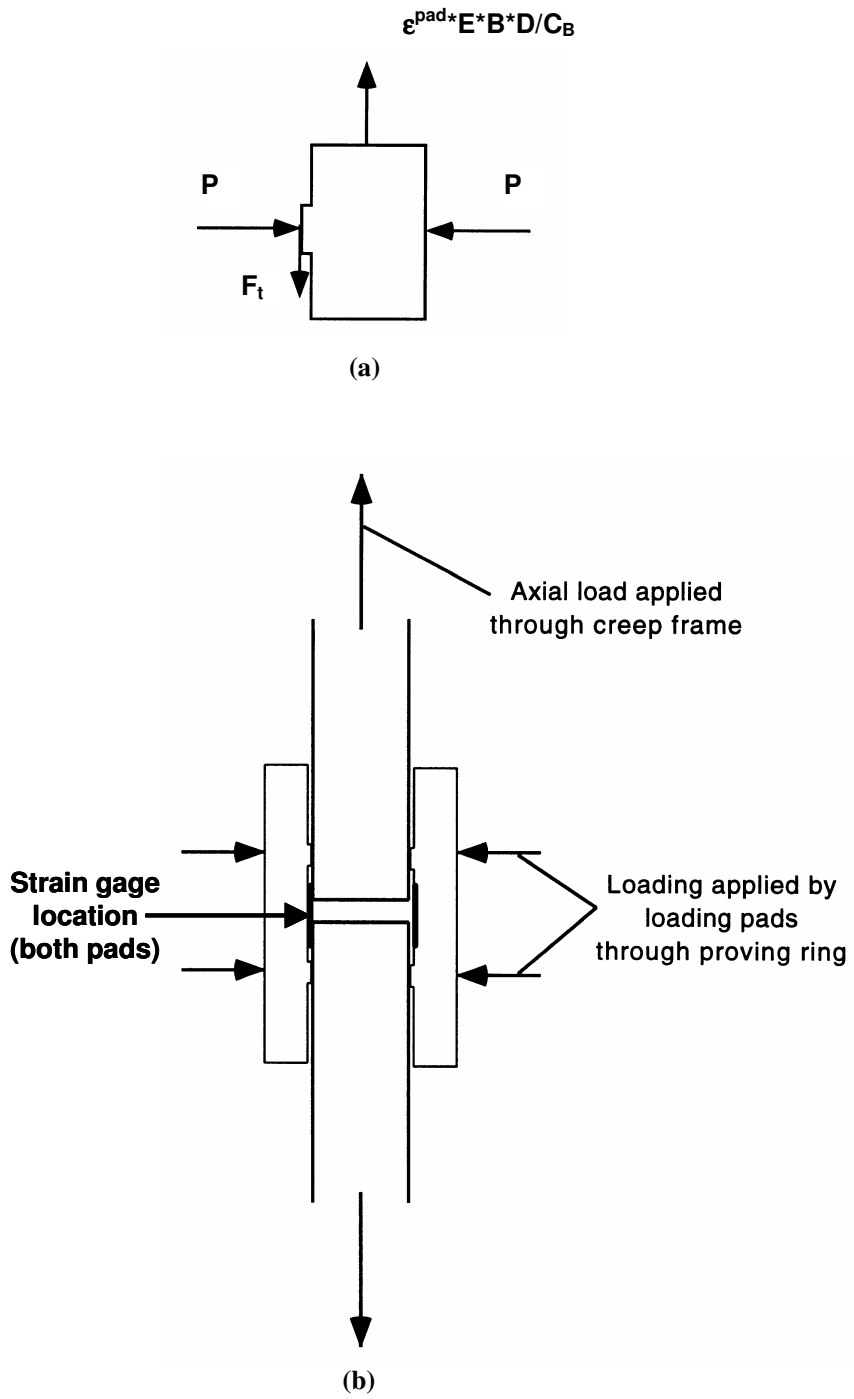


Figure 4.8: Calibration schematics showing (a) a free body diagram of half of a fretting pad and (b) a diagram of the split specimen setup showing the fretting pads and split specimen (Pape, 1997).

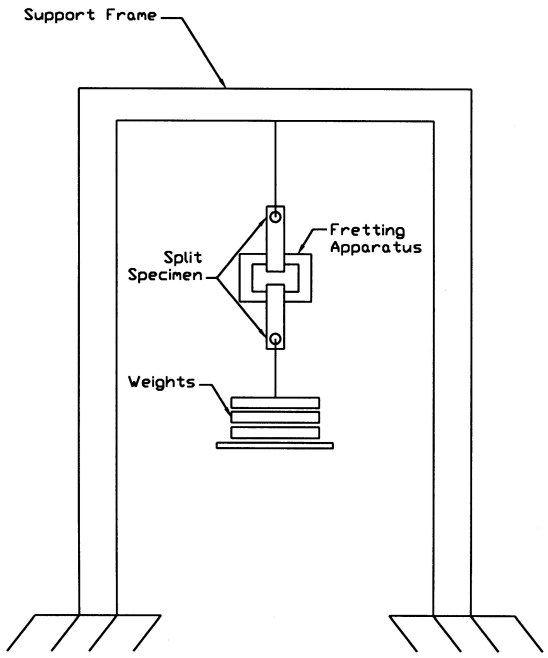


Figure 4.9: Schematic of tangential force calibration.

In our case, the normal force on each pad was held constant at 1112 N (250 lb) throughout the calibration process. Previous calibrations by Wallace (2001) and Pape (1997) demonstrated that a change in the contact force produced no substantial change in the pad strain outputs for the same applied axial loads. The values of $C_B$ are reported in Table 4.1. The complete calibration data is given in Appendix B. The slightly higher value for the cylindrical pad can be explained by the fact that the contact geometry of the cylindrical pad is more inclined to bending than that of the flat pad. With the present configuration, a dynamic calibration was also necessary. This calibration is discussed in section 4.6.

Table 4.1: Fretting pad bending calibration constants.

| | $C_B$ |
|---|---|
| Flat Pads | 4.49 |
| Cylindrical Pads | 5.06 |

### 4.4 Apparatus Assembly

The assembly of the fretting fatigue specimen and testing apparatus can be seen in Figure 4.10. The normal force is applied through a load screw. The force is transferred through a high strength steel ball bearing to a loading pad. Two bolts are used to tighten the loading pad to the fretting pad just enough to hold the sub-assembly together. This setup using the ball bearing and the loading pads allows the load to be evenly distributed along the feet of the fretting pads and prevents the introduction of a bending stress into the fretting pad. A load cell is placed inline with the normal loading to measure the normal force. Seven Belleville springs were used to help maintain a constant normal force in the case of excessive wear on the fretting specimen or the fretting pads. Redesigned spacers were used that facilitated assembly by reducing the number of components.

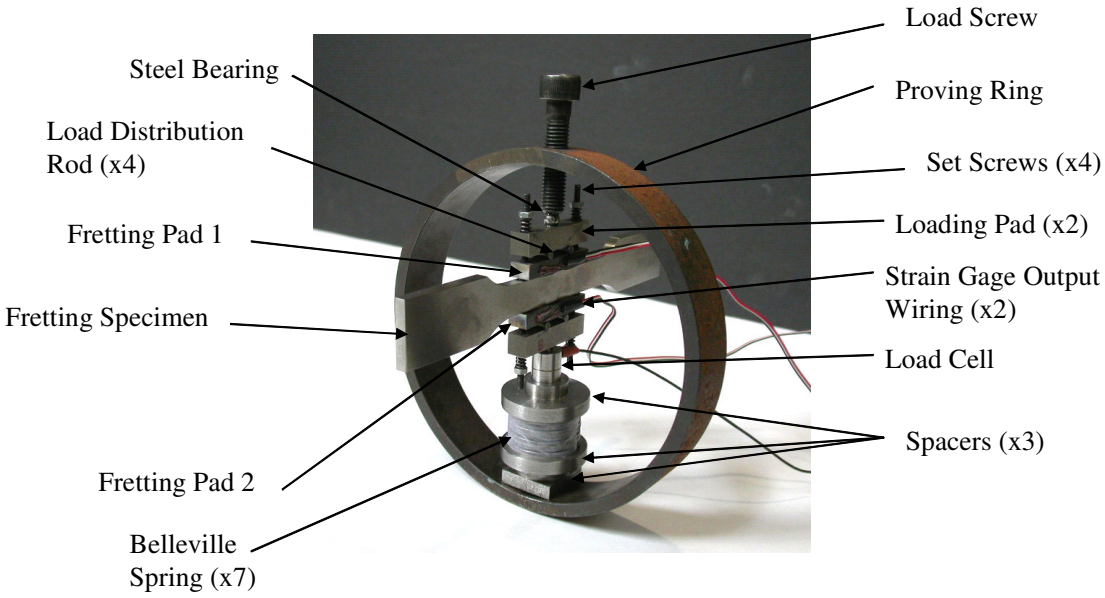


Figure 4.10: Fretting fatigue specimen and testing apparatus.

### 4.5 Test Setup and Execution

Before setting up the test, all contact surfaces of the specimen and the fretting pads were cleaned with ethanol to prevent contamination at the fretting contacts. The specimen was centered in both directions between the fretting pads. After the specimen was properly aligned with the other components inside the proving ring, a normal load was applied using the load screw. This force was monitored by the output display from the load cell that was placed inline with the specimen and the pads. Next, the specimen and fretting assembly were clamped into grips on a servohydraulic testing machine. All fretting fatigue tests were performed on a SATEC 20 kip Servohydraulic Fatigue Test System with MTS 647 Hydraulic Wedge Grips located in the Mechanical Properties Research Laboratory at the Georgia Institute of Technology. Figure 4.11 shows the fretting fatigue assembly mounted in the testing machine. Aluminum spacers bolted to the hydraulic wedge grips were used to both center the specimen along the centerline of the grips and to ensure proper alignment of the specimen in the machine. After the specimen and fretting assembly were installed in the testing machine and grips clamped, the actuator was adjusted to zero axial force (if necessary) and then both of the fretting pad strain outputs and the axial displacement (stroke) were reset to zero. The fatigue test was conducted in axial force control. A constant amplitude cyclic fatigue loading was applied to the specimen at a frequency of 10 Hz. The axial force and the strain gage outputs from the fretting pads were recorded at various cycles throughout the test. The data acquisition system acquired data at a rate of 50 points per cycle. The initial 10 cycles of the test were recorded so that the behavior of the frictional force during the bedding-in phase could be successfully examined. Data was then recorded at cycles

using a logarithmic count (i.e. cycles 10, 20…100, 200…1000, 2000, etc.). Cycles near the end of the test were recorded if the test script detected a large decline in the frictional force signaling the growth of a dominant fatigue crack. The test was stopped once a dominant fatigue crack was detected or when the test reached a runout condition, typically $10^7$ cycles.

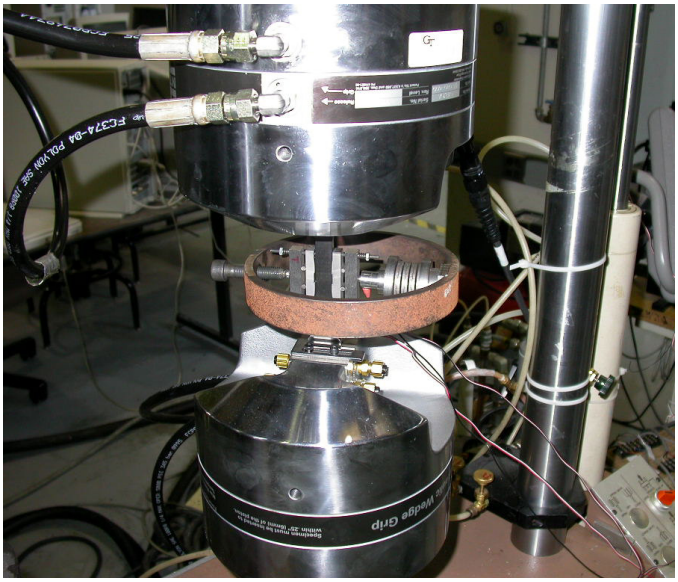

Figure 4.11: Fretting specimen and apparatus clamped in hydraulic grips.

### 4.6 Correction for Frequency Effects

During testing it was noticed that the recorded frictional force values were substantially lower than those found present in previous work performed by Wallace (2001). However, the fatigue life was similar to the lives recorded by Wallace suggesting that the same frictional force was present, but the signal was not being recorded properly. It was discovered that the applied load and the frictional force in the pads were out of phase for all of the tests (see Figure 4.12). Another observation likely related was that there were jumps in the hysteresis loops for the fully reversed tests. An example of this behavior can be seen for specimen 4A in Figure 4.13. A fully reversed plain fatigue test was run using a specimen with strain gages attached to the wide sides of the gage section in the direction of the axial load. The jumps could still be seen in plots of strain vs. the axial load, verifying that problem was not in the fretting apparatus. This jump apparently induces a dynamic load on the fretting apparatus. Currently the exact cause of the problem has not been identified, but it is likely due to the control system of the hydraulic testing machine.

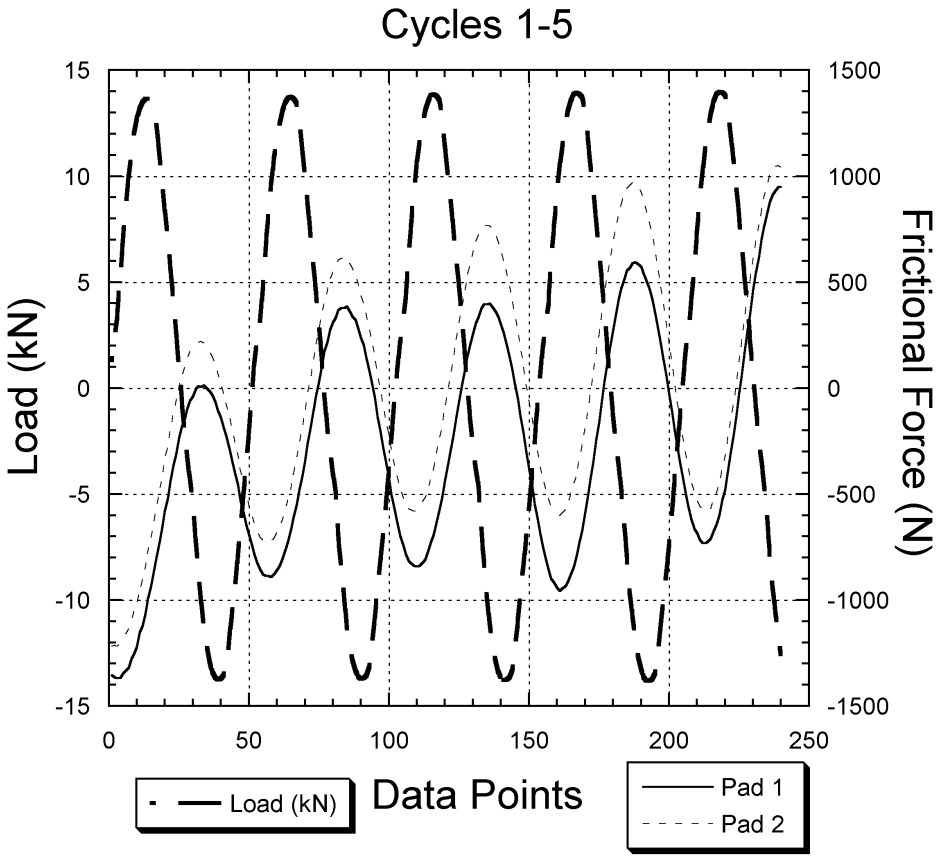


Figure 4.12: Plot showing the out of phase behavior between the applied load and the fretting pads for test specimen 7C.

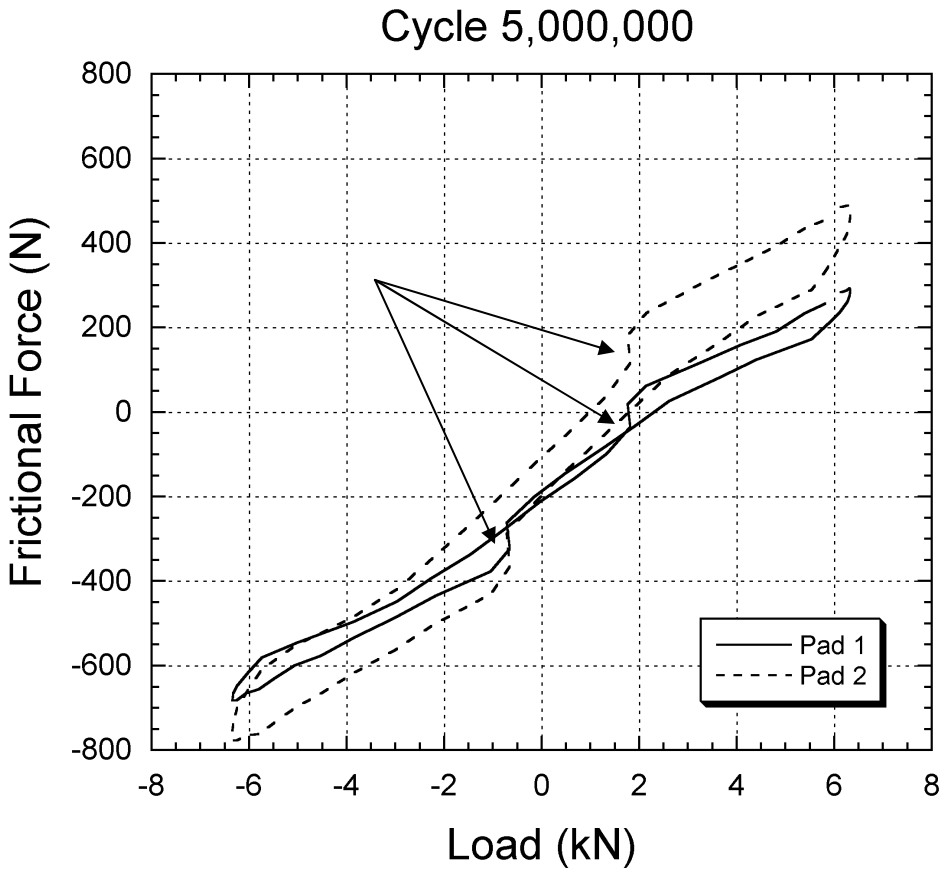


Figure 4.13: A plot of frictional force vs. applied load for specimen 4A ($\sigma_a$ = 100 MPa, R = -1, f = 10 Hz, cylindrical pads). The arrows are pointed at the unexpected jumps in the hysteresis loops.

A correction factor that relates the raw frictional force measured based on a static calibration at 10 Hz to the actual frictional force was determined. To determine this calibration, a fretting fatigue test was conducted at constant stress amplitude, but at different frequencies. Tests were run at frequencies of 10 Hz, 5 Hz, 1 Hz, 0.2 Hz, and 0.05 Hz. The pad strain readings were recorded. The tests were stopped after 1000 cycles because the frictional force ranges had stabilized by that point. This set of calibration experiments was performed at stress amplitudes of 100, 150, 200, and 250 MPa. No change in pad strain range was seen between the tests performed at 0.2 Hz and

0.05 Hz suggesting that the statically equivalent (quasi-static) response had been reached (see Figure 4.14). Using this data, factors were created that correlated the frictional force recorded at 10 Hz to the actual frictional force that was present (i.e. the force recorded at 0.2 Hz). The tests were run on both flat and cylindrical pads, but the same calibration factor was seen for both types of pads. However, different correction factors were required for pad 1 and pad 2 (see Figure 4.10). The different factors for pad 1 and pad 2 are not surprising since the placement of the specimen and the fretting pads within the proving ring is not symmetric. The frictional force range values that were obtained using the correction factors for the pad strain ranges were in line with previous values recorded by Wallace (2001). Appendix C contains the complete results from these dynamic calibration experiments. All of the frictional force results presented throughout this document are corrected values.

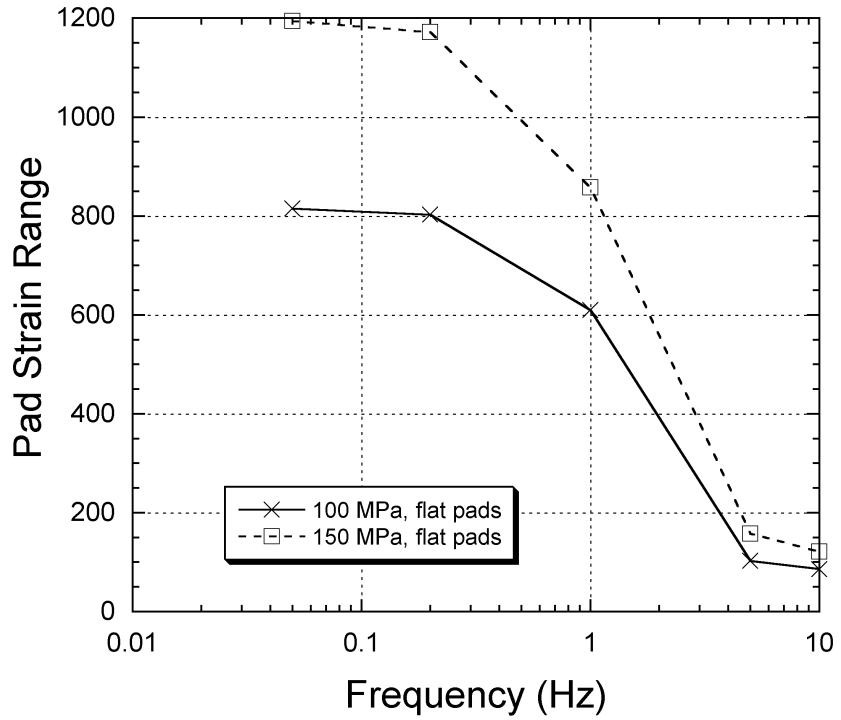


Figure 4.14: A plot showing the change in pad strain range for various frequencies.

### 4.7 Metallographic Procedure

An important part of this study was to use microscopy to characterize the fretting damage. It was imperative to ensure that damage, such as the fretting scars, was consistent with results from prior fretting studies. Subsurface characterization was also necessary to find cracks that may have initiated, but did not propagate into a crack that led to complete fracture. In order to characterize the damage of the specimens, four major steps were necessary to prepare the specimens for examination with either an optical microscope or a scanning electron microscope (SEM): sectioning, mounting, grinding, and polishing.

The specimens were sectioned using a Struers Labotom-3 cut-off machine. This machine uses a high speed abrasive wheel to perform the cutting. A Struers 40-TRE abrasive cut-off wheel was used to cut the specimens. This wheel is designed for tough, ductile materials, making it suitable for use on Ti-6Al-4V.

The specimens were cold mounted using Struers EpoFix resin and EpoFix hardener. The resin and the hardener were mixed in the ratio 15 parts by volume of resin to 2 parts by volume of hardener and were given 8 hours to cure as indicated in the instruction manual. These products were chosen because they offer high hardness for good edge retention and low shrinkage.

The final two steps were performed on a Struers RotoPol-15 automatic polisher. For the course grinding, 500 grit paper was used at a pressure of 35N and a of speed 300 rpm for 5 minutes. Cooling water was used during the grinding process. The next step used a Struers MD-Largo grinding disc. This step was run at a pressure of 35 N and a speed of 150 rpm for 5 minutes. Struers DiaPro Largo diamond suspension was used to

enhance the polishing process for this step. The final step used a Struers MD-Chem polishing cloth. The last step was run at a pressure of 35 N at 150 rpm for 5 minutes. For this step, a mixture of 95% OP-S suspension and 5% $H_2O_2$ (hydrogen peroxide) was used to enhance the polishing process.

### 4.8 Test Matrix

The aim of this study was to determine the effect of stress ratio (mean stress) on fretting fatigue life. The mean stress effect in fretting fatigue is often not clear in models. Under high cycle fatigue, it is well known that higher mean stress leads to lower fatigue life. Under low cycle fatigue, the influence of an initial mean stress is often not significant due to mean stress reduction from cyclic plasticity (e.g., in a zero to tension strain-control loading). It is possible the mean stress effect is not as significant for fretting fatigue due to the large accumulated cyclic plastic strains at the interface.

The test conditions were chosen to provide data for a variety of fretting conditions. The test plan was compared with prior work performed at Georgia Institute of Technology by Wallace (2001) and Swalla (2002) so that conditions could be chosen that would fully characterize the fretting fatigue behavior of Ti-6Al-4V. This broad range of conditions was necessary so that a simple design parameter could be validated. The majority of the testing was done at a fatigue stress ratio equal to -1 since prior testing did not explore this condition. The stress amplitude was varied to achieve a range of fatigue lives between $10^5$ to $10^7$ cycles for both the cylindrical and the flat contact pads. Tests were also conducted on specimens that were treated with Low Plasticity Burnishing to explore the effects of such a surface treatment. A summary of the test plan can be seen in Table 4.2 where R is the fatigue stress ratio, $\sigma_a$ is the stress amplitude applied to the fretting fatigue specimen, P is the normal force applied to each pad foot, and $\delta_n$ is the nominal relative slip amplitude. The experiments at R = 0.1, R = 0.5, and R = 0.8 were aimed at supplementing data generated by Wallace (2001) and Swalla (2002), especially near the fretting fatigue limit.

Table 4.2: Fretting fatigue test matrix for Ti-6Al-4V.

| R | $\sigma_a$ (MPa) | Pad Geometry | Condition | P (N) | Pad Span (mm) | $\delta_n$ (μm) |
|---|---|---|---|---|---|---|
| -1.0 | 100 | Flat w/ radii | virgin | 1340 | 14 | 11.9 |
| -1.0 | 110 | Flat w/ radii | virgin | 1340 | 14 | 13.1 |
| -1.0 | 125 | Flat w/ radii | virgin | 1340 | 14 | 14.8 |
| -1.0 | 150 | Flat w/ radii | virgin | 1340 | 14 | 17.8 |
| -1.0 | 200 | Flat w/ radii | virgin | 1340 | 14 | 23.7 |
| -1.0 | 250 | Flat w/ radii | virgin | 1340 | 14 | 29.7 |
| -1.0 | 100 | Cyl., R=50mm | virgin | 1340 | 14 | 11.9 |
| -1.0 | 125 | Cyl., R=50mm | virgin | 1340 | 14 | 14.8 |
| -1.0 | 150 | Cyl., R=50mm | virgin | 1340 | 14 | 17.8 |
| -1.0 | 175 | Cyl., R=50mm | virgin | 1340 | 14 | 20.8 |
| -1.0 | 200 | Cyl., R=50mm | virgin | 1340 | 14 | 23.7 |
| -1.0 | 200 | Cyl., R=50mm | virgin | 1340 | 14 | 23.7 |
| -1.0 | 225 | Cyl., R=50mm | virgin | 1340 | 14 | 26.7 |
| -1.0 | 250 | Cyl., R=50mm | virgin | 1340 | 14 | 29.7 |
| -1.0 | 275 | Cyl., R=50mm | virgin | 1340 | 14 | 32.6 |
| 0.1 | 80 | Cyl., R=50mm | virgin | 1340 | 14 | 9.5 |
| 0.1 | 100 | Cyl., R=50mm | virgin | 1340 | 14 | 11.9 |
| 0.1 | 120 | Cyl., R=50mm | virgin | 1340 | 14 | 14.2 |
| 0.5 | 75 | Cyl., R=50mm | virgin | 1340 | 14 | 8.9 |
| 0.8 | 85 | Cyl., R=50mm | virgin | 1340 | 14 | 10.1 |
| -1.0 | 275 | Cyl., R=50mm | LPB | 1340 | 14 | 32.6 |
| -1.0 | 300 | Cyl., R=50mm | LPB | 1340 | 14 | 35.6 |
| -1.0 | 350 | Cyl., R=50mm | LPB | 1340 | 14 | 41.5 |
| -1.0 | 400 | Cyl., R=50mm | LPB | 1340 | 14 | 47.5 |
| 0.1 | 250 | Cyl., R=50mm | LPB | 1340 | 14 | 29.7 |
| 0.1 | 300 | Cyl., R=50mm | LPB | 1340 | 14 | 35.6 |

# CHAPTER V

# RESULTS AND DISCUSSION

## 5.1 Fretting Fatigue Lives

The fretting fatigue lives for the new fretting fatigue tests are plotted in Figure 5.1. The majority of the tests developed a dominant fatigue crack that caused the specimen to fracture. Four of the tests were stopped and were considered runout tests, indicated by the arrows on the plot. The fretting fatigue life for the specimen treated with low plasticity burnishing was substantially improved. This test was also considered a runout because it did not fail due to a crack formed at the fretting contact. Figure 5.2 shows the test results plotted along with the data of Wallace (2001) and Swalla (2002) (see Appendix D for a table of these experimental results). These prior tests were performed using the same procedure and test equipment at Georgia Institute of Technology making it possible to directly compare the data. The fretting pad geometry seemed to have little effect on the fatigue life. The stress ratio, R, did have a noticeable impact on fretting fatigue life. The fully reversed tests (R = -1) were the least damaging of the tests for a given stress amplitude. The normal force, P, had a minimal effect within the range of loads considered in this study. The data follows the typical shape of stress-life curves where the cycles to crack initiation increases as the stress amplitude decreases. The R = -1 tests show an especially clear relation for the stress-life curves. There is little deviation between any of the points for this stress ratio. The relationship among the different stress ratios is not as clear in the plot of maximum stress versus the cycles to crack initiation shown in Figure 5.2 (b), suggesting that fretting fatigue is less sensitive to

mean stress than it is to stress amplitude. Using all of the data provided in Figure 5.2, an estimate for the fretting fatigue limit has been established for different stress ratios. These limits are 2-4 times lower than plain fatigue limits found for the experimental work performed by Dunyak (1999) presented in section 3.2. The greater differences existed for the lower stress ratios. The values for the fretting fatigue limits are reported in Table 5.1.

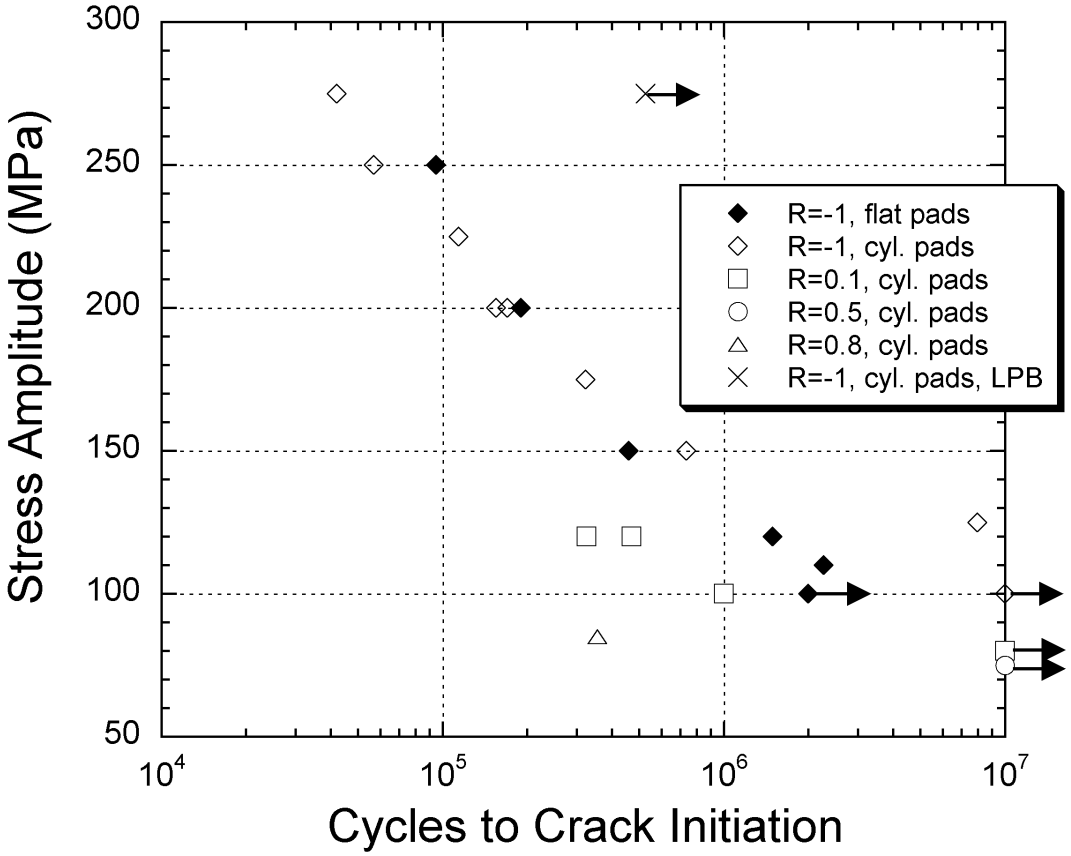


Figure 5.1: Fretting fatigue test results for Ti-6Al-4V (P = 1340 N).

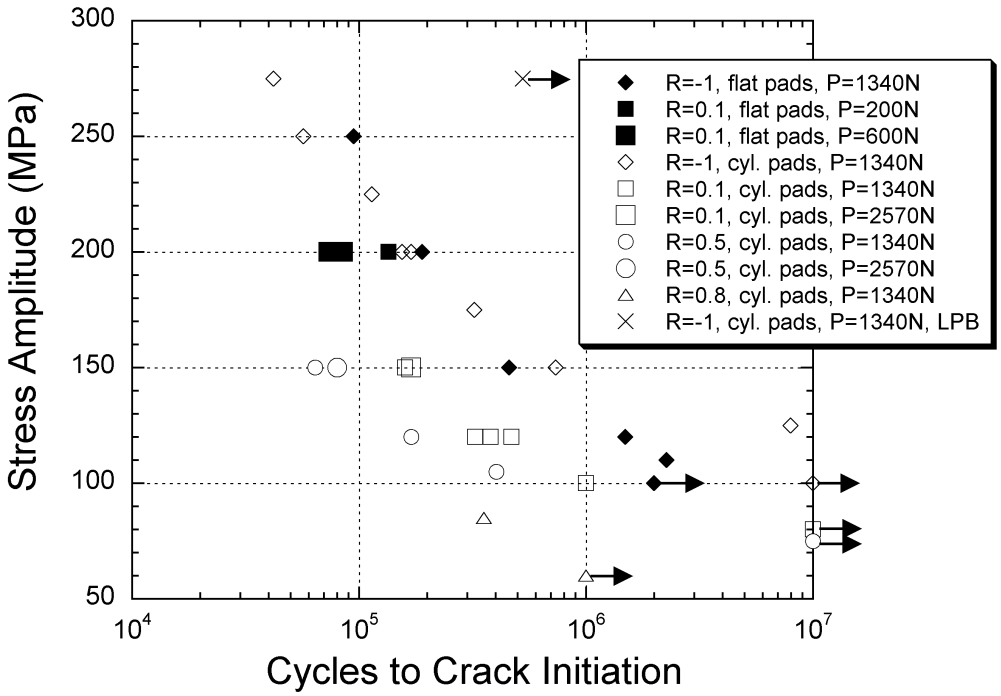


(a)

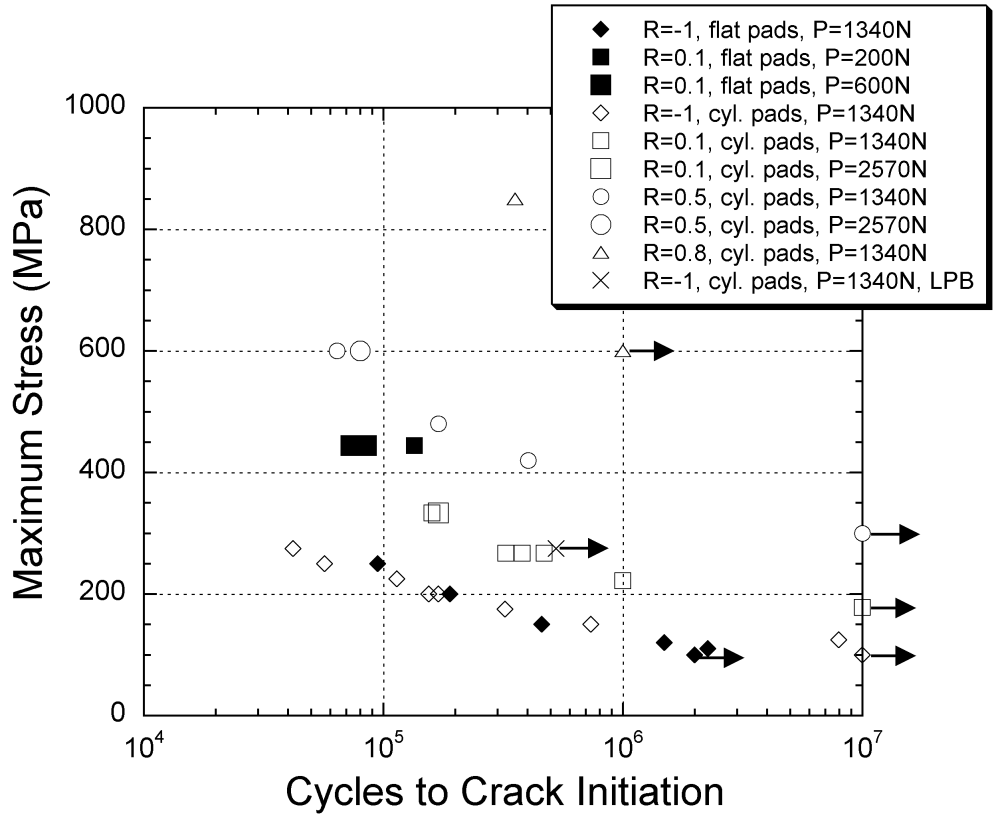


(b)

Figure 5.2: Fretting fatigue results for Ti-6Al-4V for all tests conducted at Georgia Institute of Technology (including data from Wallace (2001) and Swalla (2002)).

Table 5.1: Estimates for fretting fatigue limits at $10^7$ cycles for different stress ratios.

| Stress Ratio, R | Fretting Fatigue Limit (MPa) |
|---|---|
| -1 | 100 |
| 0.1 | 80 |
| 0.5 | 75 |
| 0.8 | 60 |

A detailed summary of the fretting fatigue loading conditions and the results of the tests are shown in Table 5.2. In this table, $\sigma_a$ is the remotely applied axial stress amplitude, R is the remotely applied stress ratio, P is the normal force applied to each foot, $p_{foot}$ is the contact pressure at each pad foot (the peak Hertzian contact pressure is used for the cylindrical pads), $l$ is the average width of the four fretting scars, $\delta_n$ is the nominal relative slip amplitude, $N_i$ is the cycles to crack initiation (defined in section 2.3), and $N_T$ is the total cycles applied to the specimen. The tests were run at a frequency of 10 Hz except where noted. The frictional force values reported in the table are the stabilized frictional force values obtained at half-life. The tests were stopped when fracture occurred due to the growth of a dominant fatigue crack or when the test reached a runout condition, typically $10^7$ cycles.

Table 5.2: Fretting fatigue test results for Ti-6Al-4V.

| Figure | Specimen | R | $\sigma_a$ (MPa) | Pad Geometry | Condition | P (N) | Pad Span (mm) | $\delta_n$ (μm) | $p_{foot}$ (MPa) | $\ell$ (mm) | Frictional Force (N) | | | $N_i$ (Cycles) | $N_T$ (Cycles) | Comments |
|---|---|---|---|---|---|---|---|---|---|---|---|---|---|---|---|---|
| | | | | | | | | | | | Max | Min | Range | | | |
| A.1 | 5B | -1.0 | 100 | Flat w/ radii | virgin | 1340 | 14 | 11.9 | 79.1 | 4.24 | 1283.8 | -6.5 | 1290.3 | 2,000,000 | 2,000,000 | Runout |
| A.2 | 7B | -1.0 | 110 | Flat w/ radii | virgin | 1340 | 14 | 13.1 | 82.4 | 4.07 | 1059.5 | -217.9 | 1277.4 | 2,268,000 | 2,273,660 | |
| A.3 | 9A | -1.0 | 125 | Flat w/ radii | virgin | 1340 | 14 | 14.8 | 86.0 | 3.90 | 1039.5 | -469.2 | 1508.7 | 1,489,000 | 1,491,969 | |
| A.4 | 5C | -1.0 | 150 | Flat w/ radii | virgin | 1340 | 14 | 17.8 | 83.9 | 3.99 | 2010.9 | 8.1 | 2002.8 | 460,000 | 467,240 | |
| A.5 | 3A | -1.0 | 200 | Flat w/ radii | virgin | 1340 | 14 | 23.7 | 81.8 | 4.10 | 2163.8 | -104.5 | 2268.3 | 190,000 | 192,863 | |
| A.6 | 2C | -1.0 | 250 | Flat w/ radii | virgin | 1340 | 14 | 29.7 | 86.2 | 3.89 | 599.6 | -2476.3 | 3075.9 | 95,000 | 99,291 | |
| A.7 | 4A | -1.0 | 100 | Cyl., R=50mm | virgin | 1340 | 14 | 11.9 | 372.0 | 4.18 | 392.8 | -728.1 | 1120.9 | 10,000,000 | 10,000,000 | Runout |
| A.8 | 3C | -1.0 | 125 | Cyl., R=50mm | virgin | 1340 | 14 | 14.8 | 361.9 | 4.42 | 615.7 | -777.2 | 1392.9 | 7,980,000 | 7,982,065 | |
| A.9 | 4B | -1.0 | 150 | Cyl., R=50mm | virgin | 1340 | 14 | 17.8 | 366.3 | 4.31 | 957.2 | -622.8 | 1580.0 | 735,000 | 738,283 | |
| A.10 | 8C | -1.0 | 175 | Cyl., R=50mm | virgin | 1340 | 14 | 20.8 | 357.7 | 4.52 | 535.1 | -1306.4 | 1841.5 | 323,000 | 326,076 | |
| A.11 | 4C | -1.0 | 200 | Cyl., R=50mm | virgin | 1340 | 14 | 23.7 | 371.4 | 4.19 | 1686.1 | -297.0 | 1983.1 | 155,000 | 157,195 | |
| A.12 | 5A | -1.0 | 200 | Cyl., R=50mm | virgin | 1340 | 14 | 23.7 | 363.9 | 4.37 | 1136.0 | -933.5 | 2069.5 | 175,000 | 178,638 | |
| A.13 | 7C | -1.0 | 225 | Cyl., R=50mm | virgin | 1340 | 14 | 26.7 | 372.4 | 4.17 | 1099.2 | -1016.7 | 2115.9 | 114,000 | 117,591 | |
| A.14 | 2B | -1.0 | 250 | Cyl., R=50mm | virgin | 1340 | 14 | 29.7 | 362.7 | 4.40 | 1327.7 | -1065.7 | 2393.4 | 57,000 | 59,978 | |
| A.15 | 9C | -1.0 | 275 | Cyl., R=50mm | virgin | 1340 | 14 | 32.6 | 368.4 | 4.26 | 1290.6 | -1267.9 | 2558.5 | 42,000 | 43,997 | Test run at 1Hz |
| A.16 | 10C | 0.1 | 80 | Cyl., R=50mm | virgin | 1340 | 14 | 9.5 | 366.6 | 4.30 | -4104.4 | -4942.5 | 838.1 | 10,000,000 | 10,000,000 | Runout |
| A.17 | 8B | 0.1 | 100 | Cyl., R=50mm | virgin | 1340 | 14 | 11.9 | 362.8 | 4.40 | 288.3 | -716.6 | 1004.8 | 999,000 | 1,004,798 | |
| A.18 | 2A | 0.1 | 120 | Cyl., R=50mm | virgin | 1340 | 14 | 14.2 | 363.9 | 4.37 | 2679.9 | 1322.3 | 1357.7 | 325,000 | 330,547 | |
| A.19 | 3B | 0.1 | 120 | Cyl., R=50mm | virgin | 1340 | 14 | 14.2 | 367.1 | 4.29 | 1008.0 | -350.1 | 1358.1 | 470,000 | 472,307 | |
| A.20 | 10A | 0.5 | 75 | Cyl., R=50mm | virgin | 1340 | 14 | 8.9 | 358.3 | 4.51 | -109.8 | -923.1 | 813.3 | 10,000,000 | 10,000,000 | Runout |
| A.21 | 7A | 0.8 | 85 | Cyl., R=50mm | virgin | 1340 | 14 | 10.1 | 372.5 | 4.17 | -1143.9 | -2093.6 | 949.7 | 355,000 | 355,971 | |
| A.22 | 6C | -1.0 | 275 | Cyl., R=50mm | LPB | 1340 | 14 | 32.6 | 418.8 | 3.30 | 849.1 | -1404.7 | 2253.8 | 528,000 | 528,075 | |

## 5.2 Frictional Force Measurements

The progression of the frictional force range throughout the test along with the hysteresis between the frictional force range and the displacement, which is proportional to the applied stress (i.e., Equation 4.2), can be used to characterize the damage to the specimen throughout the test. Since displacement is proportional to the applied stress, the hysteresis of frictional force versus displacement is given by plots of frictional force versus applied axial force. There are three characteristic shapes for these hysteresis loops as shown in Figure 5.3. These shapes result from a stick, partial slip, or gross slip contact condition. In a stick condition (Figure 5.3 (a)), there is little relative displacement between the two bodies and microslip exists only at the edge of contact near the singularity. Most of the displacement is due to elastic deformation of the bodies between the 'remote' displacement measurement. In a partial slip condition (Figure 5.3 (b)), the center area of contact is sticking, but the edges are undergoing significant slip to be observed remotely. The partial slip condition tends to be the most damaging fretting fatigue condition. The gross slip condition (Figure 5.3 (c)), involves large relative displacements between the two bodies. The horizontal portion of the hysteresis loop represents gross sliding. This condition typically leads to fretting wear as opposed to fretting fatigue.

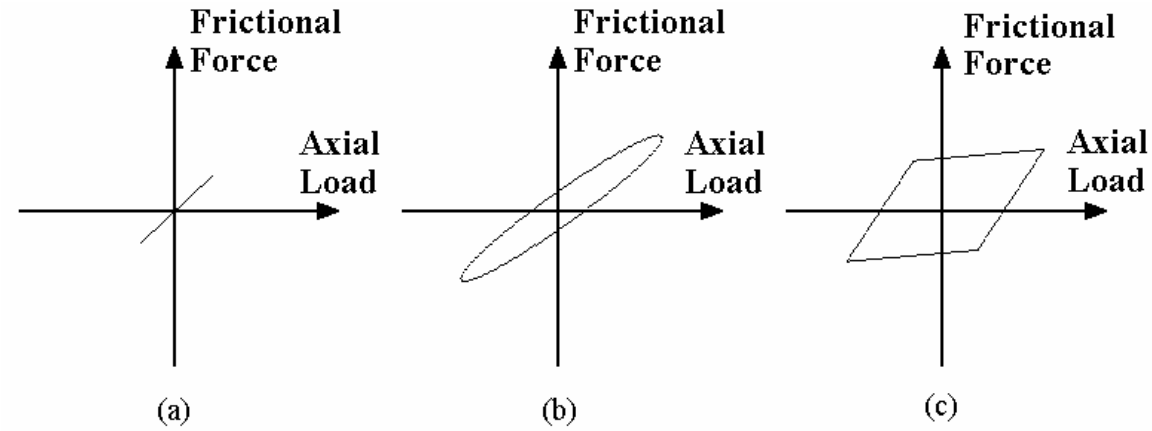


Figure 5.3: Types of frictional force hysteresis loops: (a) stick (b) partial slip and (c) gross slip. The frictional force is plotted on the vertical axis and the axial load, which is proportional to displacement (Equation 4.2), is plotted on the horizontal axis.

Frictional force hysteresis curves for the test run on specimen 7C ($\sigma_a$ = 225 MPa, R = -1, cylindrical pads) are shown in Figure 5.4. Many of the features of this test are representative of other tests in the program. Frictional force hysteresis curves for the tests with the highest and lowest stress amplitudes are also shown in Figure 5.5 and Figure 5.6. Plots for the remaining tests are included in Appendix A. For the majority of the tests, fretting pad 2 had a wider hysteresis loop than fretting pad 1 (See Figure 4.10 for relative location of fretting pads). It is possible that since the arrangement of components within the proving ring is not perfectly symmetrical, slightly different conditions could have been present. However, the difference in hysteresis shape did not seem to affect the location of failure. The location of dominant cracks was evenly distributed among the two pads as well as between the two contact feet on each pad. Another possible explanation is that the signal may have been amplified slightly differently. The differences seemed to subside after the tangential force calibration

procedure was performed even though no intentional changes were made to the amplifier box.

For all of the tests run at 10 Hz, the loops initially started out wide as illustrated in Figure 5.3 (a). The loops tended to get thinner as the test progressed, but usually reached a steady state value within the first 50 cycles. The stress amplitude usually influenced the slip conditions, especially at the beginning of tests. The higher remotely applied stress amplitudes lead to wider hysteresis curves and it took closer to 100 cycles for the curves to reach steady state values.

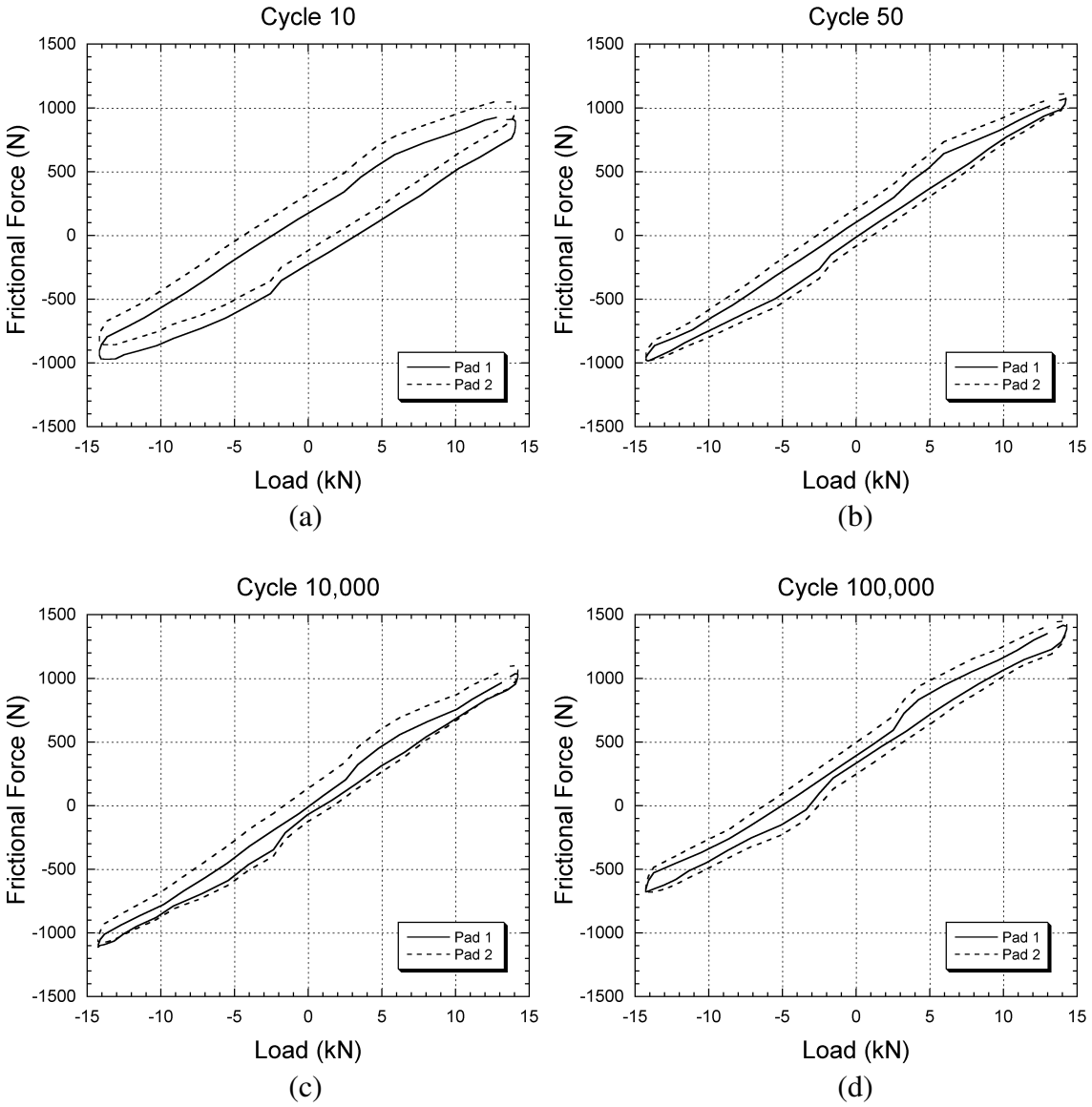


Figure 5.4: Plots of frictional force vs. applied load for specimen 7C ($\sigma_a$ = 225 MPa, R = -1, f = 10 Hz, cylindrical pads) at (a) cycle 10, (b) cycle 50, (c) cycle 10,000, and (d) cycle 100,000.

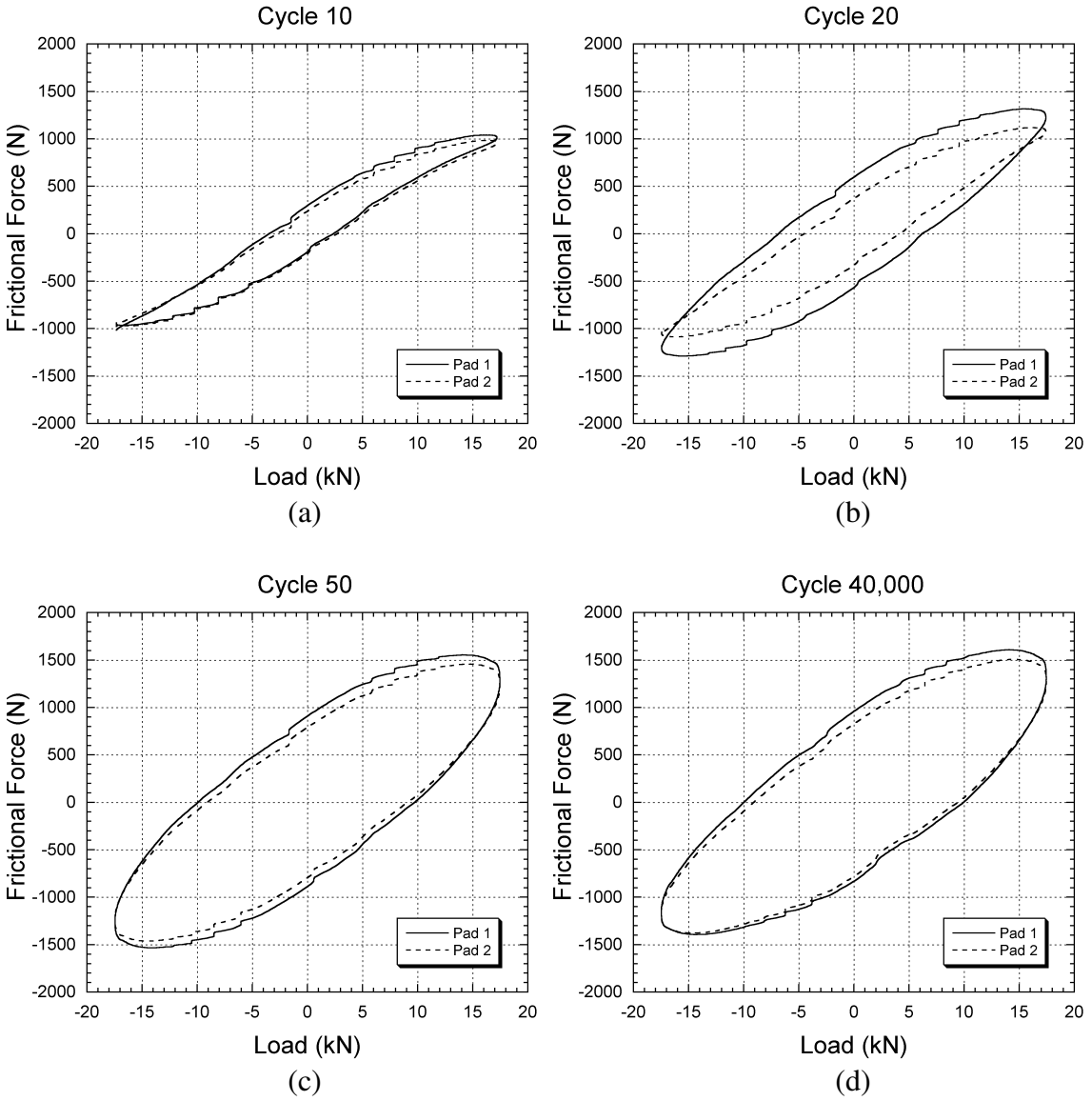


Figure 5.5: Plots of frictional force vs. applied load for specimen 9C ($\sigma_a$ = 275 MPa, R = -1, f = 1 Hz, cylindrical pads) at (a) cycle 10, (b) cycle 20, (c) cycle 50, and (d) cycle 40,000.

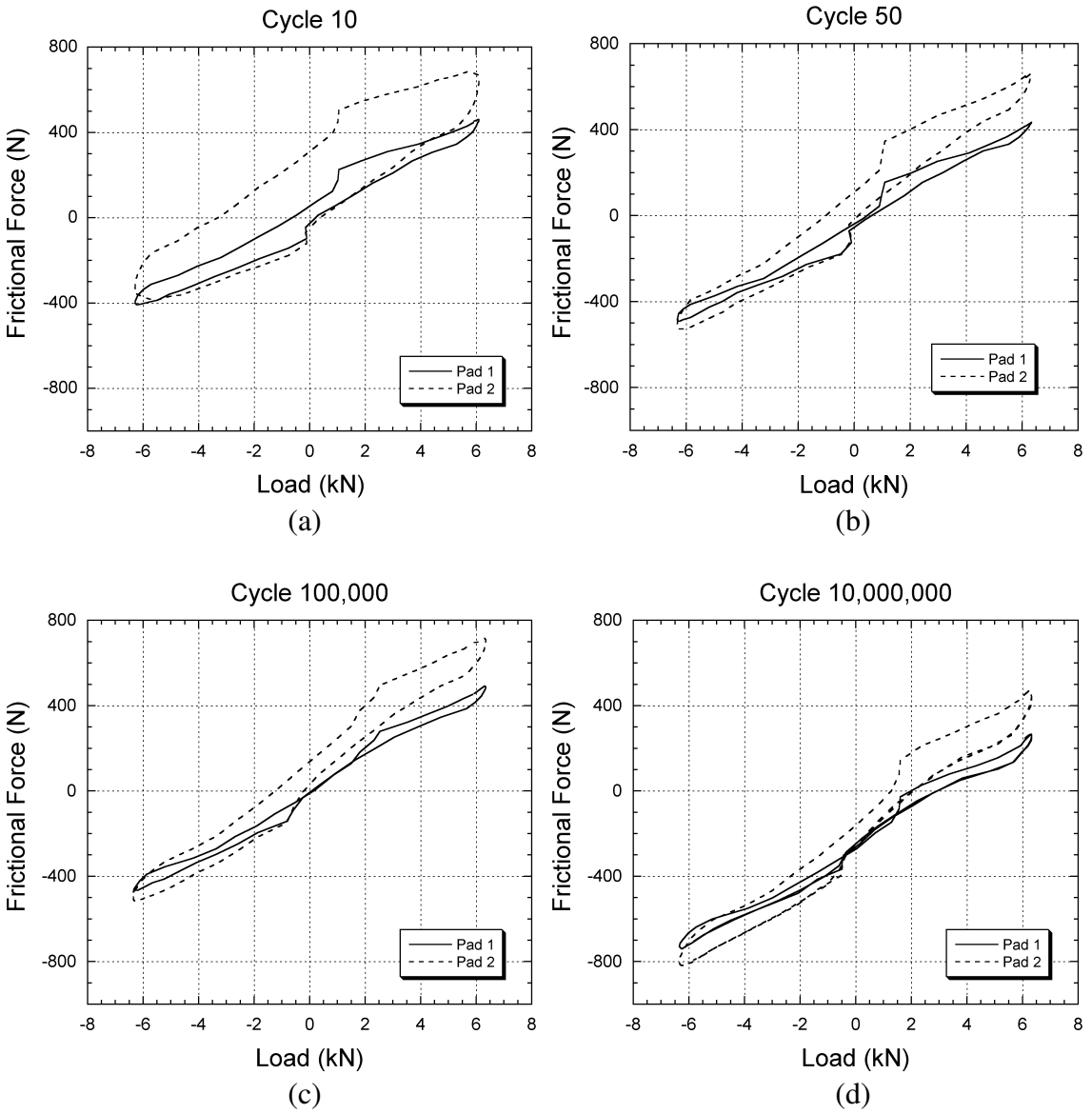


Figure 5.6: Plots of frictional force vs. applied load for specimen 4A ($\sigma_a$ = 100 MPa, R = -1, f = 10 Hz, cylindrical pads) at (a) cycle 10, (b) cycle 50, (c) cycle 100,000, and (d) cycle 10,000,000.

The frictional force range for specimen 7C ($\sigma_a$ = 225 MPa, R = -1, cylindrical pads) is plotted versus cycles in Figure 5.7. This figure shows the progression of the frictional force range throughout the test. An initial 'bedding-in' period was present for all the tests. During this period, the frictional force range increases rapidly as shown in Figure 5.7 (b). After roughly 100 cycles, the frictional force range begins to reach a steady-state value. It remains at this steady state value until it experienced a rapid drop at 114,000 cycles. Figure 5.7 (a) shows that the rapid drop occurred on fretting pad 1, which is the side that the dominant crack initiated. The rapid decrease in the frictional force range was the criteria used to determine the cycles to crack initiation ($N_i$) for the specimen. The decrease was an indication of the growth of a dominating fatigue crack in the specimen which causes a change in the compliance of the specimen. It is important to represent the evolution of frictional force range since the magnitude of the frictional force range appears to be directly related to fretting fatigue crack initiation.

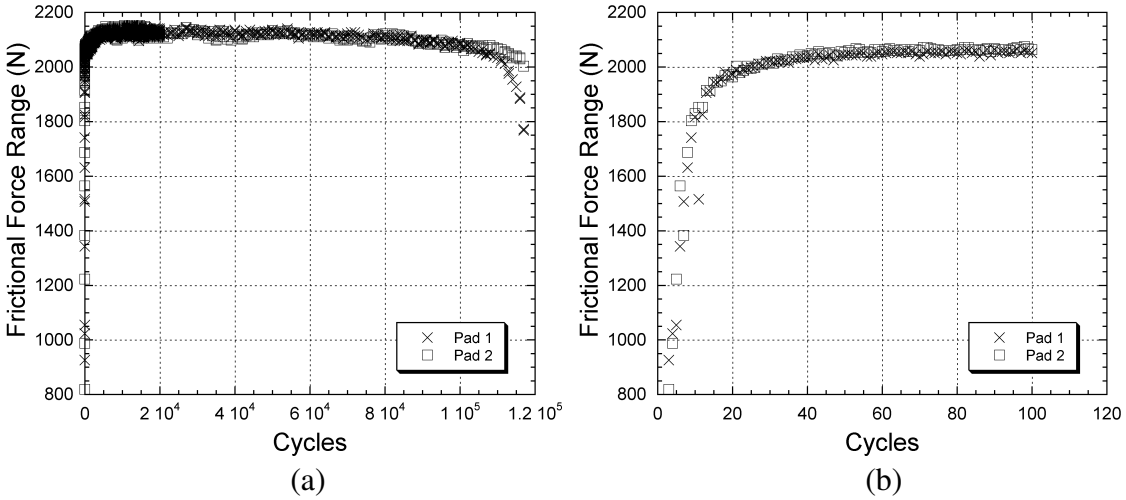


Figure 5.7: Plots of frictional force range vs. cycles for specimen 7C ($\sigma_a$ = 225 MPa, R = -1, cylindrical pads) for (a) the entire test and (b) the initial cycles.

### 5.3 Damage Characterization

The fretting scars of four of the specimens were studied using a scanning electron microscope. The tests with the highest and lowest stress amplitudes at R = -1 for the cylindrical and flat pads were chosen so that the effect of stress amplitude could be seen. Micrographs of the fretting scars are shown in Figure 5.8. The tests with the higher stress amplitudes had darker fretting scars and had more debris present compared to the tests with lower stress amplitudes. Significant damage from slip can be seen in the trailing edges of contact. For all of the specimens in the test program that fractured, a dominant crack initiated at the trailing edge of the fretting scar as shown in Figure 5.9. The variation of the scars across the thickness of the specimen is likely due to unevenness in the contact pressure which was a result of a combination of initial surface roughness and misalignment of the specimen and fretting pads in the proving ring.

The appearance of the fretting scars can be related to the hysteresis loops for the frictional force versus displacement discussed in the previous section. The scars from Figures 5.8 (a) and (c) are characteristic of partial slip. The center regions of these scars were in stick since that region appears to have little damage. Conversely, the trailing edges, which are the regions where slip occurs, show damage. Figures 5.8 (b) and (d) show scars that exhibit much more surface damage. This type of surface damage is characteristic of the energy expended by wider frictional force versus displacement hysteresis loops.

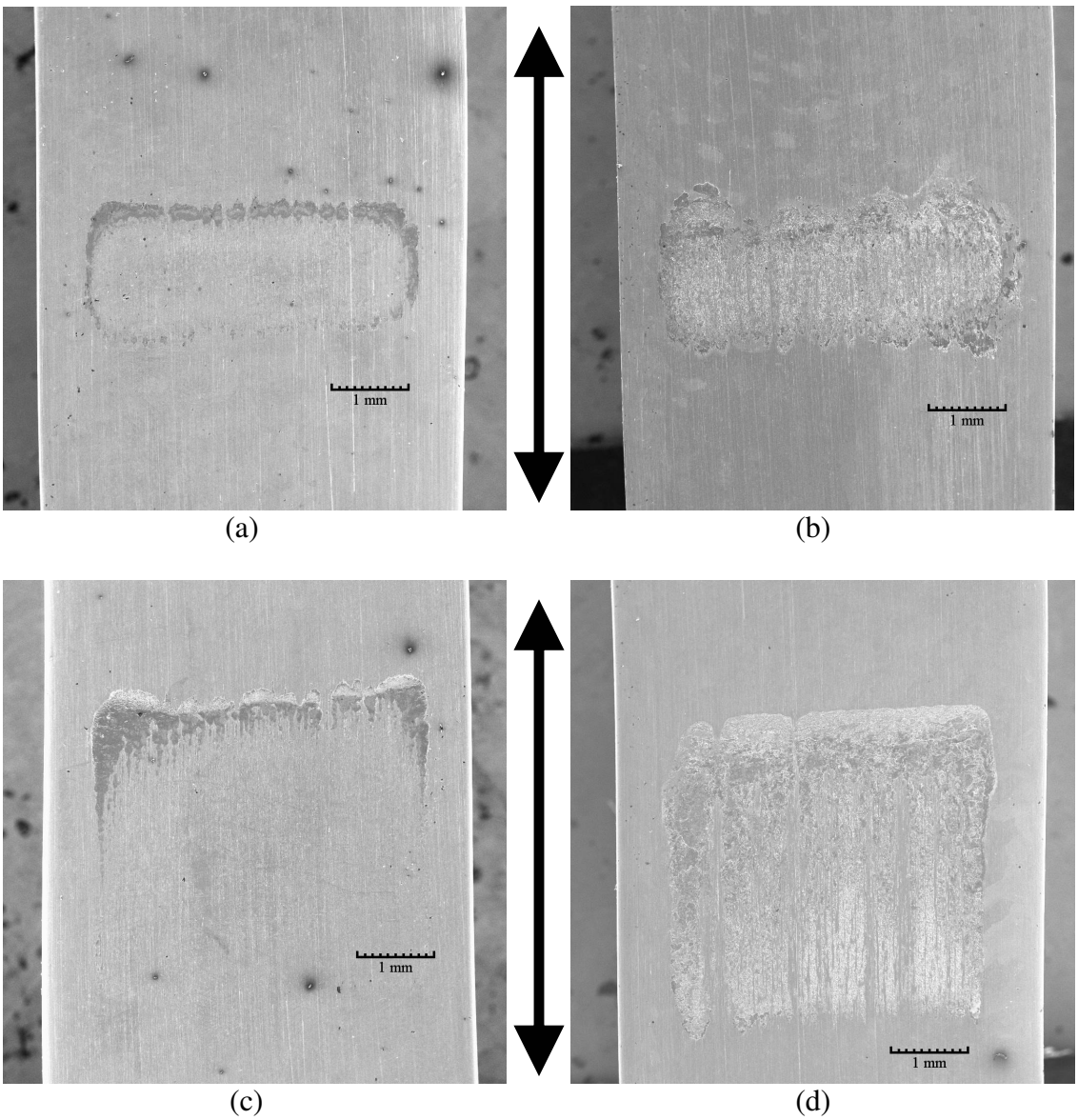


Figure 5.8: SEM images of contact surface scars for (a) specimen 4A ($\sigma_a$ = 100 MPa, R = -1, cylindrical pads) (b) specimen 9C ($\sigma_a$ = 275 MPa, R = -1, cylindrical pads) (c) specimen 5B ($\sigma_a$ = 100 MPa, R = -1, flat pads), and (d) specimen 2C ($\sigma_a$ = 250 MPa, R = -1, flat pads). The arrows indicate the axial loading direction.

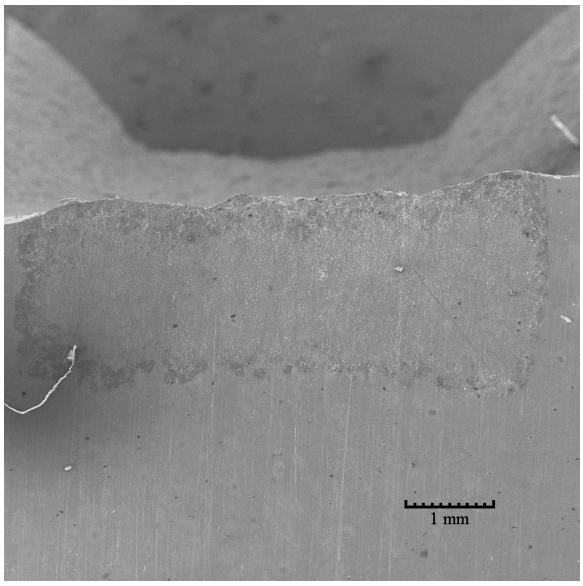

Figure 5.9: SEM image of fretting scar where dominant crack initiated for specimen 7C.

The stick and slip regions for these tests were also analyzed quantitatively. A summary of dimensions of the stick and slip regions is reported in Table 5.3 where 2*a*' is the full contact scar width, 2*c*' is the contact scar stick region width, L is the contact scar leading edge partial slip width, and T is the trailing edge contact scar partial slip width, as defined in Figure 5.10. The primes are used to distinguish between the measured values of the full contact scar stick and slip region after cyclic fatigue loading and the instantaneous contact width predicted by Hertzian theory. All of the measurements were taken across the middle thickness of the specimens. Not surprisingly, for the cylindrical contacts, the test with the higher stress amplitude had larger regions of slip. For the flat contacts, the higher stress amplitude led to a larger trailing edge for the scars.

The local coefficient of friction in the slip regions can be estimated for the cylindrical contacts when the frictional force range has reached a stabile value during the test. Using the Mindlin solution, similar to Fouvry et al. (1998) and Wallace and Neu (2003), the local coefficient of friction can be given by (reference Equation 2.11)

$$\mu_{local} = \frac{Q_a}{P\left(1-\left(\frac{c'}{a'}\right)^2\right)} \tag{5.1}$$

where $Q_a$ is the stabilized frictional force amplitude, P is the normal force applied to each pad foot, 2c' is the stick region width, and 2a' is the full contact width. Values for the local coefficient of friction for specimens 4A and 9C are reported in Table 5.3. The local coefficient of friction for specimen 4A ($\sigma_a$ = 100 MPa) was in the same range as the values reported by Wallace (2001). However, for the higher stress amplitude test with specimen 9C ($\sigma_a$ = 100 MPa), the coefficient of friction was considerably higher. For this case, the surface roughness in the stick region is higher than the initial roughness. Thus, the coefficient of friction in this region could also be higher. It is likely that this test is operating in the mixed fretting regime, which is characterized by gross slip in the initial cycles, which increases the roughness of the surface, and then it transitions to partial slip in the later cycles. In this case, it is often difficult to determine the exact stick/slip boundary at stabilized response from scar observations with certainty because fretting damage will be present in parts of the stick region, too.

Table 5.3: Measurements of surface scar features for cylindrical pads and flat pads.

| Cylindrical Pads | | | | | | | | | | |
|---|---|---|---|---|---|---|---|---|---|---|
| Specimen | $\sigma_a$ (MPa) | $Q_a$ (N) | | Scar Side | 2a' (mm) | 2c' (mm) | c'/a' | L (mm) | T (mm) | $\mu_{local}$ |
| 4A | 100 | 560.5 | Upper Grip | Pad 1 | 1.62 | 1.16 | 0.72 | 0.20 | 0.28 | 0.86 |
| | | | | Pad 2 | 1.52 | 1.17 | 0.77 | 0.15 | 0.21 | 1.03 |
| | | | Lower Grip | Pad 1 | 1.68 | 1.17 | 0.70 | 0.21 | 0.34 | 0.81 |
| | | | | Pad 2 | 1.60 | 1.10 | 0.69 | 0.22 | 0.26 | 0.79 |
| 9C | 275 | 1279.3 | Upper Grip | Pad 1 | 1.49 | 0.82 | 0.55 | 0.25 | 0.42 | 1.37 |
| | | | | Pad 2 | 1.71 | 0.74 | 0.43 | 0.32 | 0.69 | 1.17 |
| | | | Lower Grip | Pad 1 | 1.26 | 0.58 | 0.46 | 0.24 | 0.45 | 1.21 |
| | | | | Pad 2 | 1.30 | 0.53 | 0.41 | 0.30 | 0.44 | 1.14 |

| Flat Pads | | | | | |
|---|---|---|---|---|---|
| Specimen | $\sigma_a$ (MPa) | $Q_a$ (N) | | Scar Side | T (mm) |
| 5B | 100 | 645.2 | Upper Grip | Pad 1 | 0.30 |
| | | | | Pad 2 | 0.42 |
| | | | Lower Grip | Pad 1 | 0.40 |
| | | | | Pad 2 | 0.39 |
| 2C | 275 | 1538.0 | Upper Grip | Pad 1 | 1.30 |
| | | | | Pad 2 | 0.59 |
| | | | Lower Grip | Pad 1 | 0.94 |
| | | | | Pad 2 | 0.77 |

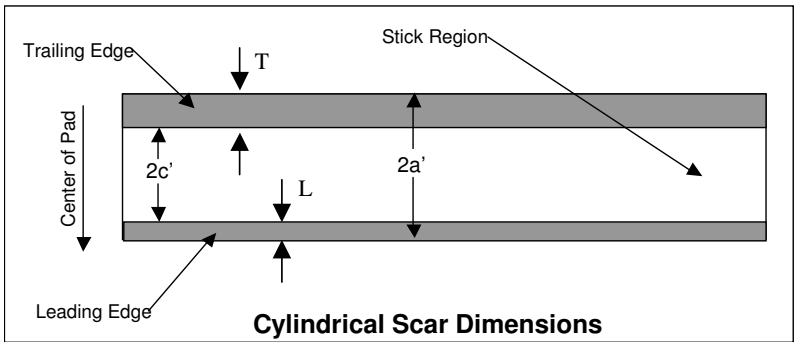


(a)

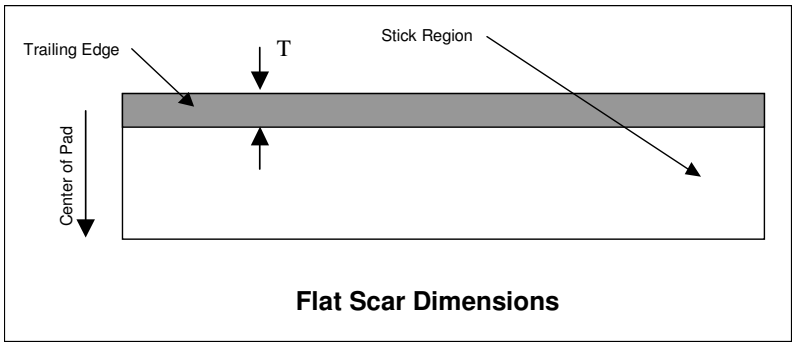


(b)

Figure 5.10: Schematic of fretting scars for (a) cylindrical pads and (b) flat pads.

Specimen 2B ($\sigma_a$ = 250 MPa, R = -1, cylindrical pads) was sectioned and observed microscopically. The dominant crack in this specimen formed at the fretting scar located on the pad 1 side on the half of the specimen that was closest to the lower grip in the hydraulic testing machine. Figure 5.11 shows images of two of the scars that did not have a dominant crack. These scars were on the half of the specimen closest to the upper grip in the hydraulic testing machine. Despite the fact that dominant cracks did not grow from these scars, cracks were still present on both of them. The cracks appear to be smaller than 0.1 mm long.

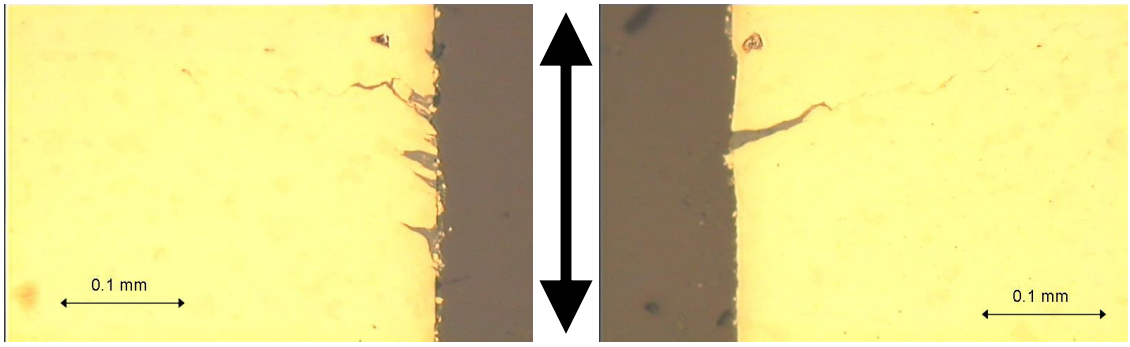


Figure 5.11: Optical microscope images of fretting scars for specimen 2B ($\sigma_a$ = 250 MPa, R = -1, cylindrical pads) for the (a) pad 1 side and (b) pad 2 side. The arrows indicate the axial loading direction.

### 5.4 Effects of Low Plasticity Burnishing

Prior to undergoing fretting fatigue testing, specimen 6C was treated with low plasticity burnishing on the surface of the thin sides in the gage section of the specimen (i.e., the sides that that experience fretting) (see Figure 2.19). The specimen did not fail due to a crack that formed at the fretting contacts. Instead, the critical crack initiated at the edge of the LPB treatment where the gage section transitions to the wider section of the specimen, illustrated in Figure 5.13. An optical microscope was used to locate cracks that had initiated on the surface of the specimen. Several cracks were found along each of the four wide edges of the gage section. An example of two of these cracks can be seen in Figure 5.12. The crack in Figure 5.12 (a) is located 5.3 mm above the lower fretting scar and the crack in Figure 5.12 (b) is located 4.0 mm below the lower fretting scar, as shown in Figure 5.12. The right sides of the specimens shown in Figure 5.12 appear slightly darker because the edges were rounded during the LPB process. The crack in Figure 5.12 (b) appears to have initiated at the edge of this darker region and propagated in both directions. Some of the cracks propagated all the way to the edge of the specimen. However, all of the cracks arrested before they reached the untreated area of the specimen.

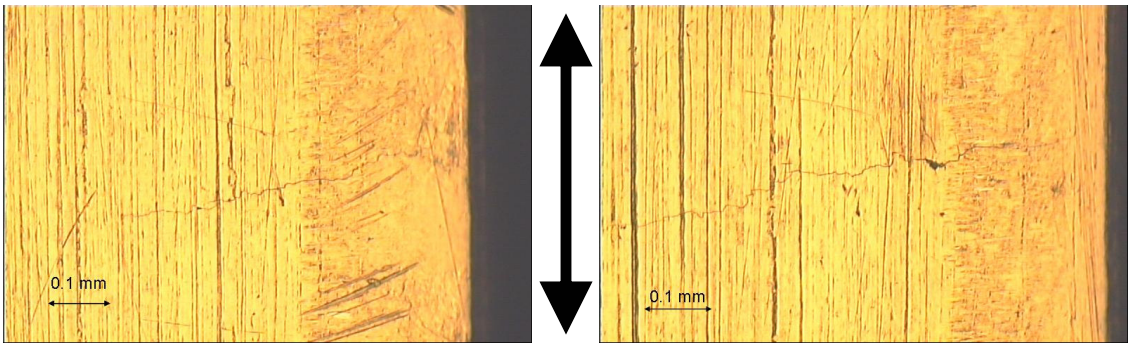


(a) (b)

Figure 5.12: Optical microscope images of cracks located on the wide surface of specimen 6C. The arrows indicate the axial loading direction.

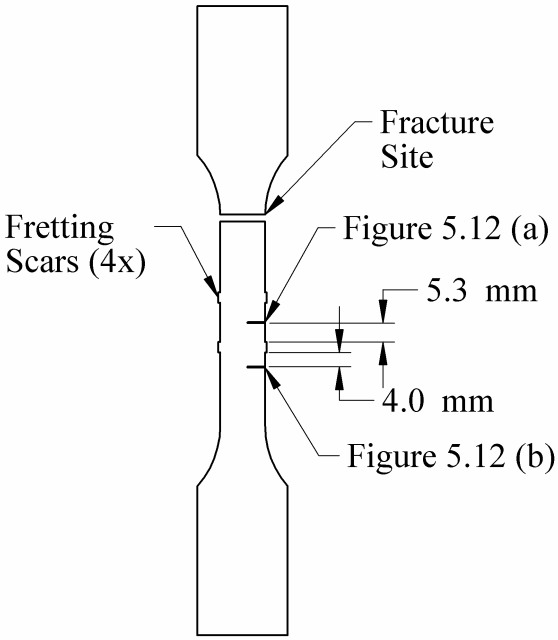


Figure 5.13: Schematic locating cracks shown in Figure 5.12.

Specimen 6C was also sectioned so that it could be determined if cracks initiated at the fretting scars. The thin dimension of the gage section was cut so that a cross section of the fretting scars could be viewed. For the LPB specimen, all four of the fretting scars had multiple small cracks originating from the trailing edge, but no other cracks were present away from the fretting site. The cracks pointed toward the center of

the specimen as shown in Figure 5.14. The cracks appear to be filled with debris and likely contain oxide particles. Previous work by Swalla (2003) using energy dispersive spectroscopy (EDS) showed the presence of oxide particles resulting from similar conditions. Although the exact residual stress profile for this LPB treated specimen is not currently available, the residual stress profiles caused by different surface treatments shown in Figure 2.17 indicate that the cracks arrested near the depth of the material where the maximum residual compressive stresses from the LPB treatment are present. However, these cracks are long enough that they would have grown through the depth of a typical compressive layer formed by shot peening. Specimen 4A ($\sigma_a$ = 100 MPa, R = -1), which was from a runout test, was also sectioned in a similar manner for comparison. However, no cracks could be found in the fretting region of this specimen.

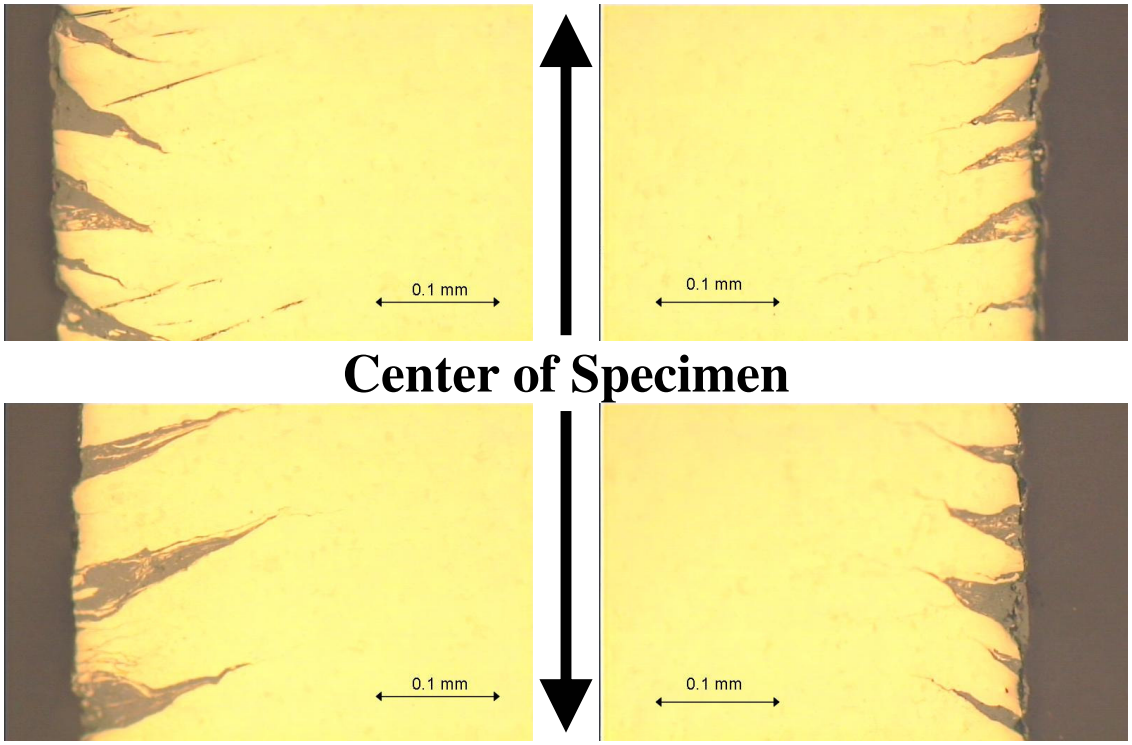


Figure 5.14: Optical microscope images of the cross section near the trailing edge of the four fretting scars from specimen 6C. The arrows indicate the axial loading direction.

The evolution of the frictional force range exhibits the behavior that would be expected to be caused by the presence of the cracks that were observed microscopically in the LPB treated specimen. The frictional force range for the LPB treated specimen 6C in Figure 5.15 (a) shows an initial increase peaking at about 60,000 cycles and then exhibits a long and gradual decline, unlike the typical stabile frictional force range shown in Figure 5.15 (b) for the untreated specimen 9C, which was tested with equal loading conditions. The decline begins after roughly the same amount of cycles that it took for a dominant crack to be initiated in the untreated specimen 9C. It is likely that the onset in the decline in the frictional force range is associated with the presence of small cracks that change the compliance of the interfacial shear. Normally, these cracks would quickly grow to a dominant crack that would cause a rapid drop in the frictional force range, but since crack growth was inhibited by the residual compressive stresses from the LPB treatment, the test continued, and the frictional force range gradually decreased as new cracks nucleated. A decline in the frictional force range can also be caused by third body wear particles. These particles are especially likely to be present when there is considerable scar damage, which was the case for the fretting scars on the LPB treated specimen.

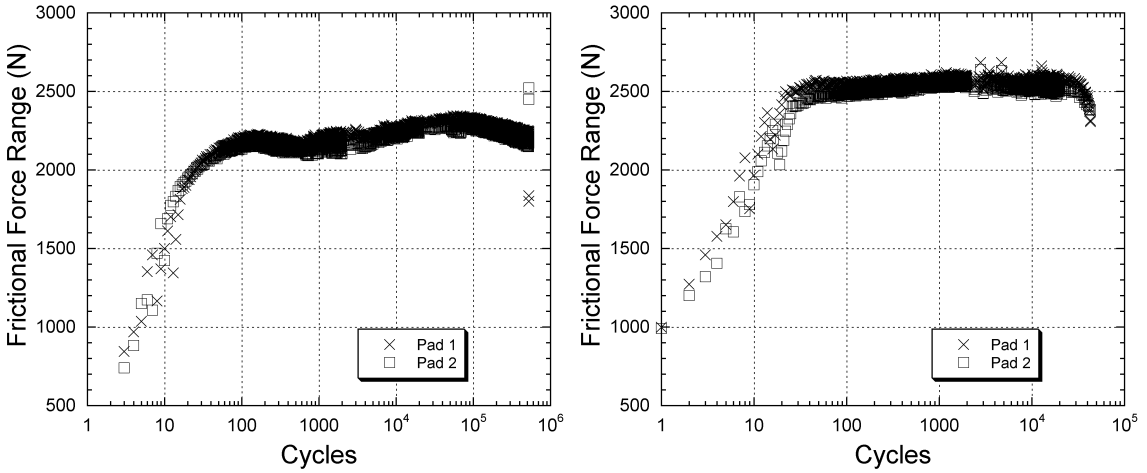


Figure 5.15: Plots of frictional force range vs. cycles on a log scale for (a) specimen 6C ($\sigma_a$ = 275 MPa, R = -1, cylindrical pads, LPB) and (b) specimen 9C ($\sigma_a$ = 275 MPa, R = -1, cylindrical pads).

### 5.5 Influence of Bulk Mean Stress

A regression analysis was performed on all of the Georgia Institute of Technology fretting fatigue data, not including the runout tests and the LPB test, to determine the value of $\gamma$ in the Walker equation (Equation 3.1). The Walker equivalent stress, representing the stress range for R = 0, using $\gamma = 0.662$, is plotted in Figure 5.16. The value for the fretting fatigue $\gamma$ was considerably higher than the value, $\gamma = 0.272$, needed to collapse the smooth fatigue data presented in section 3.2. This indicates that the fretting fatigue lives are less sensitive to mean stress and more sensitive to stress range compared to smooth fatigue. Compared to smooth fatigue specimens (MIL-HDBK-5G, 2003), notched fatigue specimens also tend to have higher values for $\gamma$. This is consistent with the idea that fretting is essentially a sharp stress concentration in the contact region. Thus, near the fretting contact, plastic deformation results in the relaxation of the remotely applied mean stress with cycling. The relaxation appears to occur rapidly (i.e., less than 1000 cycles). The knockdown factor for fretting fatigue based on the Walker equivalent stress (R = 0) at $10^7$ cycles is 4.0.

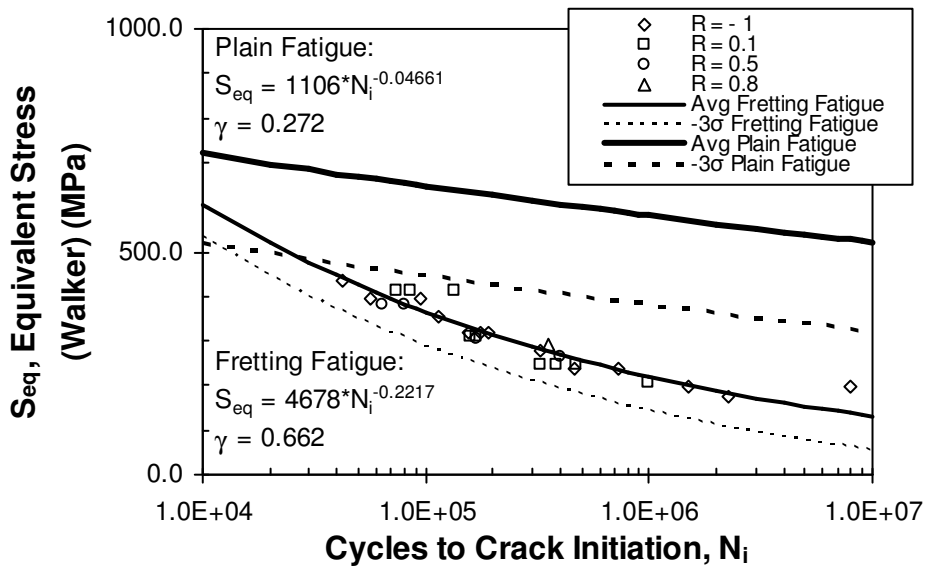


Figure 5.16: Plot of Walker equivalent stress (stress range for zero-to-tension (R = 0) loading) versus fretting fatigue life.

Using the single power law regression analysis fit of all the fretting fatigue data in terms of the Walker equivalent stress, the fretting fatigue strengths at $10^6$ and $10^7$ cycles were estimated. $S_{eq}$ at $10^6$ is 219 MPa and $10^7$ cycles is 131 MPa. Hence, the fretting fatigue strengths for R = 0 based on stress amplitude at $10^6$ and $10^7$ cycles are 109 MPa and 66 MPa, respectively. Table 5.4 shows the predicted fretting fatigue strengths for other values of R and experimental estimates for a fretting fatigue limit at $10^7$ cycles. The experimental values fall between the predicted values at $10^6$ and $10^7$ cycles. The Walker equation is not especially accurate at predicting fretting fatigue lives at $10^7$ cycles. This may be partially due to the fact that the runout tests were not included in the regression analysis. Additionally, a two term regression analysis may improve the results at $10^7$ cycles.

Table 5.4: Estimates for fretting fatigue strength based on stress amplitude for different stress ratios found experimentally and using the Walker Equation.

| Stress Ratio, R | Experimental, $10^7$ Cycles (MPa) | Walker, $10^6$ Cycles (MPa) | Walker, $10^7$ Cycles (MPa) |
|---|---|---|---|
| -1 | 100 ± 10 | 138 | 83 |
| 0.1 | 80 ± 20 | 106 | 63 |
| 0.5 | 75 ± 20 | 86 | 52 |
| 0.8 | 60 ± 20 | 63 | 38 |

## 5.6 Driving Force Parameter

A model proposed by Ahmad and Santhosh (2004) that uses the strength of the singularity to predict crack initiation is evaluated. The parameter used by Ahmad and Santhosh is essentially the H parameter derived in section 2.6.3, but is numerically determined using finite element analysis (FEA) of our fretting fatigue test configuration (Figure 2.23).

The data presented in Table 5.5 are from tests previously performed on the same material and fretting test configuration by Wallace (2001). Ahmad and Santhosh (2004) determined the driving force parameters for these fretting fatigue tests. The results of their analysis are given in Table 5.5, noted as $\Delta H_{FEA}$. In addition, the values of $\Delta H_{an}$ determined from a simple analytical analysis that does not capture the specific test configuration effects, such as the bulk stress in the fatigue specimen and the particular boundary condition of the test configuration, determined using (reference Equation 2.22)

$$\Delta H_{an} = \frac{\Delta Q}{2(\pi l)^{3/4}} \left( \frac{E^*}{RP} \right)^{1/4} \tag{5.2}$$

are also given in Table 5.5. In the fretting fatigue tests, the strength of the singularity is elevated on the trailing edge of the contact. The results of the two analyses are compared by examining the ratio $\Delta H_{FEA}/\Delta H_{an}$ where $\Delta H_{FEA}$ is the strength of the singularity for the range of $Q$ $(= Q_{max} - Q_{min})$ determined numerically for our test configuration by Ahmad and Santhosh (2004) and $\Delta H_{an}$ is the value for the simple analytical analysis using the measured range of $Q$. The factor of elevation (i.e., $\Delta H_{FEA}/\Delta H_{an}$ value) appears to be nearly independent of the loading parameters, $\sigma_a$, R, and P, for our fretting fatigue test configuration. Here the factor is 1.26. Therefore, using this multiplying factor, the

strength of the singularity for our test configuration can be determined from a simple analytical analysis.

Table 5.5: Comparison of driving force parameters.

| Specimen | R | $\sigma_a$ (MPa) | P (N) | $\Delta Q$ (N) | $N_i$ (Cycles) | $\Delta H_{an}$ (MPa-m$^{1/2}$) | $\Delta H_{FEA}$ (MPa-m$^{1/2}$) | $\Delta H_{FEA}/\Delta H_{an}$ |
|---|---|---|---|---|---|---|---|---|
| 113-S412 | 0.1 | 120 | 1340 | 1130 | 381,000 | 2.92 | 3.68 | 1.26 |
| 113-S323 | 0.1 | 150 | 1340 | 1465 | 160,000 | 3.79 | 4.75 | 1.25 |
| 113-S311 | 0.1 | 150 | 2570 | 1600 | 170,000 | 3.51 | 4.44 | 1.26 |
| 113-S322 | 0.5 | 105 | 1340 | 1000 | 403,000 | 2.58 | 3.20 | 1.24 |
| 113-S321 | 0.5 | 120 | 1340 | 1160 | 170,000 | 3.00 | 3.81 | 1.27 |
| 113-S312 | 0.5 | 150 | 1340 | 1400 | 64,000 | 3.62 | 4.57 | 1.26 |
| 113-S421 | 0.5 | 150 | 2570 | 1600 | 80,000 | 3.51 | 4.44 | 1.26 |
| | | | | | | | Average: | 1.26 |

Figure 5.17 shows a plot of ΔH versus the fatigue life. The values on this plot for ΔH are estimates using Equation 5.2 from the simple analytical analysis multiplied by 1.26 as given in Equation 5.3.

$$\Delta H = 1.26 * \Delta H_{an} \tag{5.3}$$

It includes data for the tests performed at Georgia Institute of Technology that used cylindrical contacts only. The value for ΔH appears to be leveling off at a lower limit suggesting that there is a threshold value somewhere between 3 and 4 MPa-m$^{1/2}$. The fatigue stress ratio appears to be a secondary driving factor, causing the value of ΔH to be scaled by a small factor for the different stress ratios. The failure life for the LPB specimen, based on ΔH, is considerably longer than the untreated specimens. However, ΔH did successfully predict that cracks would nucleate in the fretting region as observed experimentally. These cracks did not grow to catastrophic cracks due to compressive residual stresses that were present from the LPB treatment. Thus, ΔH is effective at predicting crack nucleation in the fretting region, but not crack initiation, which includes

both the time for crack nucleation and microcrack growth, which is affected by the residual stress field at the fretting site. A possible way to confirm this hypothesis would be to run a test on an LPB treated specimen, stop the test at the cycle count that lead to a fretting fatigue failure in an untreated specimen, and examine the LPB treated specimen for cracks.

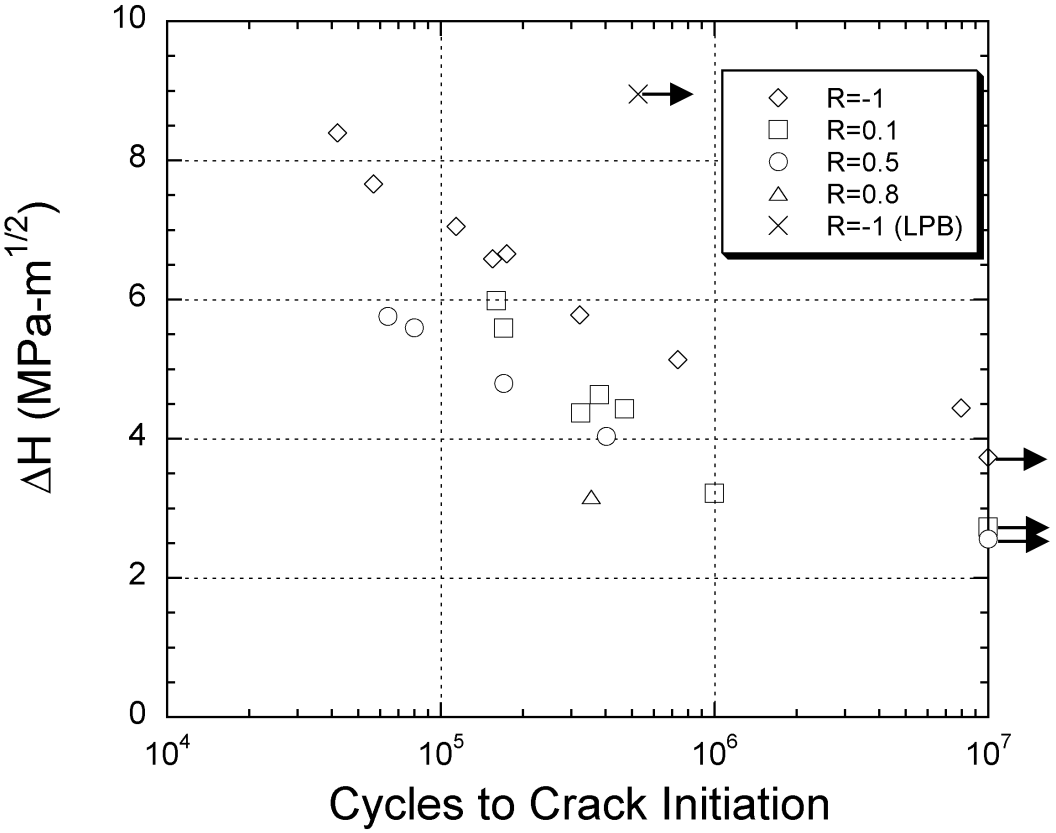


Figure 5.17: Plot of driving force parameter versus fretting fatigue life.

# CHAPTER VI

# CONCLUSIONS

Several fretting fatigue tests consisting of Ti-6Al-4V on Ti-6Al-4V contacts were conducted. These tests have contributed to a test program at Georgia Institute of Technology that has analyzed many parameters involved in fretting fatigue. The focus of the current study was to address stress amplitude, stress ratio, and contact geometry. This large body of tests can be used to validate potential design parameters and life prediction models.

The remotely applied mean value of the stress amplitude has a weaker influence in fretting fatigue life compared to smooth specimen fatigue tests. The Walker equation was used to find an equivalent stress range (for R = 0) for various stress ratios. The empirical constant that was found to relate the data also indicated that the mean stress does not have as large of an effect on fretting fatigue compared to plain (smooth) fatigue. This can be explained by the fact that plastic deformation along the surfaces will cause the mean stress to relax out. Cyclic plastic ratcheting causes the material under the fretting contact to tend toward a fully reversed plastic response. Thus, the nucleation life is controlled by the stabilized response where the mean stress is equal to zero. In fact, it is likely that the mean stress has little effect on crack nucleation and the weak dependence on mean stress is associated with the microcrack growth. Microcrack growth farther away from the fretting region is still controlled by the mean stress since the mean stress does not relax out far from the fretting region.

A sufficient number of tests were run to form estimates of the fretting fatigue limits at $10^7$ cycles for various stress ratios. The higher stress ratios did have lower fretting fatigue limits. Part of this occurrence is due to the fact that the maximum stress for the tests with very high stress ratios such as R = 0.8 approach the yield strength of the material. Still, the fretting fatigue limit was not affected by the stress ratio nearly as much as the plain fatigue limit. The stress amplitudes for plain fatigue differed by a factor of more than 4 for the R = -1 and R = 0.8 cases, while the fretting fatigue limits differed by less than a factor of 2 for the same stress ratios. The Walker equation effectively collapsed the data for the different stress ratios, but it underestimated the stress amplitude for the fretting fatigue limit at $10^7$ cycles by 13-22 MPa. However, the estimates at $10^6$ and $10^7$ cycles did form upper and lower bounds for the experimental values.

Although fretting fatigue is a complex phenomenon with many influencing factors, if the contact is in near stick or partial slip conditions, the range in the strength of the singularity $\Delta H$ at the edge of contact during cycling appears to be a primary driving parameter. This parameter is largely controlled by the tangential force range. A strong correlation has been made between the tangential force range and the fretting fatigue life. This relation holds true even when surface treatments are applied to a specimen. Although the LPB treated specimen in this study had a longer life than expected, cracks still initiated in the fretting region as predicted by the range of tangential force that was present. However, these cracks arrested due to the compressive residual stresses ahead of the cracks. Additional support for this parameter came from the examination of the fretting scars on one of the specimens that did have a dominant fretting crack form. All

of the scars on a specimen should see equal tangential forces. Thus, cracks should nucleate after the same amount of cycles for all four scars, which was shown experimentally to be true. Therefore, this parameter can be a very effective design tool for estimating whether cracks will nucleate, since it can in principle be determined for other geometries assuming the order of the singularity remains the same.

The driving force parameter, H, which measures the strength of the singularity of the stress field at the edge of contact, has the potential to be a very effective design tool. Assuming the local contact geometry can be described by Hertz contact, and after a calibration with a numerical analysis of the exact geometry and loading conditions, the value for H can be estimated using a simple analytical analysis. The calculated values can then easily be compared to threshold values of H for safe design.

Low plasticity burnishing treatment appears to be an effective way to induce a compressive residual stress that inhibits fretting fatigue cracks from growing outside of the fretting damage region. The surface treatment prevented cracks that nucleated at the fretting scars from propagating into dominant cracks that could be driven by the remotely applied cyclic loads. Additional cracks formed at the location of maximum tensile residual stress, a site away from the fretting contacts, but these cracks were also arrested before they could become a dominant crack.

# APPENDIX A

Frictional Force Hysteresis Plots and Frictional Force Range Plots

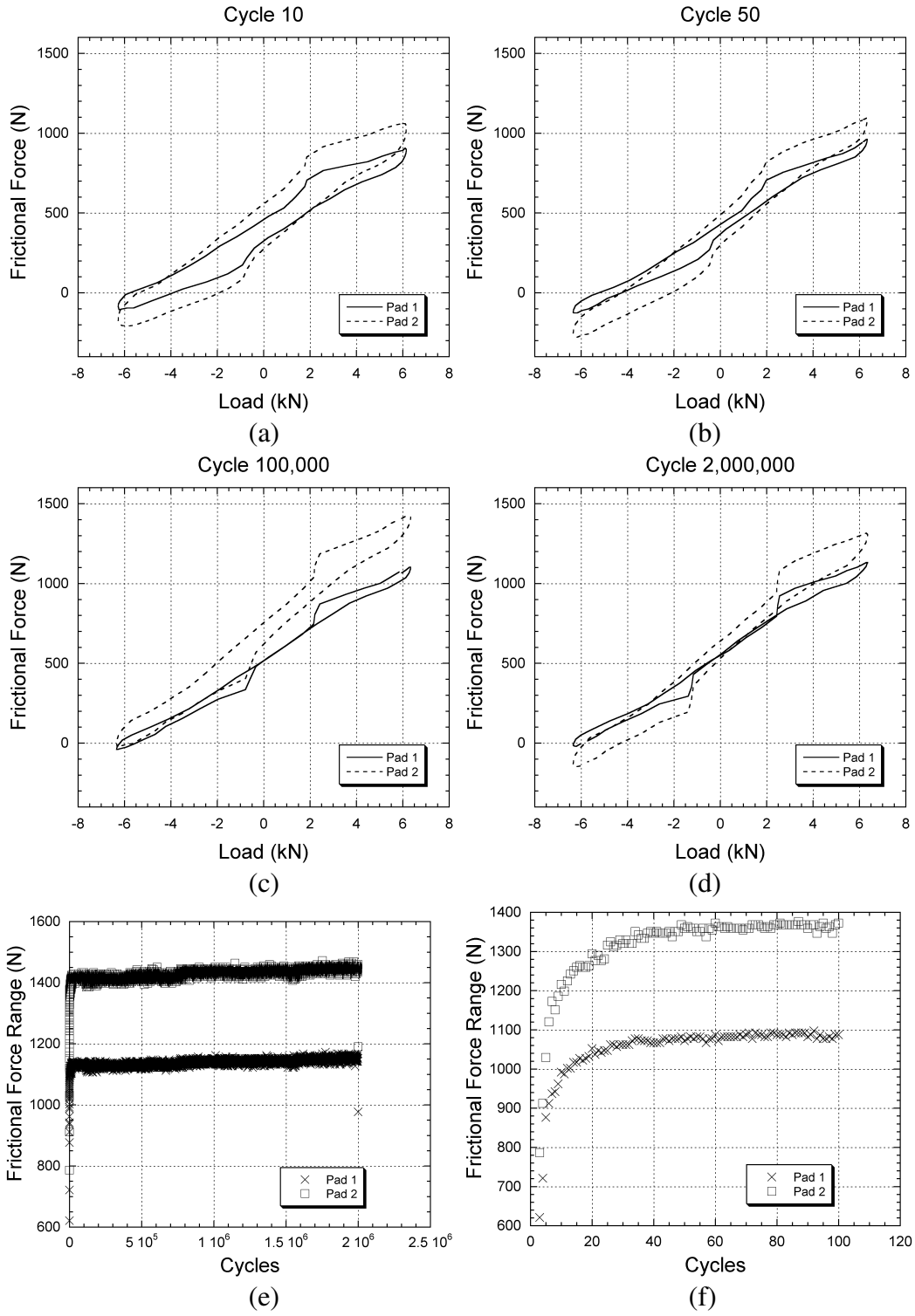


Figure A.1: Plots of frictional force vs. applied load for specimen 5B ($\sigma_a$ = 100 MPa, R = -1, f = 10 Hz, flat pads) at (a) cycle 10, (b) cycle 50, (c) cycle 100,000, and (d) cycle 2,000,000. Plots of frictional force range vs. cycles for specimen 5B for (e) the entire test and (f) the initial cycles.

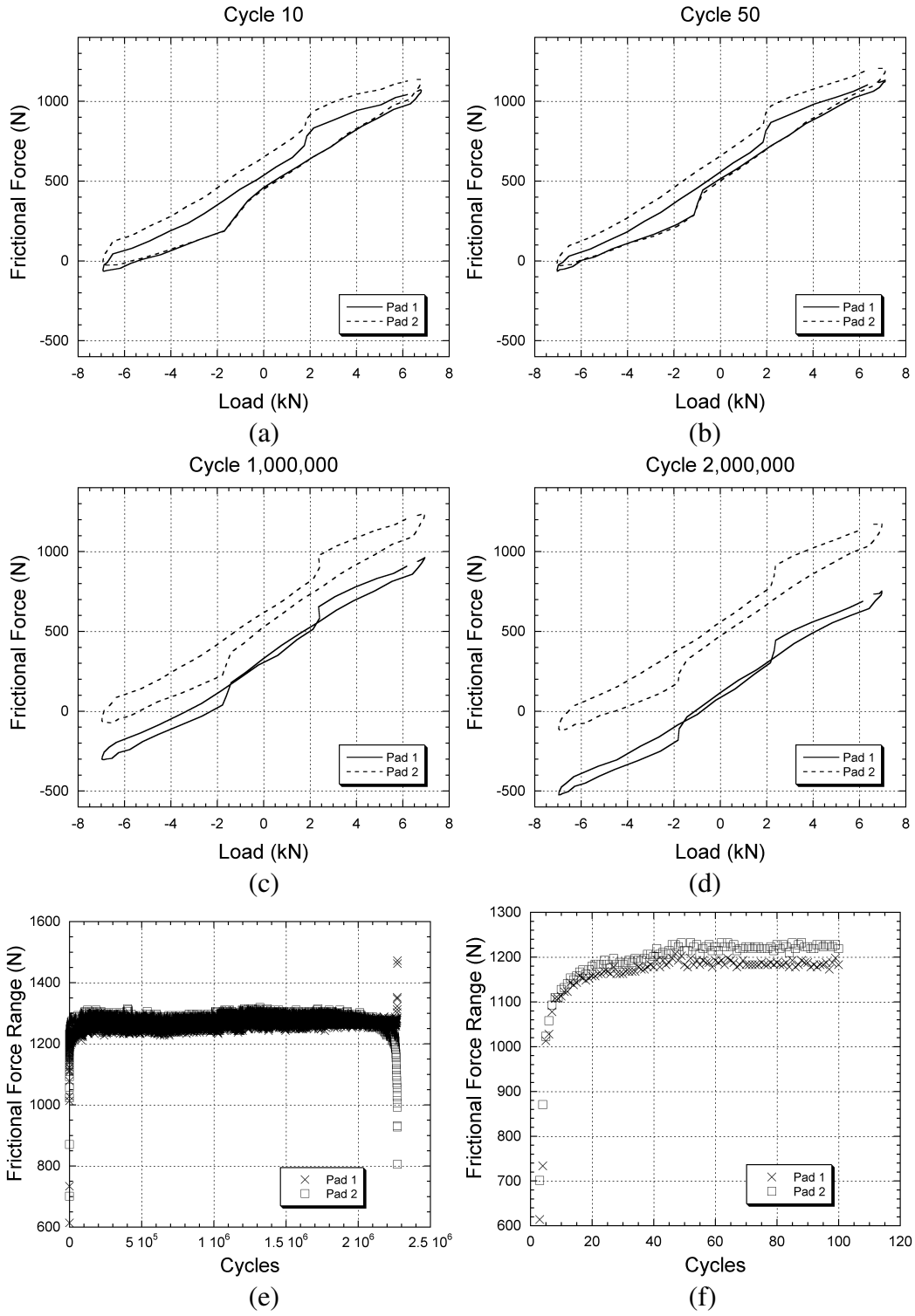


Figure A.2: Plots of frictional force vs. applied load for specimen 7B ($\sigma_a$ = 110 MPa, R = -1, f = 10 Hz, flat pads) at (a) cycle 10, (b) cycle 50, (c) cycle 1,000,000, and (d) cycle 2,000,000. Plots of frictional force range vs. cycles for specimen 7B for (e) the entire test and (f) the initial cycles.

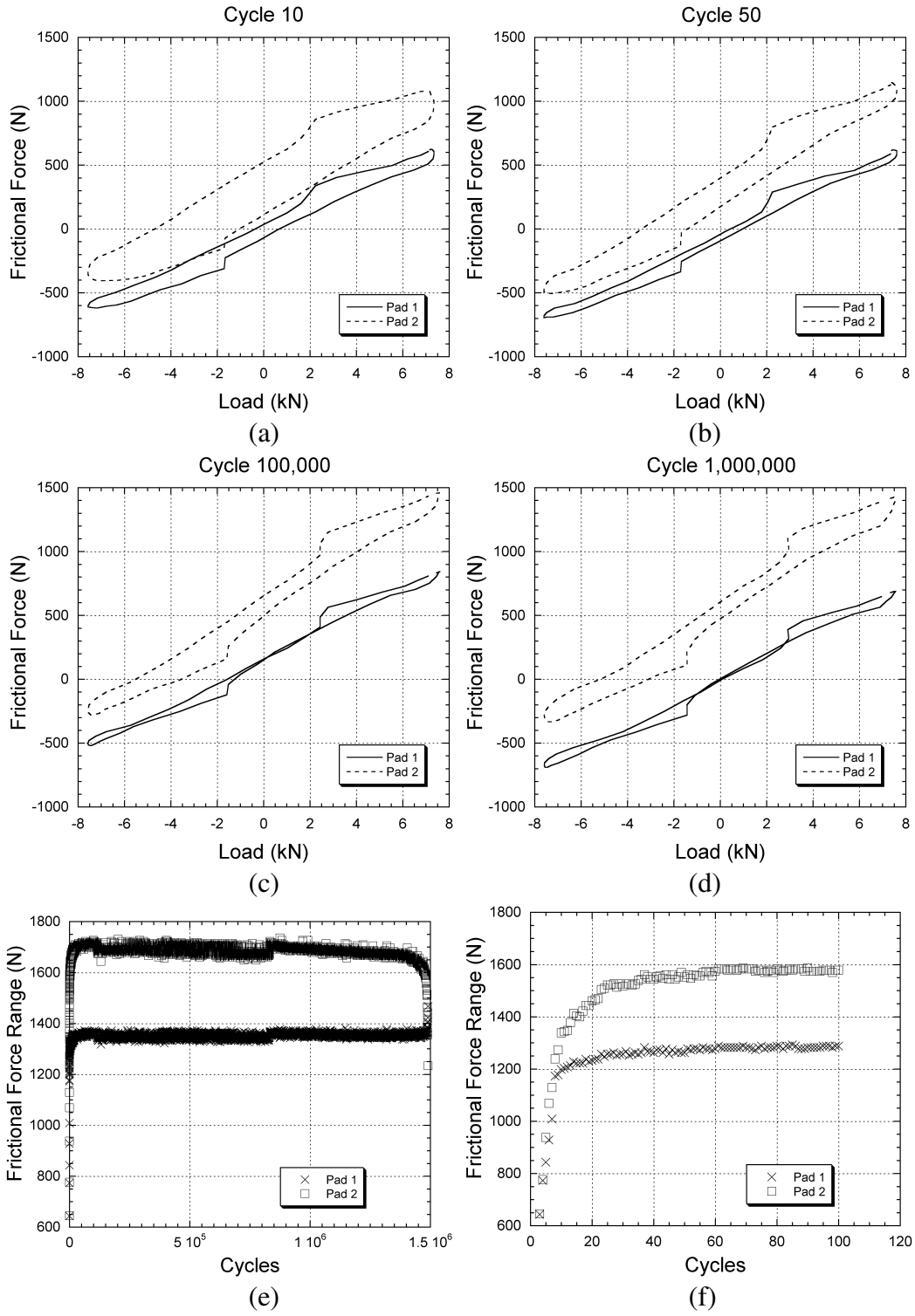


Figure A.3: Plots of frictional force vs. applied load for specimen 9A ($\sigma_a$ = 125 MPa, R = -1, f = 10 Hz, flat pads) at (a) cycle 10, (b) cycle 50, (c) cycle 100,000, and (d) cycle 1,000,000. Plots of frictional force range vs. cycles for specimen 9A for (e) the entire test and (f) the initial cycles.

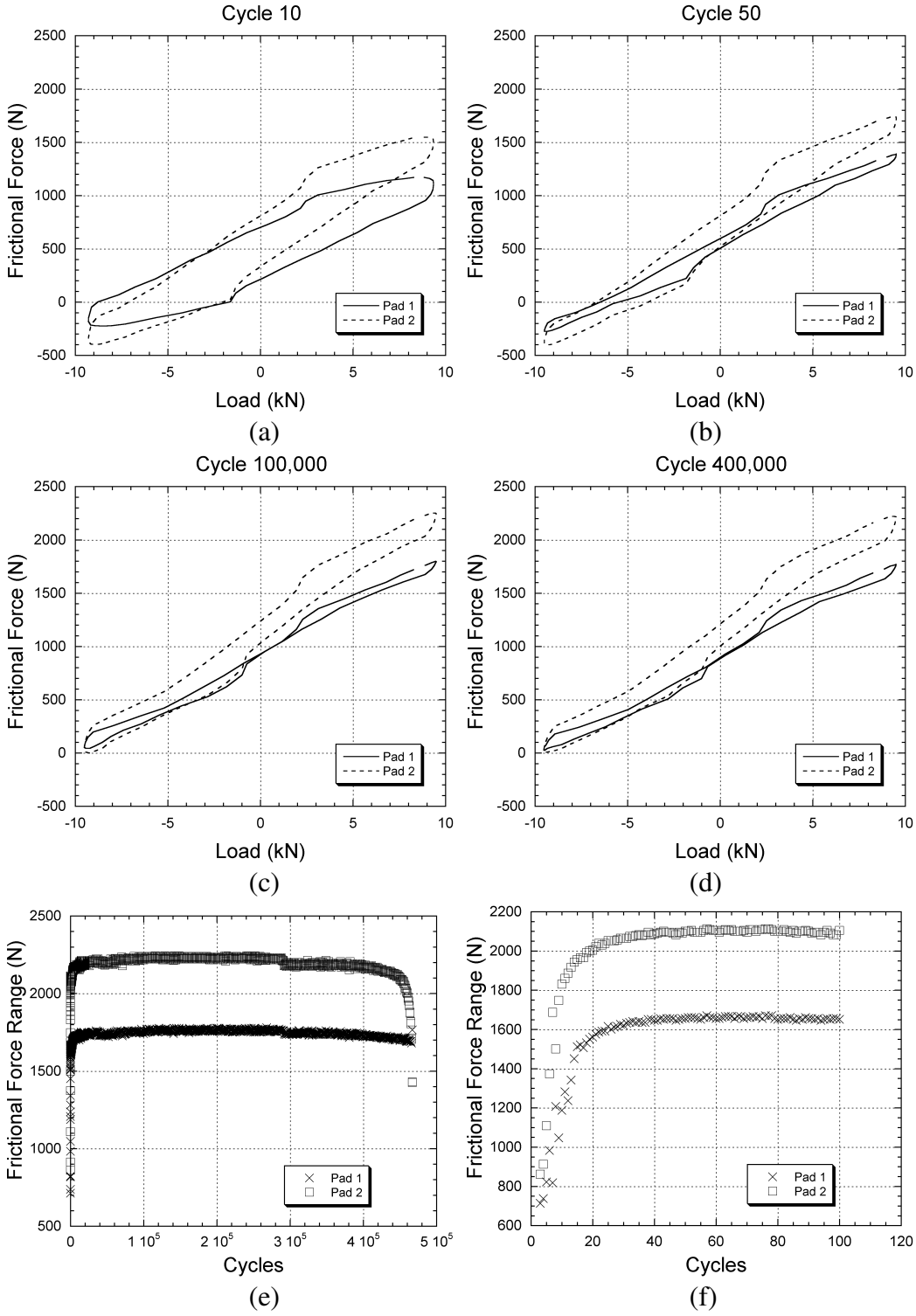


Figure A.4: Plots of frictional force vs. applied load for specimen 5C ($\sigma_a$ = 150 MPa, R = -1, f = 10 Hz, flat pads) at (a) cycle 10, (b) cycle 50, (c) cycle 100,000, and (d) cycle 400,000. Plots of frictional force range vs. cycles for specimen 5C for (e) the entire test and (f) the initial cycles.

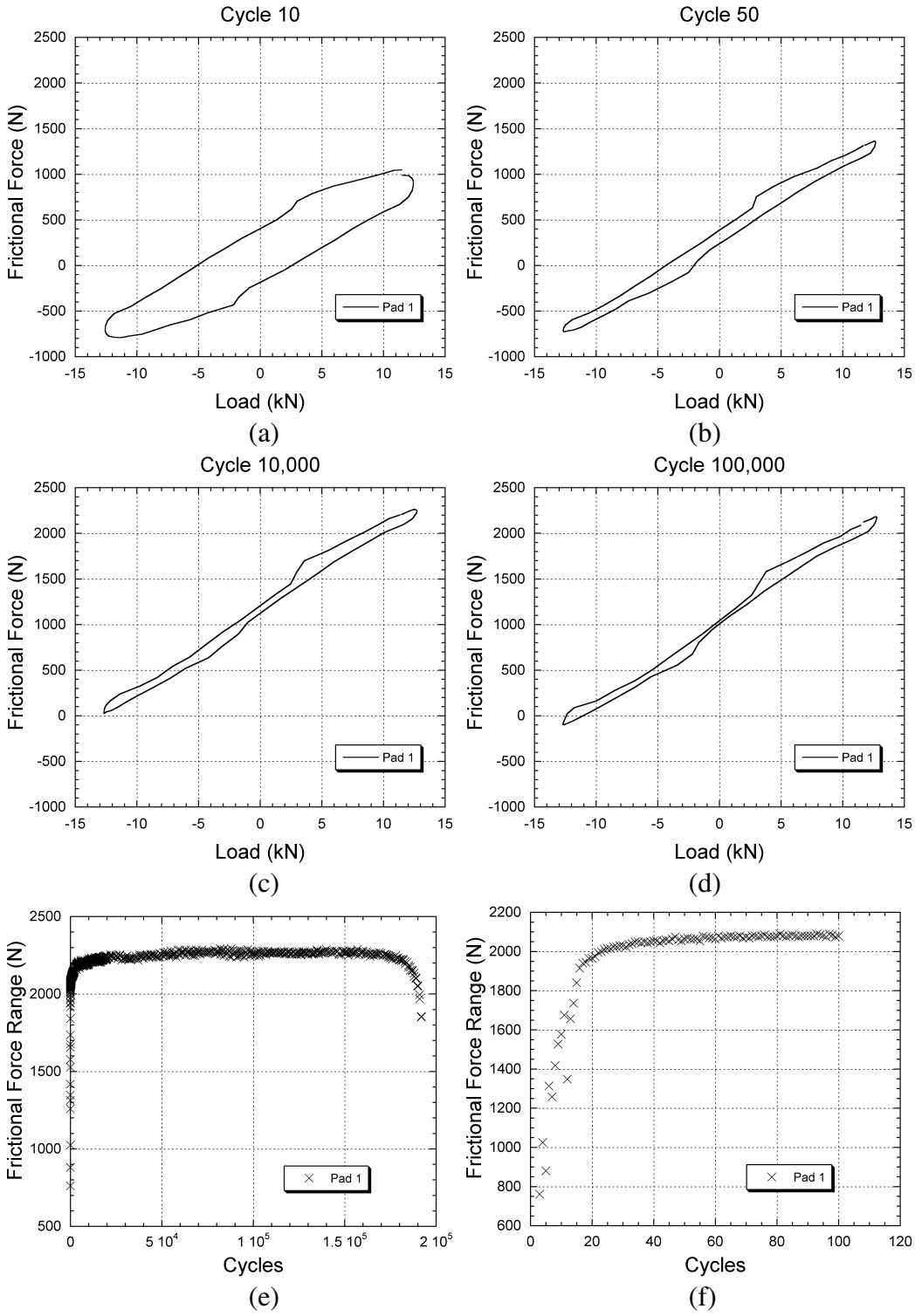


Figure A.5: Plots of frictional force vs. applied load for specimen 3A ($\sigma_a$ = 200 MPa, R = -1, f = 10 Hz, flat pads) at (a) cycle 10, (b) cycle 50, (c) cycle 10,000, and (d) cycle 100,000. Plots of frictional force range vs. cycles for specimen 3A for (e) the entire test and (f) the initial cycles.

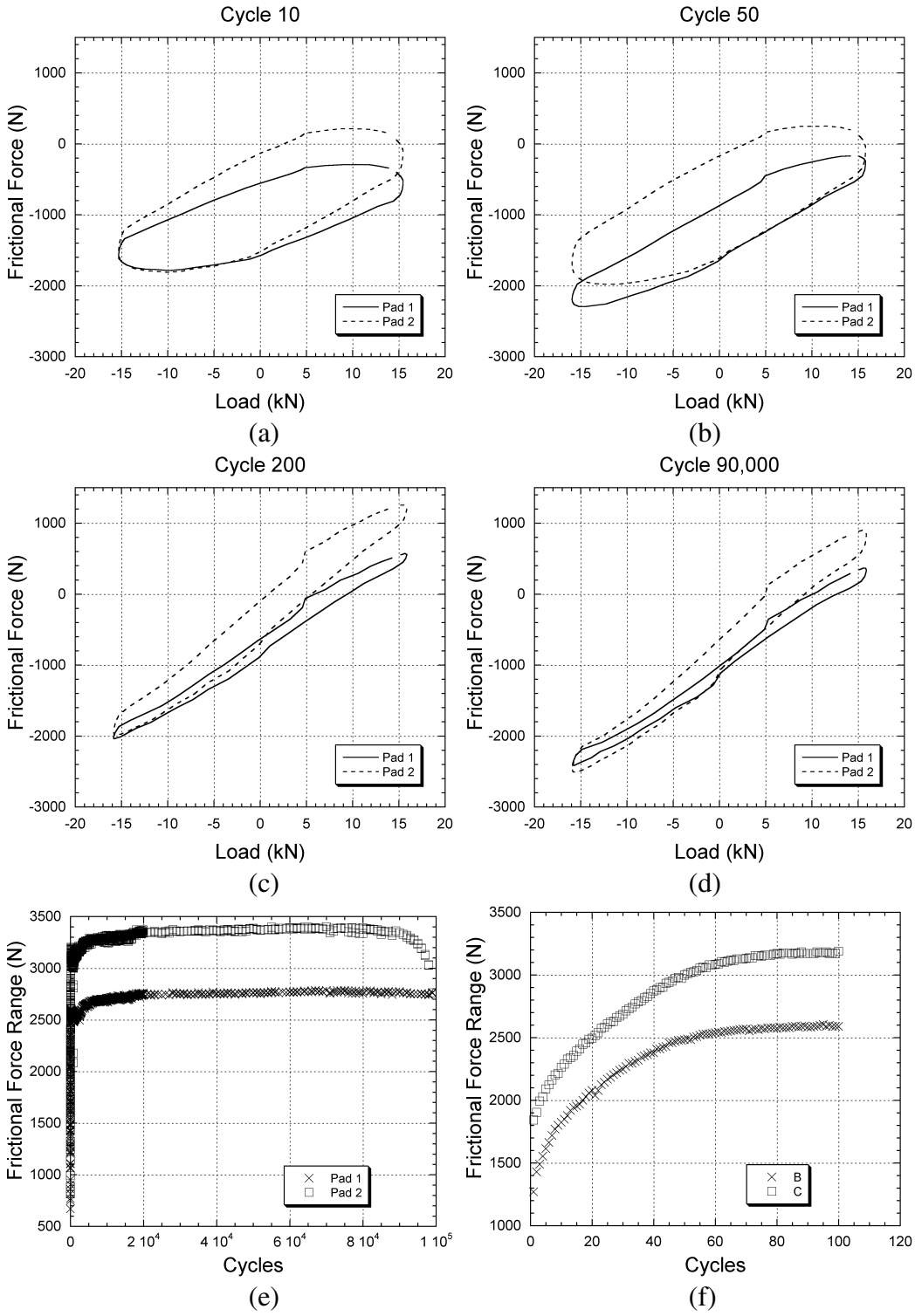


Figure A.6: Plots of frictional force vs. applied load for specimen 2C ($\sigma_a$ = 250 MPa, R = -1, f = 10 Hz, flat pads) at (a) cycle 10, (b) cycle 50, (c) cycle 200, and (d) cycle 90,000. Plots of frictional force range vs. cycles for specimen 2C for (e) the entire test and (f) the initial cycles.

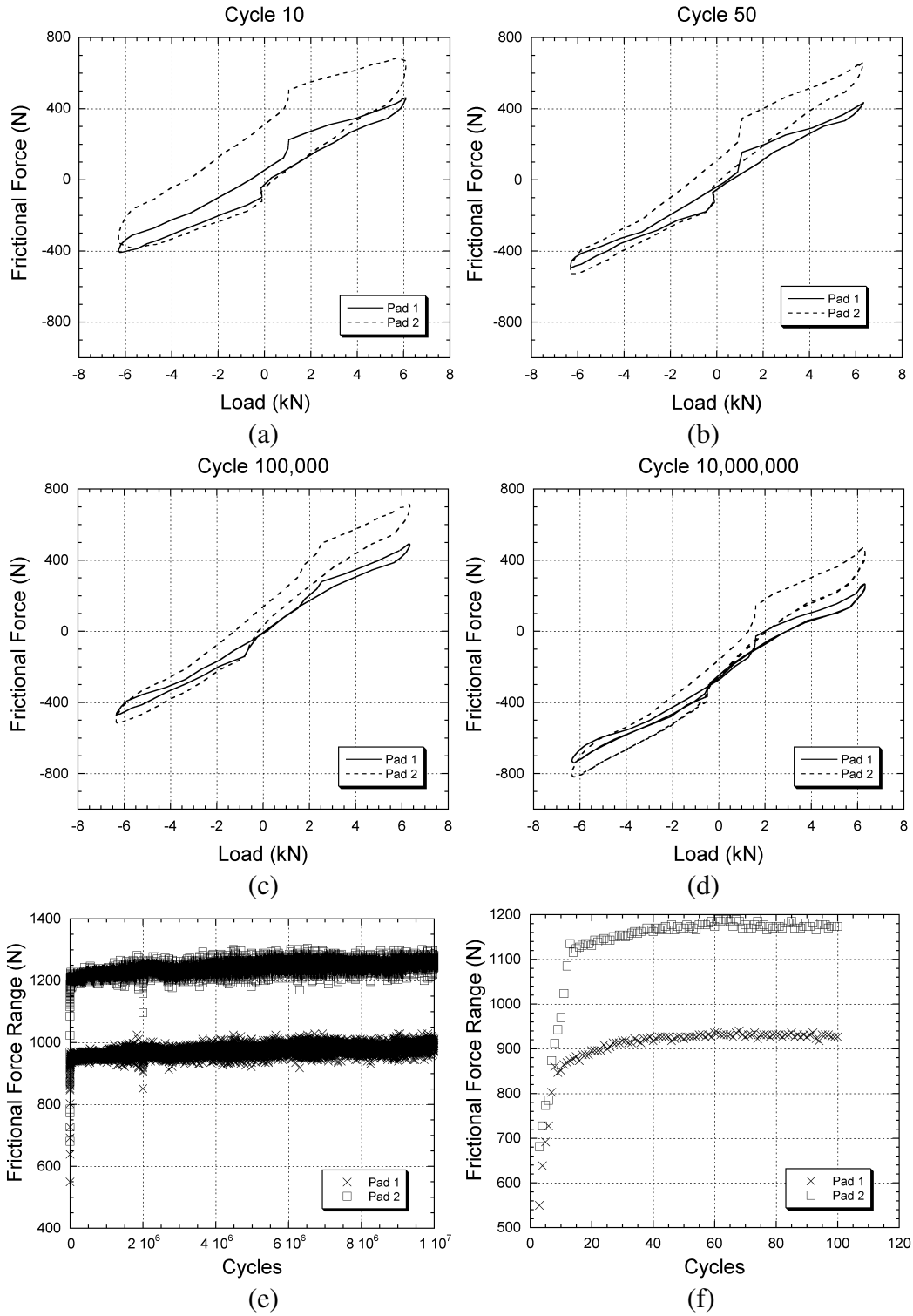


Figure A.7: Plots of frictional force vs. applied load for specimen 4A ($\sigma_a$ = 100 MPa, R = -1, f = 10 Hz, cylindrical pads) at (a) cycle 10, (b) cycle 50, (c) cycle 100,000, and (d) cycle 10,000,000. Plots of frictional force range vs. cycles for specimen 4A for (e) the entire test and (f) the initial cycles.

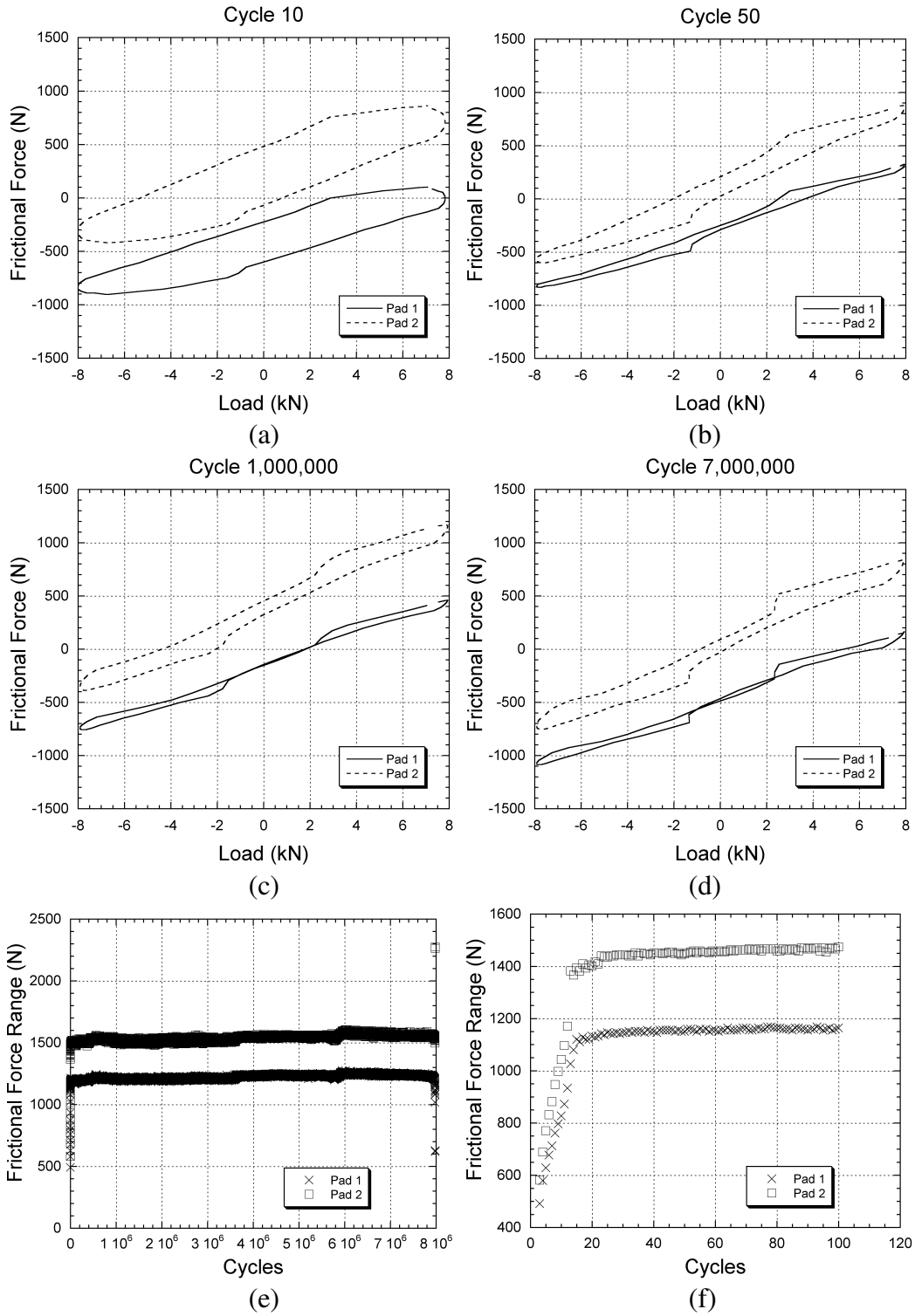


Figure A.8: Plots of frictional force vs. applied load for specimen 3C ($\sigma_a$ = 125 MPa, R = -1, f = 10 Hz, cylindrical pads) at (a) cycle 10, (b) cycle 50, (c) cycle 1,000,000, and (d) cycle 7,000,000. Plots of frictional force range vs. cycles for specimen 3C for (e) the entire test and (f) the initial cycles.

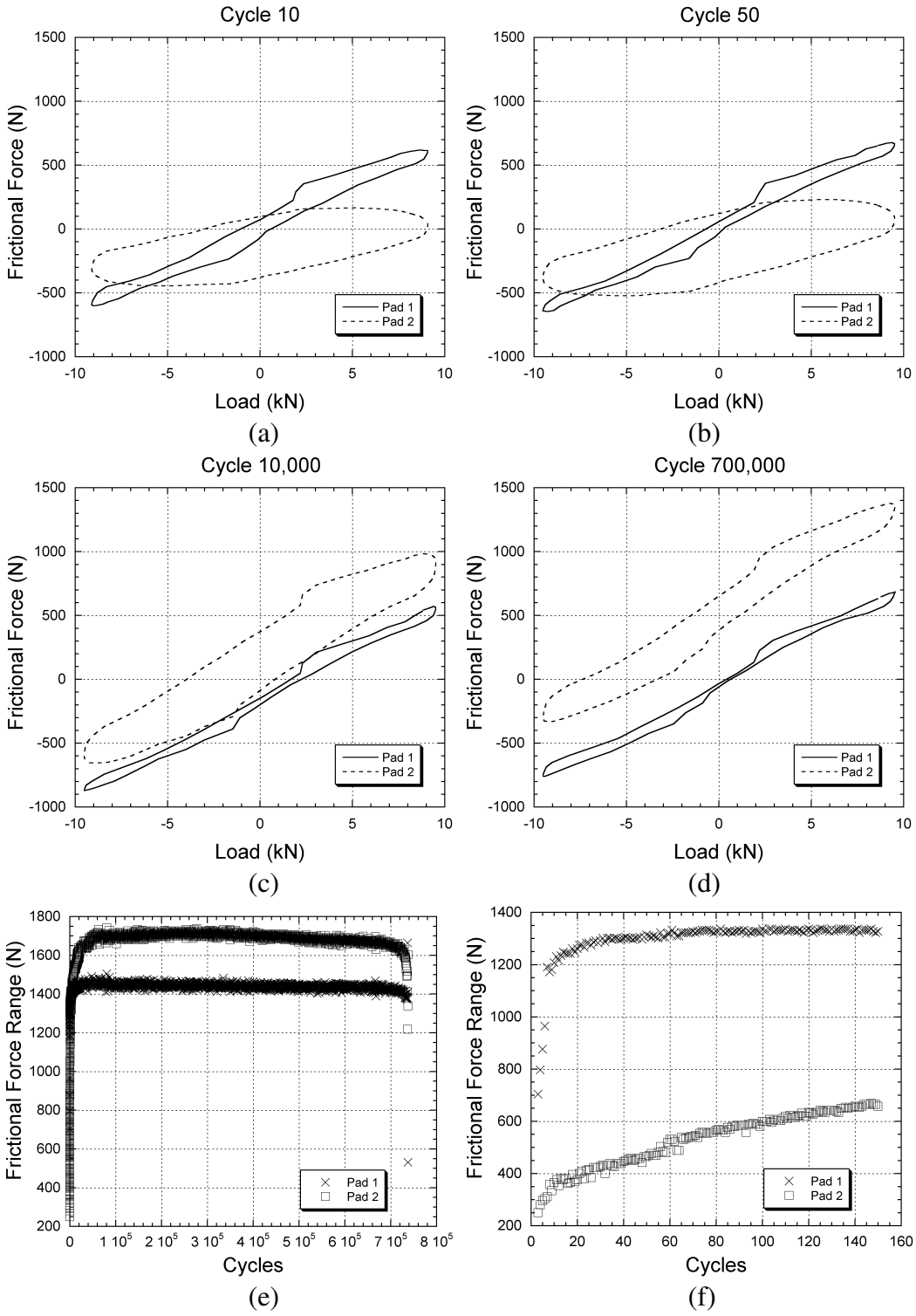


Figure A.9: Plots of frictional force vs. applied load for specimen 4B ($\sigma_a$ = 150 MPa, R = -1, f = 10 Hz, cylindrical pads) at (a) cycle 10, (b) cycle 50, (c) cycle 10,000, and (d) cycle 700,000. Plots of frictional force range vs. cycles for specimen 4B for (e) the entire test and (f) the initial cycles.

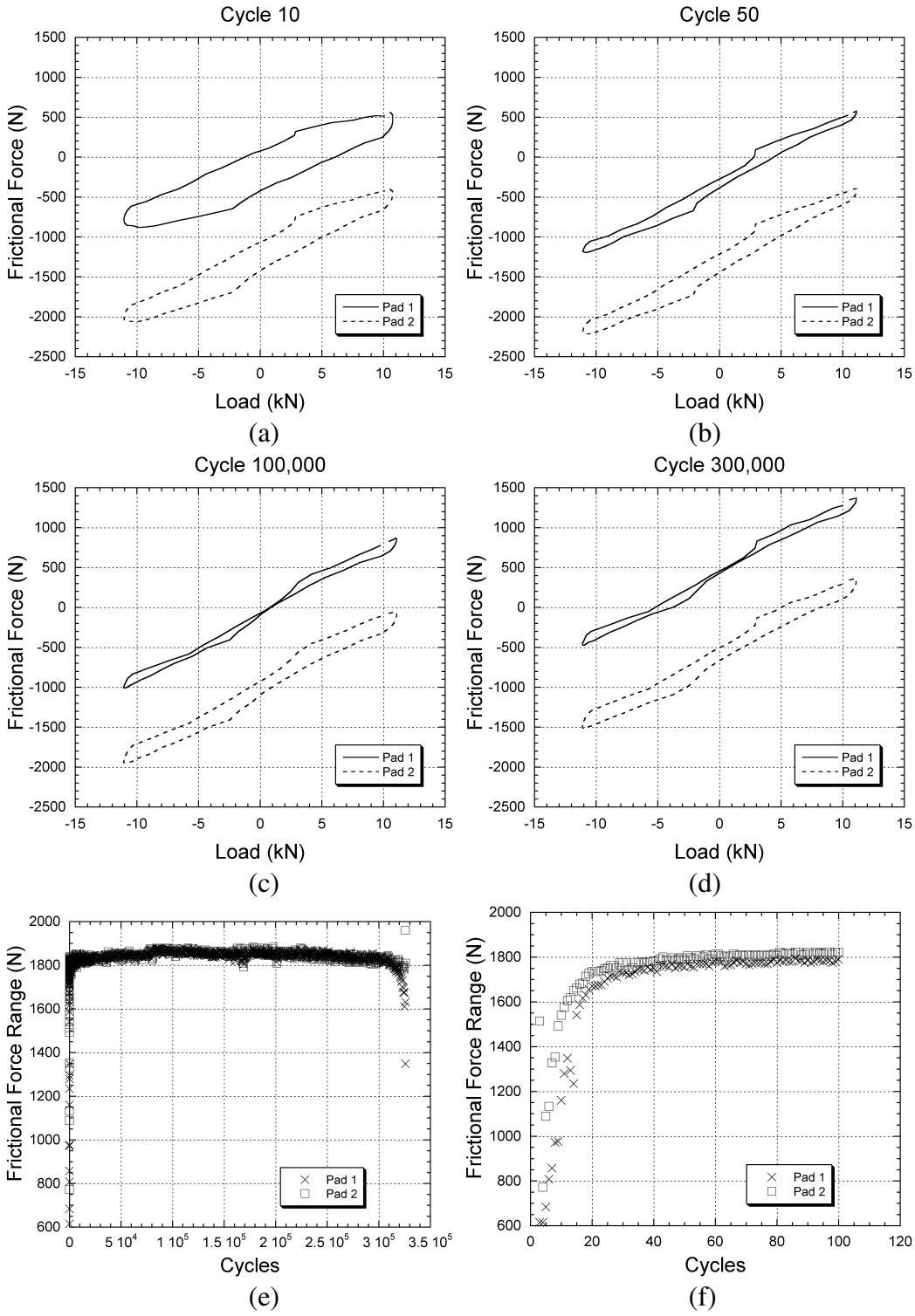


Figure A.10: Plots of frictional force vs. applied load for specimen 8C ($\sigma_a$ = 175 MPa, R = -1, f = 10 Hz, cylindrical pads) at (a) cycle 10, (b) cycle 50, (c) cycle 100,000, and (d) cycle 300,000. Plots of frictional force range vs. cycles for specimen 8C for (e) the entire test and (f) the initial cycles.

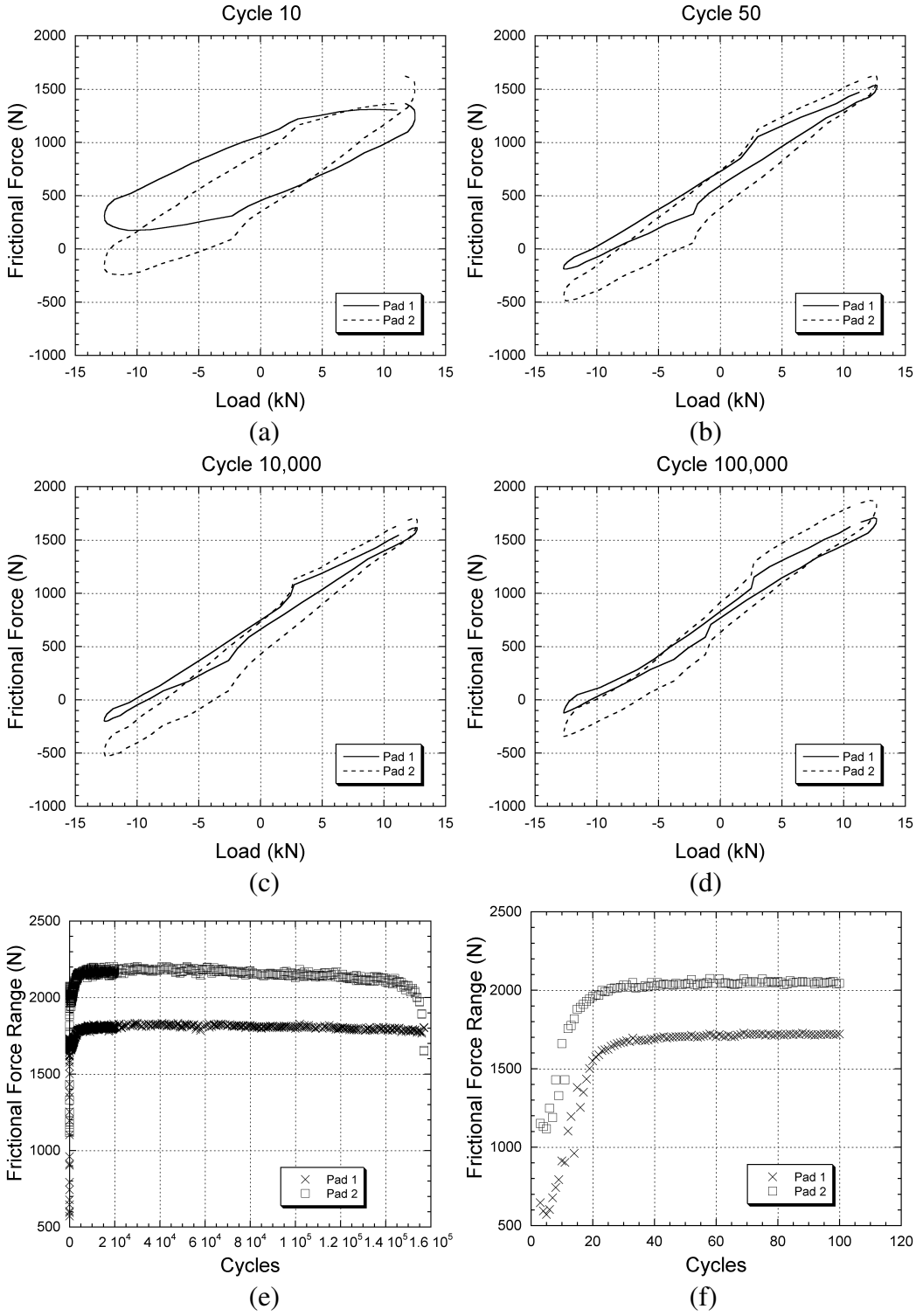


Figure A.11: Plots of frictional force vs. applied load for specimen 4C ($\sigma_a$ = 200 MPa, R = -1, f = 10 Hz, cylindrical pads) at (a) cycle 10, (b) cycle 50, (c) cycle 10,000, and (d) cycle 100,000. Plots of frictional force range vs. cycles for specimen 4C for (e) the entire test and (f) the initial cycles.

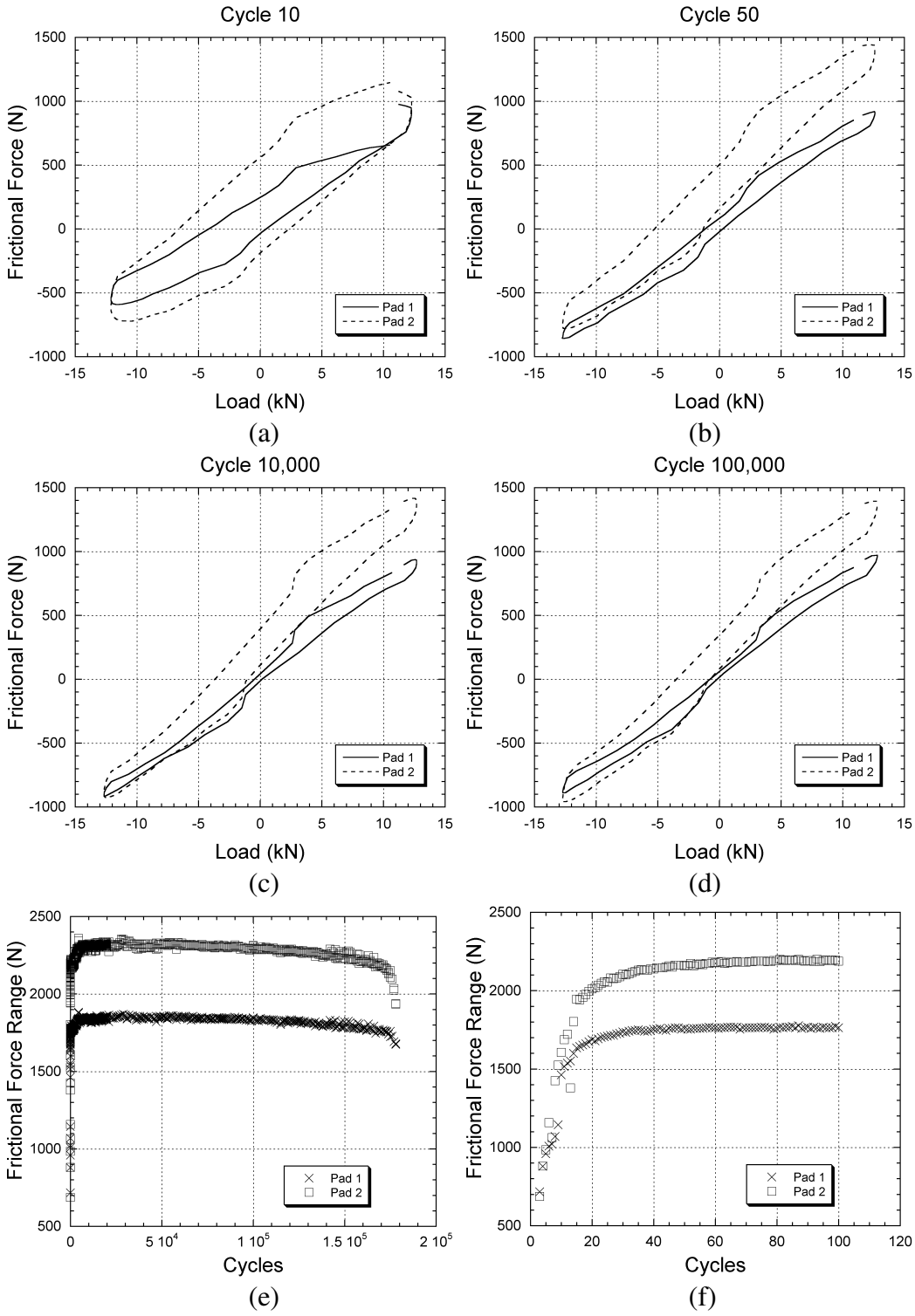


Figure A.12: Plots of frictional force vs. applied load for specimen 5A ($\sigma_a$ = 200 MPa, R = -1, f = 10 Hz, cylindrical pads) at (a) cycle 10, (b) cycle 50, (c) cycle 10,000, and (d) cycle 100,000. Plots of frictional force range vs. cycles for specimen 5A for (e) the entire test and (f) the initial cycles.

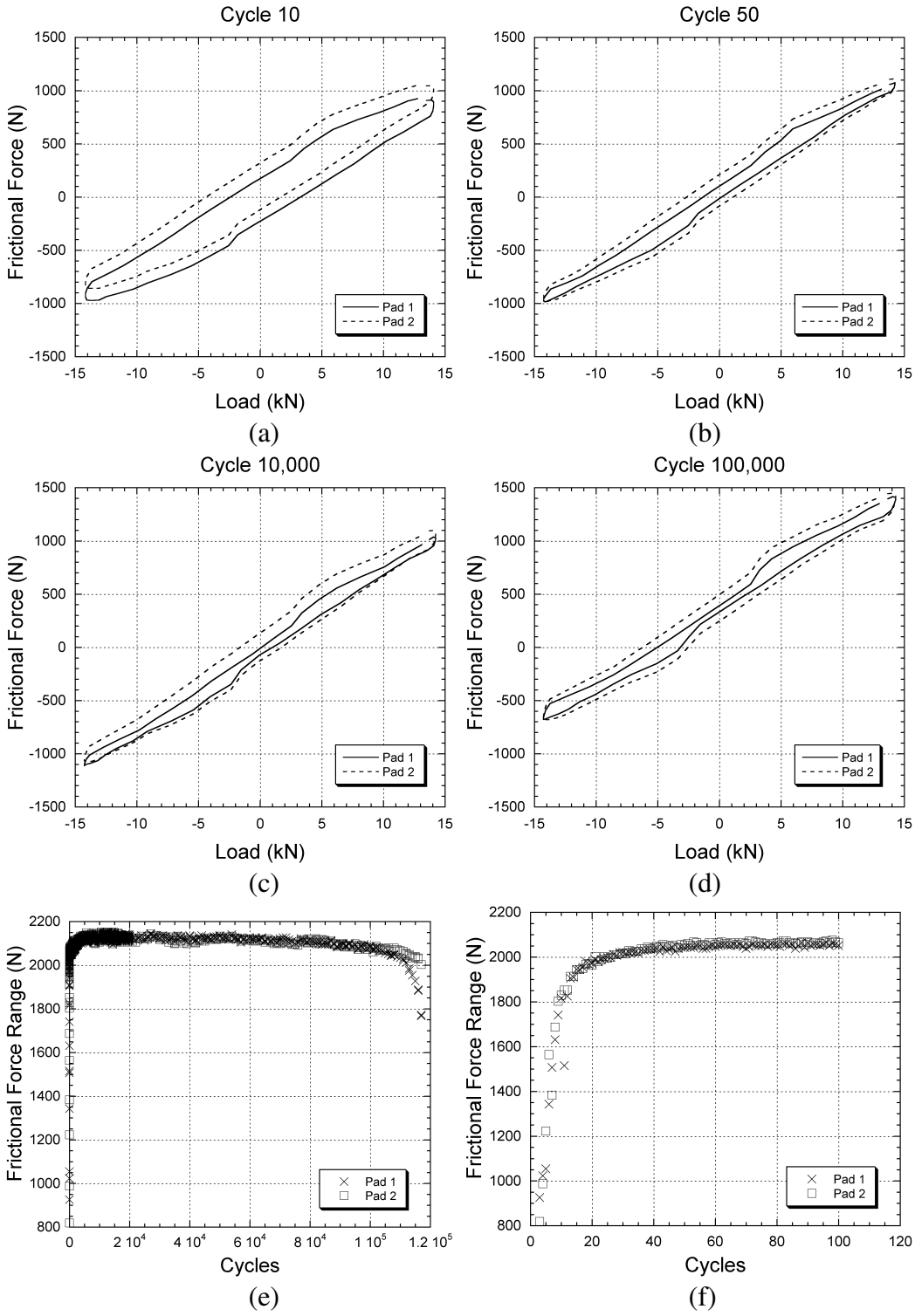


Figure A.13: Plots of frictional force vs. applied load for specimen 7C ($\sigma_a$ = 225 MPa, R = -1, f = 10 Hz, cylindrical pads) at (a) cycle 10, (b) cycle 50, (c) cycle 10,000, and (d) cycle 100,000. Plots of frictional force range vs. cycles for specimen 7C for (e) the entire test and (f) the initial cycles.

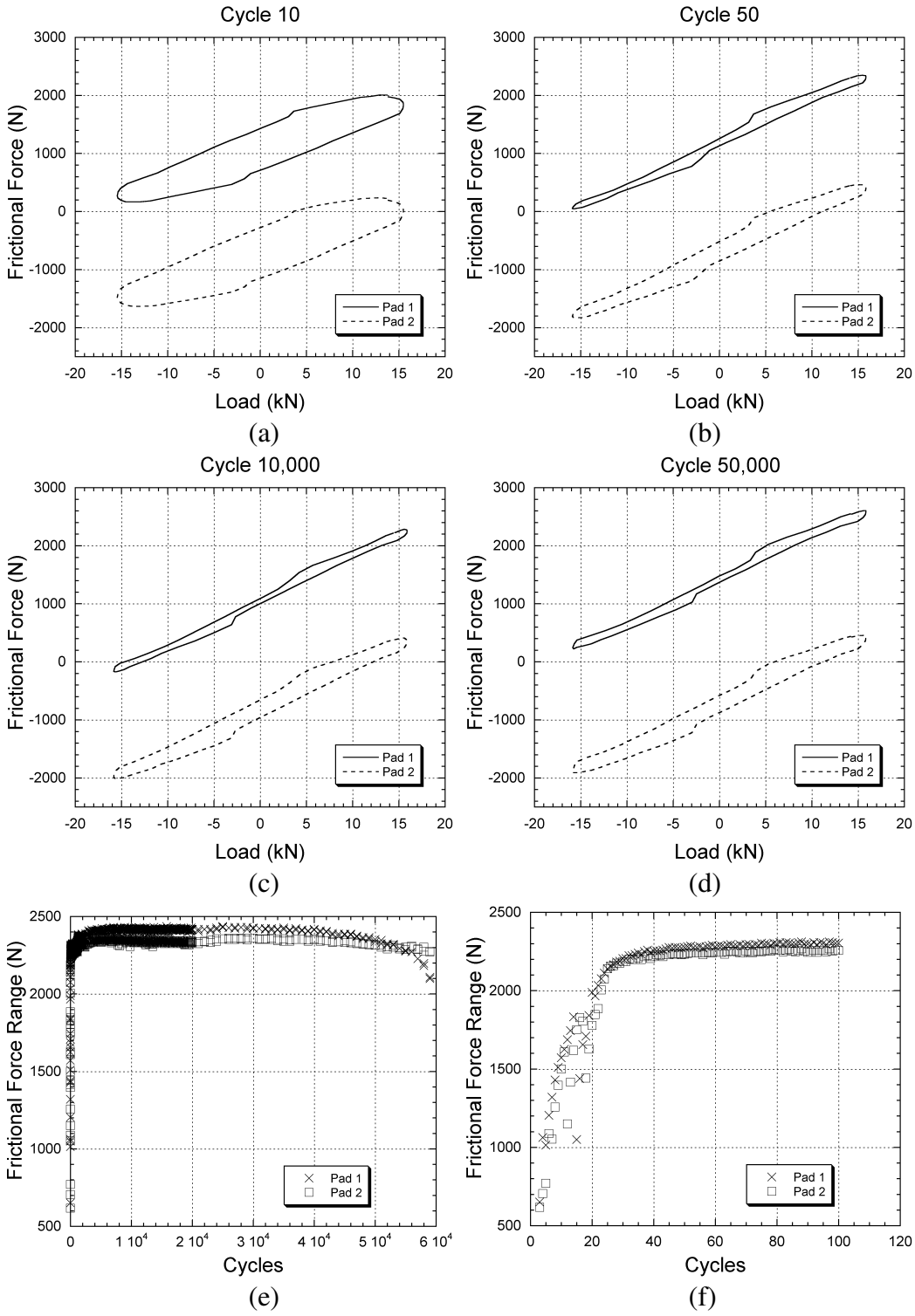


Figure A.14: Plots of frictional force vs. applied load for specimen 2B ($\sigma_a$ = 250 MPa, R = -1, f = 10 Hz, cylindrical pads) at (a) cycle 10, (b) cycle 50, (c) cycle 10,000, and (d) cycle 50,000. Plots of frictional force range vs. cycles for specimen 2B for (e) the entire test and (f) the initial cycles.

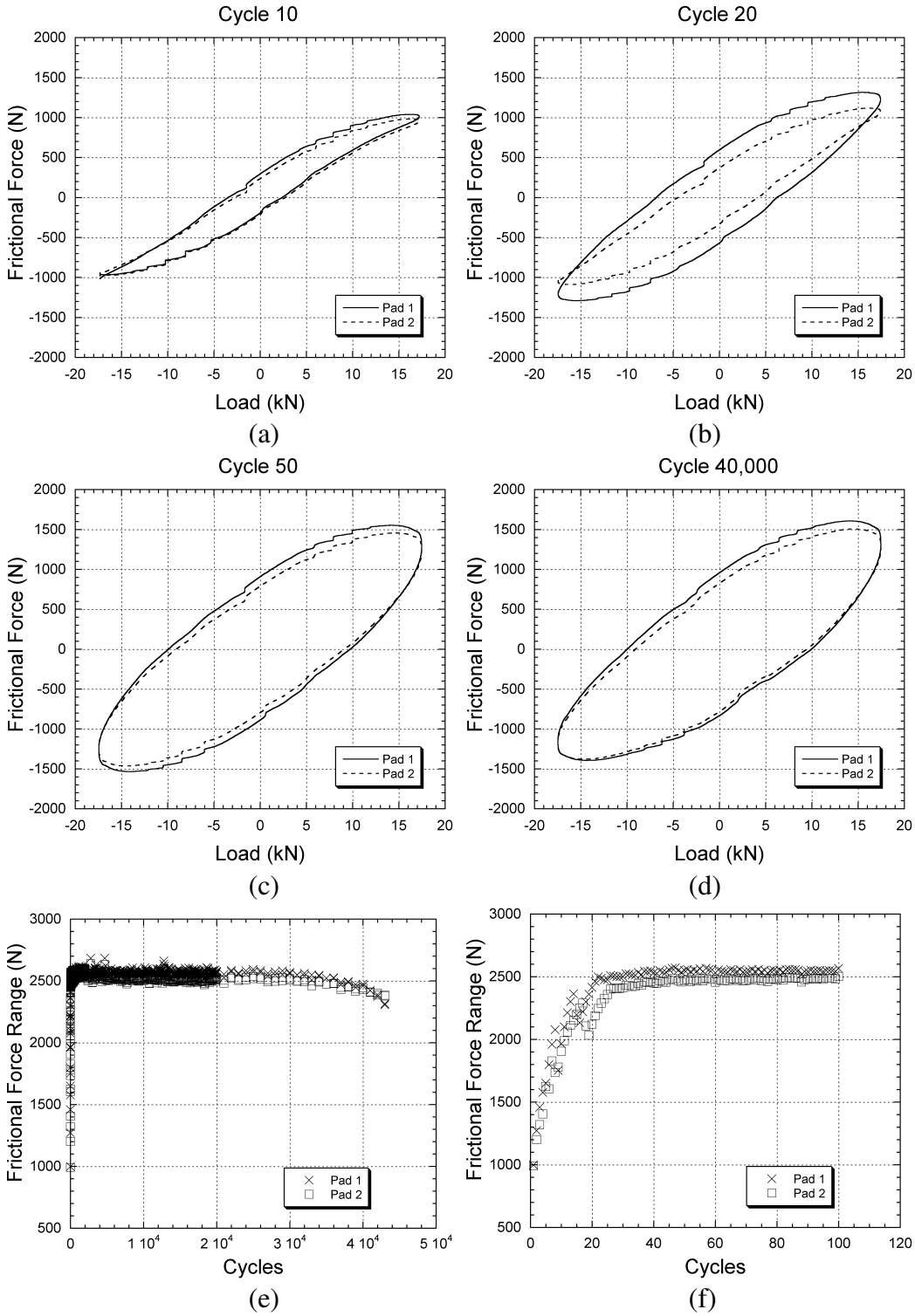


Figure A.15: Plots of frictional force vs. applied load for specimen 9C ($\sigma_a$ = 275 MPa, R = -1, f = 10 Hz, cylindrical pads) at (a) cycle 10, (b) cycle 20, (c) cycle 50, and (d) cycle 40,000. Plots of frictional force range vs. cycles for specimen 9C for (e) the entire test and (f) the initial cycles.

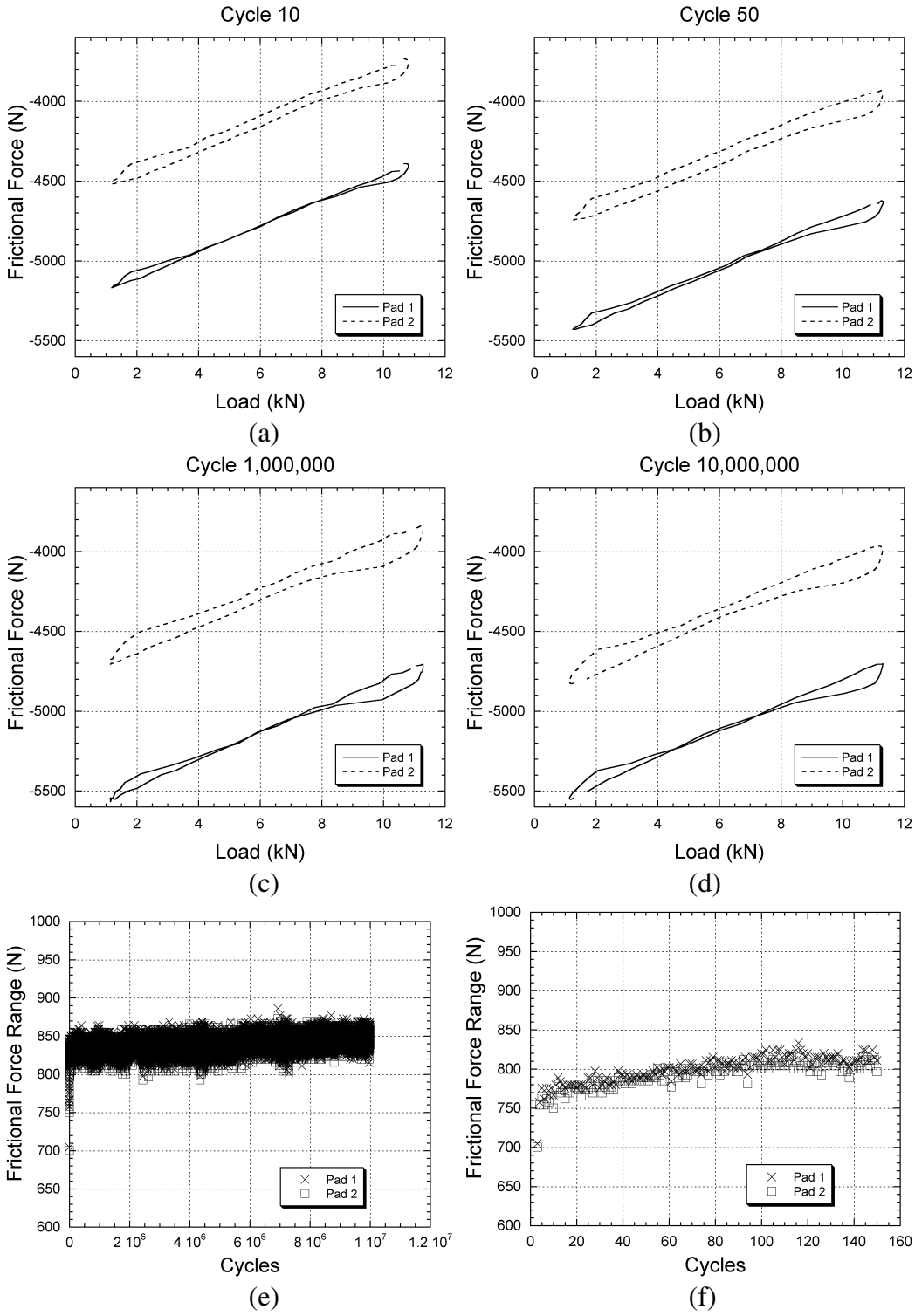


Figure A.16: Plots of frictional force vs. applied load for specimen 10C ($\sigma_a$ = 80 MPa, R = 0.1, f = 10 Hz, cylindrical pads) at (a) cycle 10, (b) cycle 50, (c) cycle 1,000,000, and (d) cycle 10,000,000. Plots of frictional force range vs. cycles for specimen 10C for (e) the entire test and (f) the initial cycles.

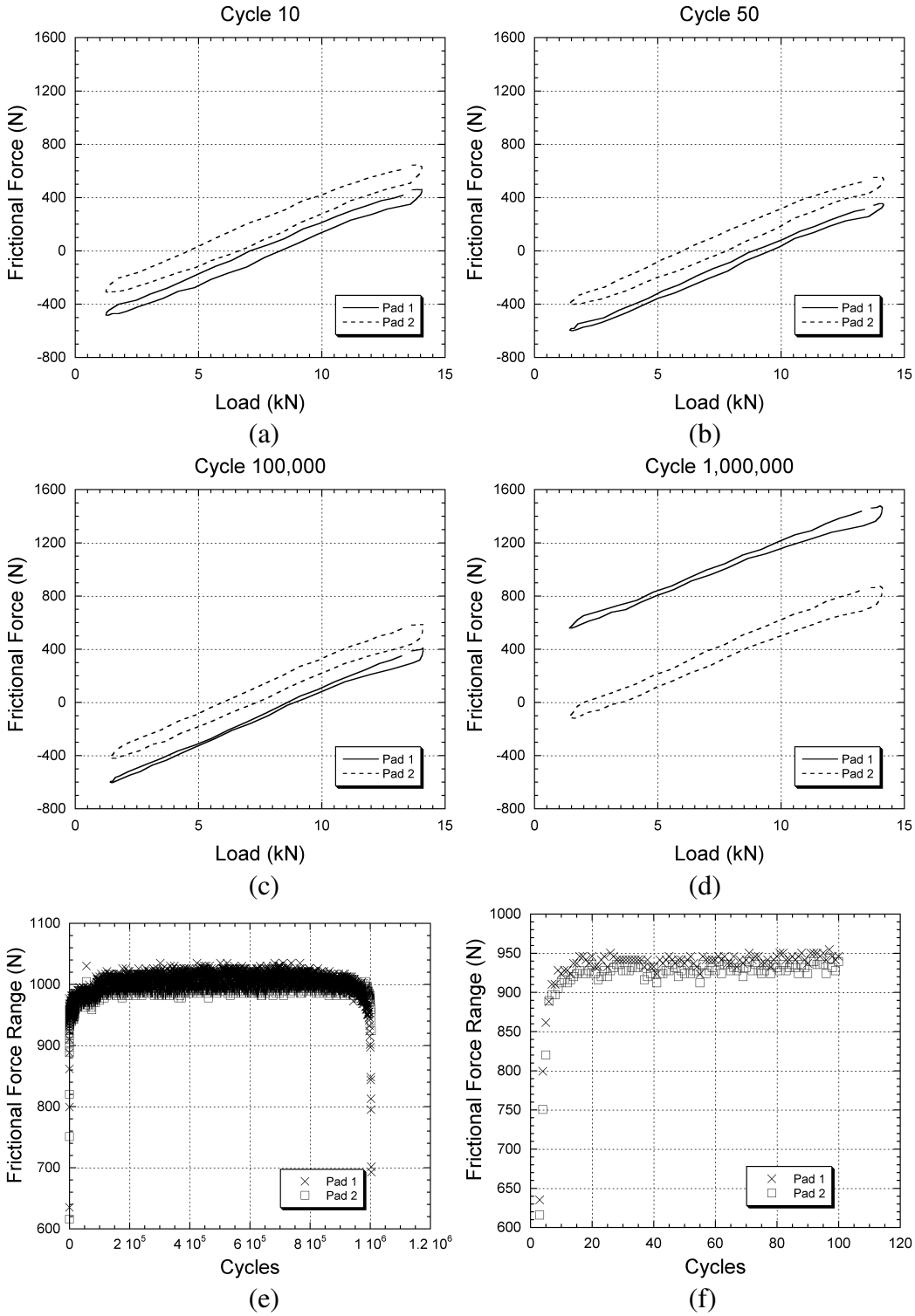


Figure A.17: Plots of frictional force vs. applied load for specimen 8B ($\sigma_a$ = 100 MPa, R = 0.1, f = 10 Hz, cylindrical pads) at (a) cycle 10, (b) cycle 50, (c) cycle 100,000, and (d) cycle 1,000,000. Plots of frictional force range vs. cycles for specimen 8B for (e) the entire test and (f) the initial cycles.

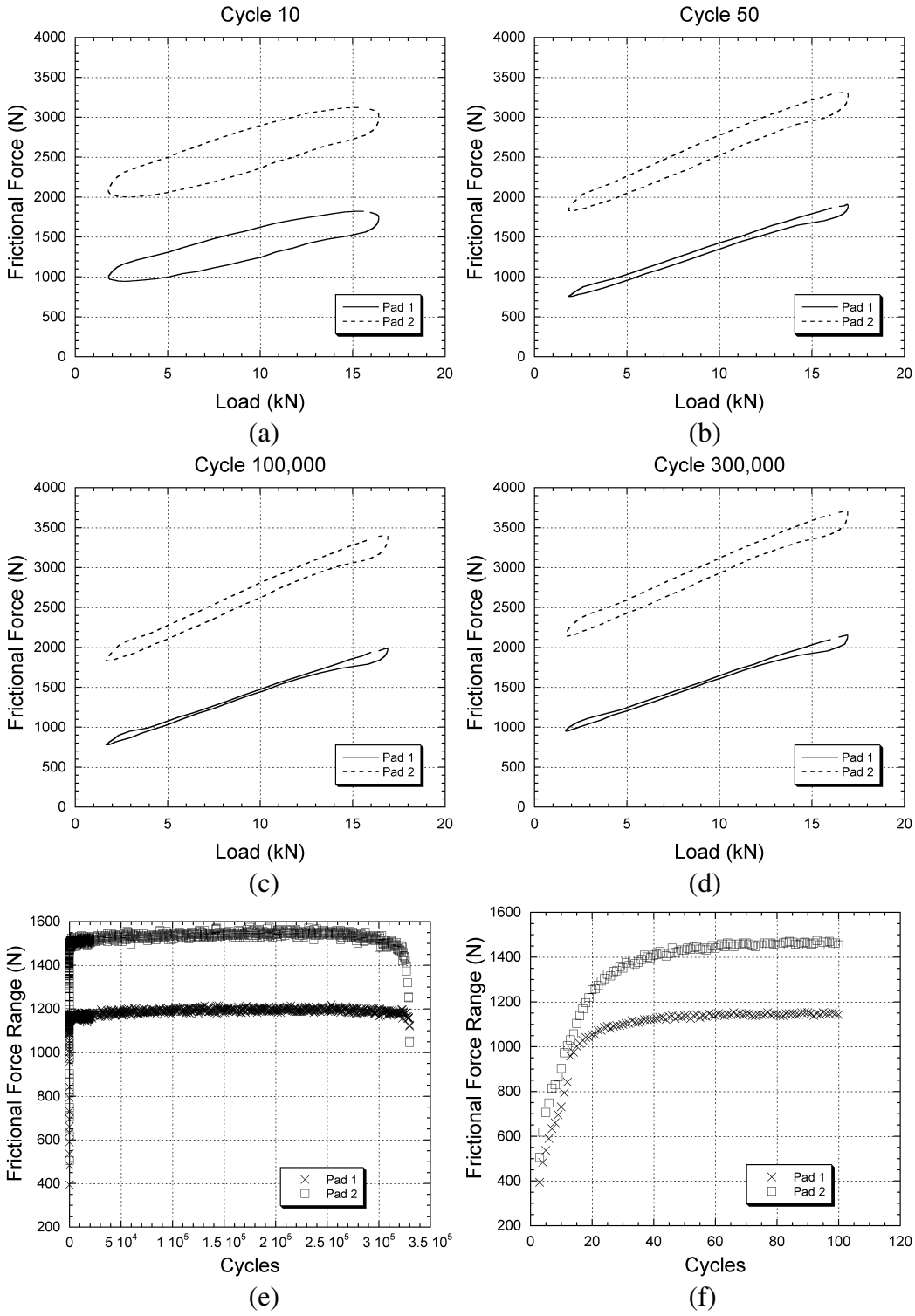


Figure A.18: Plots of frictional force vs. applied load for specimen 2A ($\sigma_a$ = 120 MPa, R = 0.1, f = 10 Hz, cylindrical pads) at (a) cycle 10, (b) cycle 50, (c) cycle 100,000, and (d) cycle 300,000. Plots of frictional force range vs. cycles for specimen 2A for (e) the entire test and (f) the initial cycles.

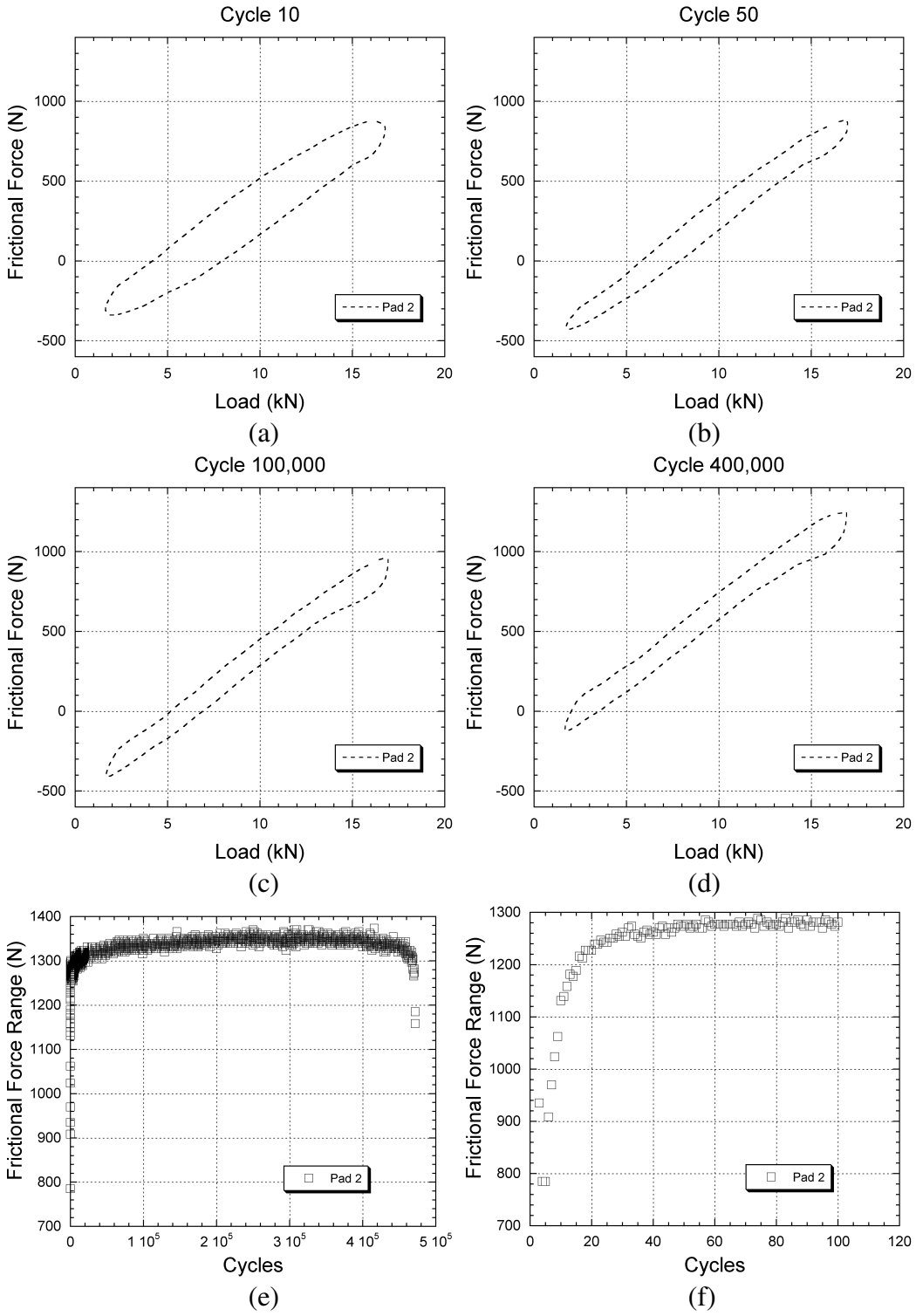


Figure A.19: Plots of frictional force vs. applied load for specimen 3B ($\sigma_a$ = 120 MPa, R = 0.1, f = 10 Hz, cylindrical pads) at (a) cycle 10, (b) cycle 50, (c) cycle 100,000, and (d) cycle 400,000. Plots of frictional force range vs. cycles for specimen 3B for (e) the entire test and (f) the initial cycles.

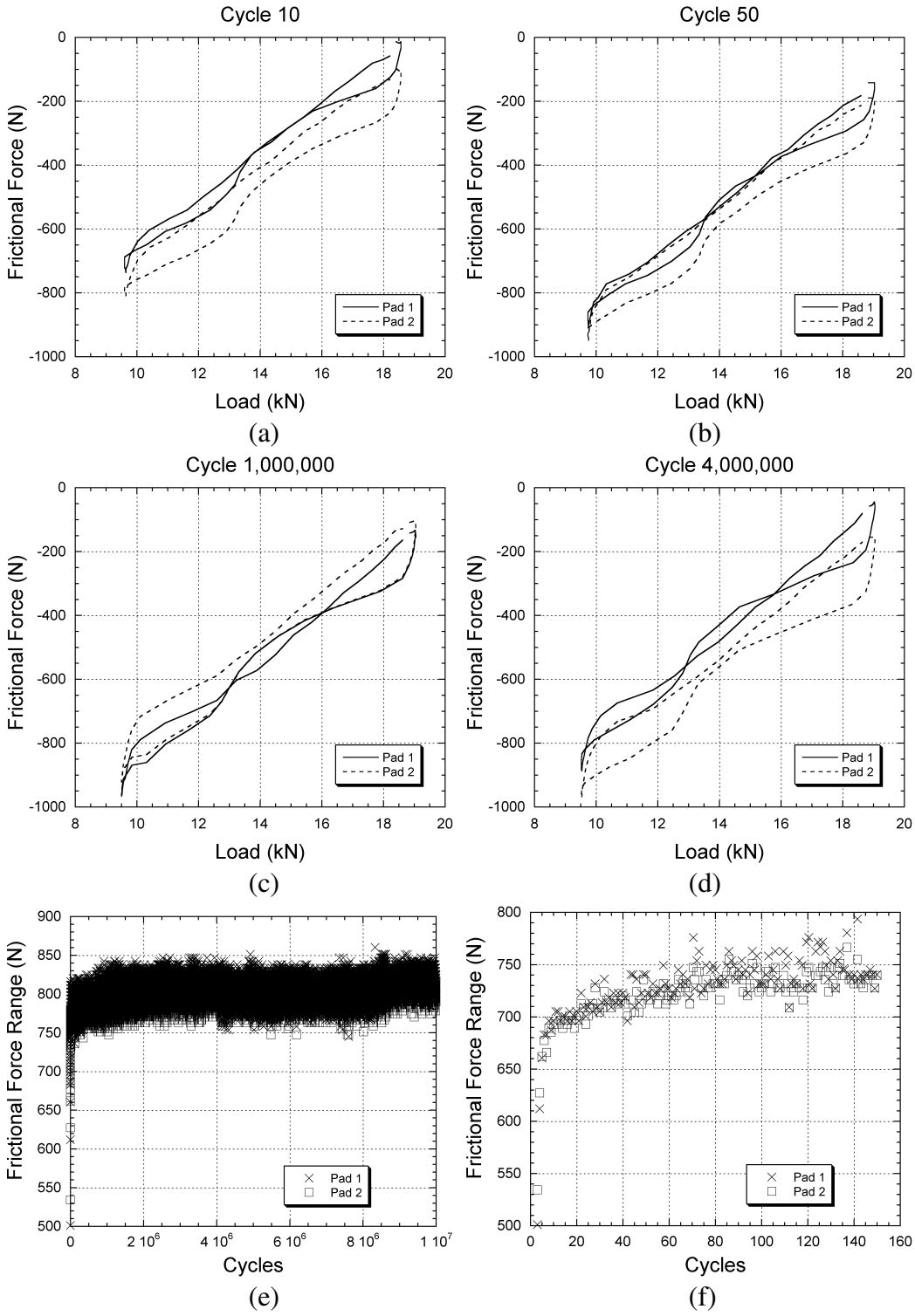


Figure A.20: Plots of frictional force vs. applied load for specimen 10A ($\sigma_a$ = 75 MPa, R = 0.5, f = 10 Hz, cylindrical pads) at (a) cycle 10, (b) cycle 50, (c) cycle 1,000,000, and (d) cycle 4,000,000. Plots of frictional force range vs. cycles for specimen 10A for (e) the entire test and (f) the initial cycles.

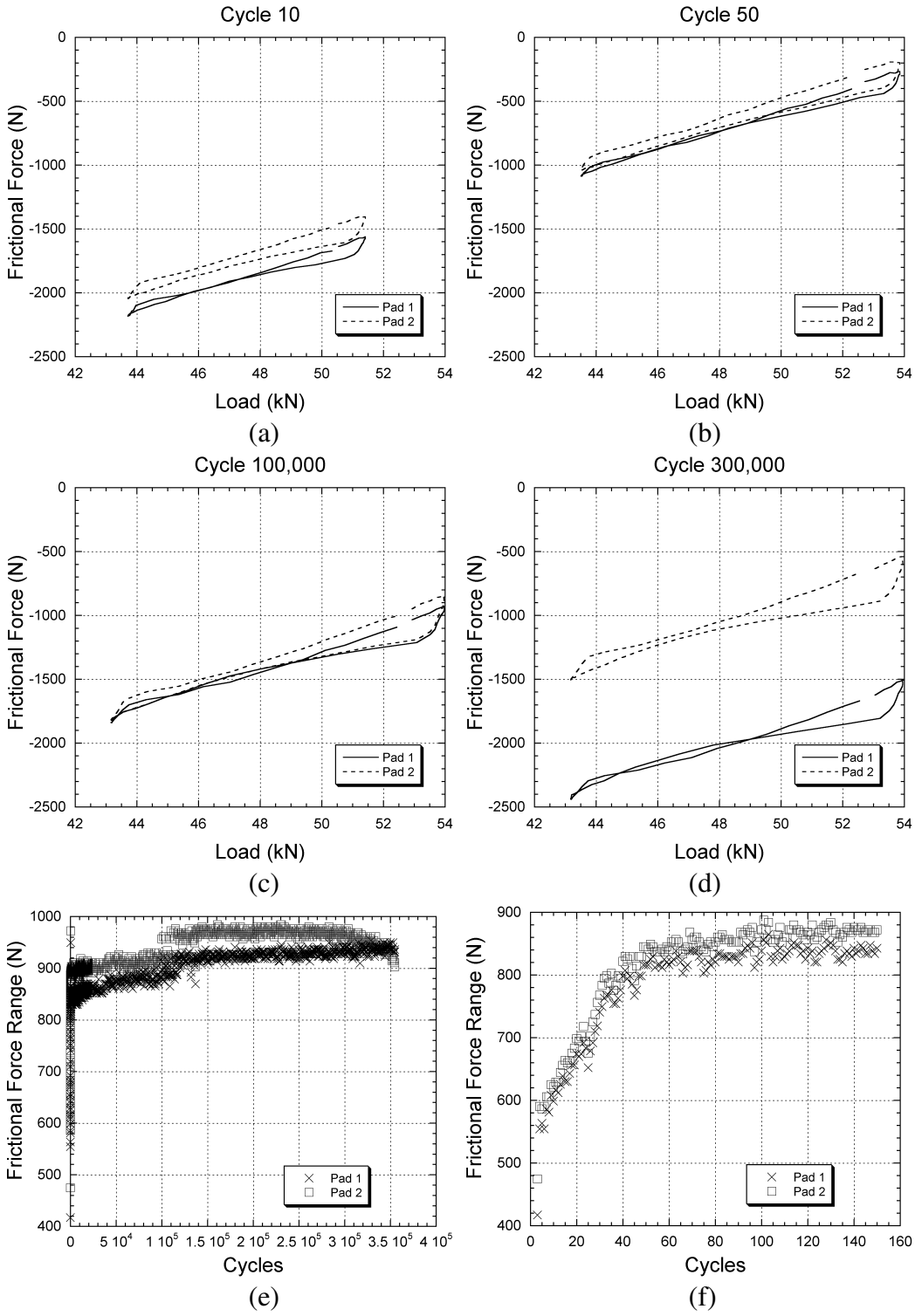


Figure A.21: Plots of frictional force vs. applied load for specimen 7A ($\sigma_a$ = 85 MPa, R = 0.8, f = 10 Hz, cylindrical pads) at (a) cycle 10, (b) cycle 50, (c) cycle 100,000, and (d) cycle 300,000. Plots of frictional force range vs. cycles for specimen 7A for (e) the entire test and (f) the initial cycles.

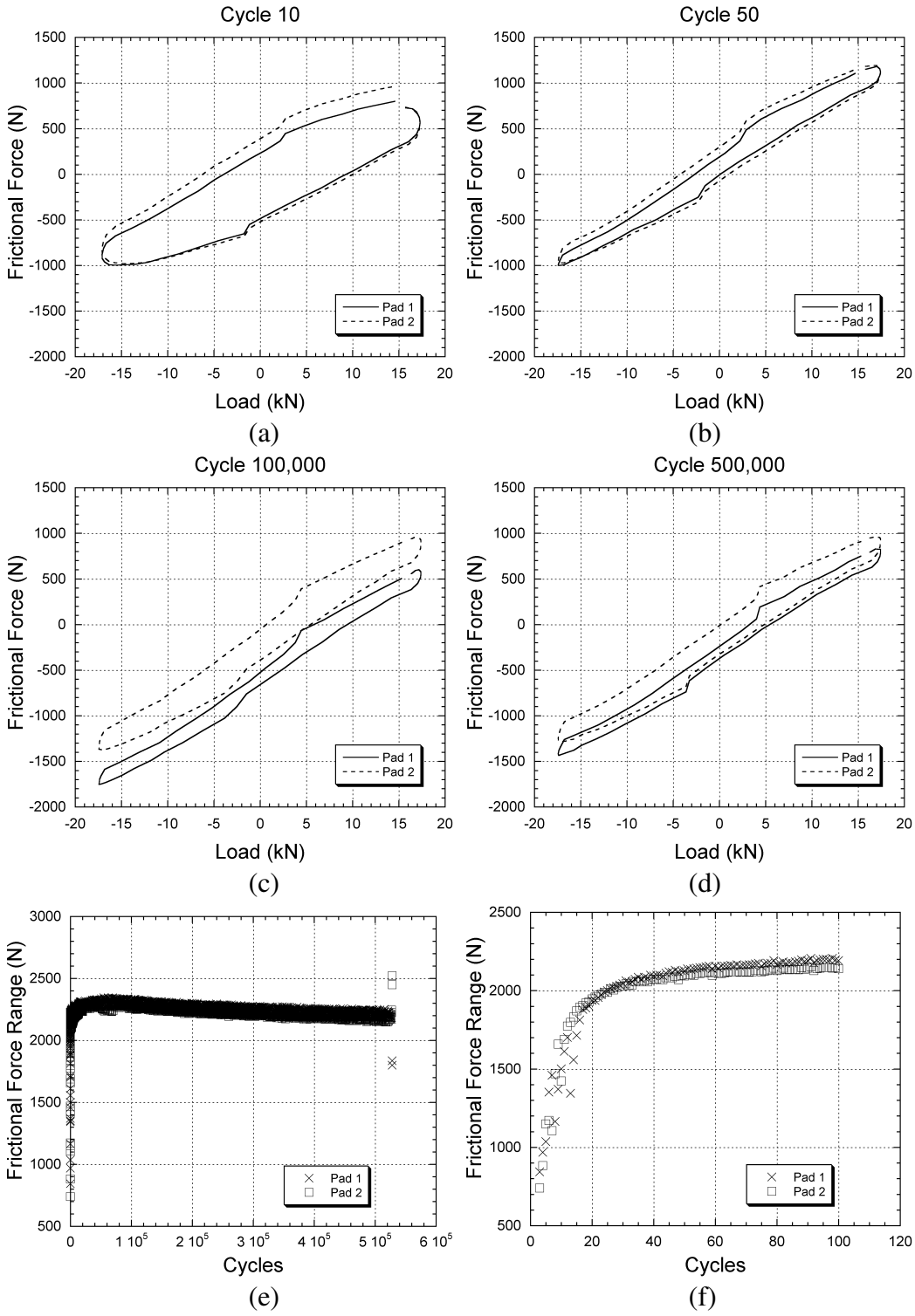


Figure A.22: Plots of frictional force vs. applied load for specimen 6C ($\sigma_a$ = 275 MPa, R = -1, f = 10 Hz, cylindrical pads, LPB) at (a) cycle 10, (b) cycle 50, (c) cycle 100,000, and (d) cycle 500,000. Plots of frictional force range vs. cycles for specimen 6C for (e) the entire test and (f) the initial cycles.

# APPENDIX B

## Tangential Force Calibration Data

Pad Dimensions

| | | |
|---|---|---|
| | *E (MPa)* | 118000 |
| Cylindrical | | |
| Pad 1 | $B_1$ *(mm)* | 8.95 |
| | $D_1$ *(mm)* | 5.97 |
| Pad 2 | $B_2$ *(mm)* | 9.00 |
| | $D_2$ *(mm)* | 5.96 |
| Flat | | |
| Pad 1 | $B_1$ *(mm)* | 9.00 |
| | $D_1$ *(mm)* | 5.95 |
| Pad 2 | $B_2$ *(mm)* | 9.02 |
| | $D_2$ *(mm)* | 5.96 |

$$F_t = \varepsilon^{pad}\frac{EBD}{C_B} \Rightarrow C_B = \frac{\varepsilon^{pad}EBD}{F_t}$$

Summary of Bending Correction Factors

| | Flat Pads | | |
|---|---|---|---|
| | Pad 1 | Pad 2 | Average |
| Trial 1 | 4.489 | 4.506 | 4.498 |
| Trial 2 | 4.375 | 4.535 | 4.455 |
| Trial 7 | 4.631 | 4.421 | 4.526 |
| Trial 8 | 4.546 | 4.392 | 4.469 |
| | | **Average:** | **4.49** |

| | Cylindrical Pads | | |
|---|---|---|---|
| | Pad 1 | Pad 2 | Average |
| Trial 3 | 4.819 | 5.322 | 5.071 |
| Trial 4 | 4.734 | 5.322 | 5.028 |
| Trial 5 | 4.791 | 5.350 | 5.071 |
| Trial 6 | 4.791 | 5.350 | 5.071 |
| | | **Average:** | **5.06** |

Table B.1: Flat pad tangential force calibration data.

| | | | Date: | 1/13/04 | | | | | Date: | 1/13/04 | | | | |
|---|---|---|---|---|---|---|---|---|---|---|---|---|---|---|
| | | | Normal Force: | -497 | | | | | Normal Force: | -497 | | | | |
| | | | Trial: | 1 | | | | | Trial: | 2 | | | | |
| | | | Pad Type: | Flat | | | | | Pad Type: | Flat | | | | |
| | | | Pad 1 | | | Pad 2 | | | Pad 1 | | | Pad 2 | | |
| Weight | Force Per Pad Foot | | Voltage | | | Voltage | | | Voltage | | | Voltage | | |
| lbs | lbs | Newtons | Absolute | Delta | Microstrain | Absolute | Delta | Microstrain | Absolute | Delta | Microstrain | Absolute | Delta | Microstrain |
| 0 | 0 | 0 | -0.004 | | | -0.001 | | | -0.005 | | | 0.000 | | |
| 10 | 5 | 22.24 | -0.021 | 0.017 | 17 | -0.016 | 0.015 | 15 | -0.022 | 0.017 | 17 | -0.015 | 0.015 | 15 |
| 20 | 10 | 44.48 | -0.036 | 0.032 | 32 | -0.031 | 0.030 | 30 | -0.038 | 0.033 | 33 | -0.031 | 0.031 | 31 |
| 30 | 15 | 66.72 | -0.052 | 0.048 | 48 | -0.047 | 0.046 | 46 | -0.053 | 0.048 | 48 | -0.047 | 0.047 | 47 |
| 40 | 20 | 88.96 | -0.068 | 0.064 | 64 | -0.063 | 0.062 | 62 | -0.068 | 0.063 | 63 | -0.062 | 0.062 | 62 |
| 50 | 25 | 111.20 | -0.084 | 0.080 | 80 | -0.079 | 0.078 | 78 | -0.084 | 0.079 | 79 | -0.079 | 0.079 | 79 |
| 0 | 0 | 0 | -0.005 | | | 0.000 | | | -0.005 | | | 0.000 | | |
| | | | Slope | 0.7104 | | Slope | 0.7104 | | Slope | 0.6924 | | Slope | 0.7149 | |
| | | | $C_B$ | 4.489 | | $C_B$ | 4.506 | | $C_B$ | 4.375 | | $C_B$ | 4.535 | |

| | | | Date: | 1/20/04 | | | | | Date: | 1/20/04 | | | | |
|---|---|---|---|---|---|---|---|---|---|---|---|---|---|---|
| | | | Normal Force: | -499 | | | | | Normal Force: | -499 | | | | |
| | | | Trial: | 7 | | | | | Trial: | 8 | | | | |
| | | | Pad Type: | Flat | | | | | Pad Type: | Flat | | | | |
| | | | Pad 1 | | | Pad 2 | | | Pad 1 | | | Pad 2 | | |
| Weight | Force Per Pad Foot | | Voltage | | | Voltage | | | Voltage | | | Voltage | | |
| lbs | lbs | Newtons | Absolute | Delta | Microstrain | Absolute | Delta | Microstrain | Absolute | Delta | Microstrain | Absolute | Delta | Microstrain |
| 0 | 0 | 0 | -0.017 | | | 0.128 | | | -0.017 | | | 0.128 | | |
| 10 | 5 | 22.24 | -0.035 | 0.018 | 18 | 0.114 | 0.014 | 14 | -0.035 | 0.018 | 18 | 0.115 | 0.013 | 13 |
| 20 | 10 | 44.48 | -0.051 | 0.034 | 34 | 0.099 | 0.029 | 29 | -0.051 | 0.034 | 34 | 0.099 | 0.029 | 29 |
| 30 | 15 | 66.72 | -0.068 | 0.051 | 51 | 0.084 | 0.044 | 44 | -0.067 | 0.050 | 50 | 0.084 | 0.044 | 44 |
| 40 | 20 | 88.96 | -0.084 | 0.067 | 67 | 0.068 | 0.060 | 60 | -0.083 | 0.066 | 66 | 0.069 | 0.059 | 59 |
| 50 | 25 | 111.20 | -0.100 | 0.083 | 83 | 0.052 | 0.076 | 76 | -0.099 | 0.082 | 82 | 0.053 | 0.075 | 75 |
| 0 | 0 | 0 | -0.017 | | | 0.127 | | | -0.016 | | | 0.128 | | |
| | | | Slope | 0.7329 | | Slope | 0.6969 | | Slope | 0.7194 | | Slope | 0.6924 | |
| | | | $C_B$ | 4.631 | | $C_B$ | 4.421 | | $C_B$ | 4.546 | | $C_B$ | 4.392 | |

Table B.2: Cylindrical pad tangential force calibration data.

| | | | Date: | 1/14/04 | | | | | Date: | 1/14/04 | | | | |
|---|---|---|---|---|---|---|---|---|---|---|---|---|---|---|
| | | | Normal Force: | -499 | | | | | Normal Force: | -499 | | | | |
| | | | Trial: | 3 | | | | | Trial: | 4 | | | | |
| | | | Pad Type: | Cylindrical | | | | | Pad Type: | Cylindrical | | | | |
| | | | Pad 1 | | | Pad 2 | | | Pad 1 | | | Pad 2 | | |
| Weight | Force Per Pad Foot | | Voltage | | | Voltage | | | Voltage | | | Voltage | | |
| lbs | lbs | Newtons | Absolute | Delta | Microstrain | Absolute | Delta | Microstrain | Absolute | Delta | Microstrain | Absolute | Delta | Microstrain |
| 0 | 0 | 0 | 0.164 | | | -0.091 | | | 0.165 | | | -0.089 | | |
| 10 | 5 | 22.24 | 0.146 | 0.018 | 18 | -0.108 | 0.017 | 17 | 0.146 | 0.019 | 19 | -0.106 | 0.017 | 17 |
| 20 | 10 | 44.48 | 0.129 | 0.035 | 35 | -0.126 | 0.035 | 35 | 0.129 | 0.036 | 36 | -0.125 | 0.036 | 36 |
| 30 | 15 | 66.72 | 0.112 | 0.052 | 52 | -0.145 | 0.054 | 54 | 0.112 | 0.053 | 53 | -0.143 | 0.054 | 54 |
| 40 | 20 | 88.96 | 0.095 | 0.069 | 69 | -0.163 | 0.072 | 72 | 0.096 | 0.069 | 69 | -0.162 | 0.073 | 73 |
| 50 | 25 | 111.20 | 0.078 | 0.086 | 86 | -0.183 | 0.092 | 92 | 0.079 | 0.086 | 86 | -0.181 | 0.092 | 92 |
| 0 | 0 | 0 | 0.165 | | | -0.090 | | | 0.165 | | | -0.089 | | |
| | | | Slope | 0.7644 | | Slope | 0.8408 | | Slope | 0.7509 | | Slope | 0.8408 | |
| | | | $C_B$ | 4.819 | | $C_B$ | 5.322 | | $C_B$ | 4.734 | | $C_B$ | 5.322 | |

| | | | Date: | 1/14/04 | | | | | Date: | 1/14/04 | | | | |
|---|---|---|---|---|---|---|---|---|---|---|---|---|---|---|
| | | | Normal Force: | -499 | | | | | Normal Force: | -499 | | | | |
| | | | Trial: | 5 | | | | | Trial: | 6 | | | | |
| | | | Pad Type: | Cylindrical | | | | | Pad Type: | Cylindrical | | | | |
| | | | Pad 1 | | | Pad 2 | | | Pad 1 | | | Pad 2 | | |
| Weight | Force Per Pad Foot | | Voltage | | | Voltage | | | Voltage | | | Voltage | | |
| lbs | lbs | Newtons | Absolute | Delta | Microstrain | Absolute | Delta | Microstrain | Absolute | Delta | Microstrain | Absolute | Delta | Microstrain |
| 0 | 0 | 0 | 0.166 | | | -0.088 | | | 0.166 | | | -0.088 | | |
| 10 | 5 | 22.24 | 0.147 | 0.017 | 17 | -0.105 | 0.014 | 14 | 0.148 | 0.017 | 17 | -0.105 | 0.016 | 16 |
| 20 | 10 | 44.48 | 0.130 | 0.034 | 34 | -0.123 | 0.032 | 32 | 0.130 | 0.035 | 35 | -0.123 | 0.034 | 34 |
| 30 | 15 | 66.72 | 0.114 | 0.050 | 50 | -0.142 | 0.051 | 51 | 0.113 | 0.052 | 52 | -0.142 | 0.053 | 53 |
| 40 | 20 | 88.96 | 0.097 | 0.067 | 67 | -0.161 | 0.070 | 70 | 0.097 | 0.068 | 68 | -0.161 | 0.072 | 72 |
| 50 | 25 | 111.20 | 0.079 | 0.085 | 85 | -0.180 | 0.089 | 89 | 0.080 | 0.085 | 85 | -0.180 | 0.091 | 91 |
| 0 | 0 | 0 | 0.166 | | | -0.088 | | | 0.167 | | | -0.087 | | |
| | | | Slope | 0.7599 | | Slope | 0.8453 | | Slope | 0.7599 | | Slope | 0.8453 | |
| | | | $C_B$ | 4.791 | | $C_B$ | 5.350 | | $C_B$ | 4.791 | | $C_B$ | 5.350 | |

Note: The term "Slope" used in the tables represents the slope of the line calculated from a linear regression fit for Microstrain vs. Force.

# APPENDIX C

Frequency Correction Factor Data

Table C.1: Flat pad frequency correction factor data.

Summary of 0.2Hz/10Hz factors for Range:

| | Pad 1 | Pad 2 |
|---|---|---|
| Flat | 10.5 | 9.2 |

| | $\sigma_a$ =100 MPa | | | Flat Pads | | | | | |
|---|---|---|---|---|---|---|---|---|---|
| | Pad 1 | Pad 2 | Average | Pad 1 | Pad 2 | Average | Pad 1 | Pad 2 | Average |
| | Min | Min | Min | Max | Max | Max | Range | Range | Range |
| 0.05Hz | -390.4 | -393.1 | -391.8 | 420.3 | 422.0 | 421.1 | 810.7 | 815.1 | 812.9 |
| 0.2Hz | -389.1 | -391.1 | -390.1 | 408.2 | 411.6 | 409.9 | 797.3 | 802.7 | 800.0 |
| 1 Hz | -301.1 | -313.5 | -307.3 | 278.3 | 296.1 | 287.2 | 579.4 | 609.6 | 594.5 |
| 5 Hz | -86.6 | -79.6 | -83.1 | 25.2 | 23.5 | 24.3 | 111.8 | 103.1 | 107.4 |
| 10 Hz | -68.5 | -70.8 | -69.7 | 5.0 | 14.8 | 9.9 | 73.5 | 85.6 | 79.6 |
| 10 Hz B | -27.9 | -39.3 | -33.6 | 46.0 | 48.0 | 47.0 | 73.9 | 87.3 | 80.6 |
| 10 Hz 9 | -23.2 | -17.1 | -20.1 | 48.3 | 65.1 | 56.7 | 71.5 | 82.2 | 76.9 |
| 0.2Hz/1Hz | 1.3 | 1.2 | 1.3 | 1.5 | 1.4 | 1.4 | 1.4 | 1.3 | 1.3 |
| 1Hz/10Hz | 4.4 | 4.4 | 4.4 | 55.3 | 20.0 | 29.0 | 7.9 | 7.1 | 7.5 |
| 0.2Hz/10Hz | 5.7 | 5.5 | 5.6 | 81.1 | 27.9 | 41.4 | 10.8 | 9.4 | 10.1 |
| 0.05Hz/10Hz | 5.7 | 5.5 | 5.6 | 83.5 | 28.6 | 42.5 | 11.0 | 9.5 | 10.3 |

| | $\sigma_a$ =150 MPa | | | Flat Pads | | | | | |
|---|---|---|---|---|---|---|---|---|---|
| | Pad 1 | Pad 2 | Average | Pad 1 | Pad 2 | Average | Pad 1 | Pad 2 | Average |
| | Min | Min | Min | Max | Max | Max | Range | Range | Range |
| 0.05Hz | -553.9 | -567.7 | -560.8 | 631.1 | 634.8 | 633.0 | 1185.0 | 1202.5 | 1193.8 |
| 0.2Hz | -571.4 | -570.7 | -571.0 | 595.5 | 605.9 | 600.7 | 1166.9 | 1176.6 | 1171.8 |
| 1 Hz | -421.6 | -431.4 | -426.5 | 414.9 | 447.8 | 431.4 | 836.6 | 879.2 | 857.9 |
| 5 Hz | -81.9 | -62.4 | -72.2 | 82.9 | 87.3 | 85.1 | 164.8 | 149.7 | 157.3 |
| 10 Hz | -61.4 | -59.1 | -60.3 | 51.0 | 71.5 | 61.3 | 112.5 | 130.6 | 121.5 |
| 10 Hz B | -44.6 | -60.4 | -52.5 | 66.1 | 68.8 | 67.5 | 110.8 | 129.2 | 120.0 |
| 10 Hz 9 | -28.9 | -1.7 | -15.3 | 82.2 | 124.9 | 103.6 | 111.1 | 126.6 | 118.8 |
| 0.2Hz/1Hz | 1.4 | 1.3 | 1.3 | 1.4 | 1.4 | 1.4 | 1.4 | 1.3 | 1.4 |
| 1Hz/10Hz | 6.9 | 7.3 | 7.1 | 8.1 | 6.3 | 7.0 | 7.4 | 6.7 | 7.1 |
| 0.2Hz/10Hz | 9.3 | 9.7 | 9.5 | 11.7 | 8.5 | 9.8 | 10.4 | 9.0 | 9.7 |
| 0.05Hz/10Hz | 9.0 | 9.6 | 9.3 | 12.4 | 8.9 | 10.3 | 10.5 | 9.2 | 9.9 |

| | $\sigma_a$ =200 MPa | | | Flat Pads | | | | | |
|---|---|---|---|---|---|---|---|---|---|
| | Pad 1 | Pad 2 | Average | Pad 1 | Pad 2 | Average | Pad 1 | Pad 2 | Average |
| | Min | Min | Min | Max | Max | Max | Range | Range | Range |
| 0.2Hz | -747.9 | -742.9 | -745.4 | 797.6 | 815.8 | 806.7 | 1545.6 | 1558.7 | 1552.1 |
| 1 Hz | -545.5 | -580.1 | -562.8 | 565.0 | 585.1 | 575.1 | 1110.5 | 1165.2 | 1137.9 |
| 5 Hz | -108.1 | -105.4 | -106.8 | 110.1 | 93.3 | 101.7 | 218.2 | 198.7 | 208.5 |
| 10 Hz | -79.2 | -97.7 | -88.5 | 67.5 | 72.2 | 69.8 | 146.7 | 169.9 | 158.3 |
| 0.2Hz/1Hz | 1.4 | 1.3 | 1.3 | 1.4 | 1.4 | 1.4 | 1.4 | 1.3 | 1.4 |
| 1Hz/10Hz | 6.9 | 5.9 | 6.4 | 8.4 | 8.1 | 8.2 | 7.6 | 6.9 | 7.2 |
| 0.2Hz/10Hz | 9.4 | 7.6 | 8.4 | 11.8 | 11.3 | 11.6 | 10.5 | 9.2 | 9.9 |

| | $\sigma_a$ =250 MPa | | | Flat Pads | | | | | |
|---|---|---|---|---|---|---|---|---|---|
| | Pad 1 | Pad 2 | Average | Pad 1 | Pad 2 | Average | Pad 1 | Pad 2 | Average |
| | Min | Min | Min | Max | Max | Max | Range | Range | Range |
| 0.2Hz | -901.0 | -925.2 | -913.1 | 974.9 | 976.2 | 975.6 | 1875.9 | 1901.4 | 1888.7 |
| 1 Hz | -648.9 | -687.5 | -668.2 | 696.6 | 722.1 | 709.3 | 1345.5 | 1409.6 | 1377.6 |
| 5 Hz | -135.6 | -133.9 | -134.8 | 121.2 | 99.0 | 110.1 | 256.8 | 233.0 | 244.9 |
| 10 Hz | -93.7 | -117.2 | -105.4 | 86.6 | 91.6 | 89.1 | 180.3 | 208.8 | 194.5 |
| 0.2Hz/1Hz | 1.4 | 1.3 | 1.4 | 1.4 | 1.4 | 1.4 | 1.4 | 1.3 | 1.4 |
| 1Hz/10Hz | 6.9 | 5.9 | 6.3 | 8.0 | 7.9 | 8.0 | 7.5 | 6.8 | 7.1 |
| 0.2Hz/10Hz | 9.6 | 7.9 | 8.7 | 11.3 | 10.7 | 10.9 | 10.4 | 9.1 | 9.8 |

Table C.2: Cylindrical pad frequency correction factor data.

| | $\sigma_a$ =100 MPa | | | Cylindrical Pads | | | | | |
|---|---|---|---|---|---|---|---|---|---|
| | Pad 1 | Pad 2 | Average | Pad 1 | Pad 2 | Average | Pad 1 | Pad 2 | Average |
| | Min | Min | Min | Max | Max | Max | Range | Range | Range |
| 1 Hz | -269.2 | -259.8 | -264.5 | 254.8 | 280.6 | 267.7 | 524.0 | 540.5 | 532.3 |
| 5 Hz | -55.7 | -31.2 | -43.5 | 48.7 | 60.8 | 54.7 | 104.4 | 92.0 | 98.2 |
| 10 Hz | -48.3 | -33.6 | -41.0 | 22.5 | 46.3 | 34.4 | 70.8 | 79.9 | 75.4 |
| 1Hz/10Hz | 5.6 | 7.7 | 6.5 | 11.3 | 6.1 | 7.8 | 7.4 | 6.8 | 7.1 |

| | $\sigma_a$ =150 MPa | | | Cylindrical Pads | | | | | |
|---|---|---|---|---|---|---|---|---|---|
| | Pad 1 | Pad 2 | Average | Pad 1 | Pad 2 | Average | Pad 1 | Pad 2 | Average |
| | Min | Min | Min | Max | Max | Max | Range | Range | Range |
| 1 Hz | -412.9 | -406.5 | -409.7 | 420.0 | 447.8 | 433.9 | 832.9 | 854.4 | 843.6 |
| 5 Hz | -87.3 | -61.8 | -74.5 | 89.0 | 98.4 | 93.7 | 176.2 | 160.1 | 168.2 |
| 10 Hz | -55.7 | -45.7 | -50.7 | 51.7 | 76.9 | 64.3 | 107.4 | 122.5 | 115.0 |
| 1Hz/10Hz | 7.4 | 8.9 | 8.1 | 8.1 | 5.8 | 6.7 | 7.8 | 7.0 | 7.4 |

| | $\sigma_a$ =200 MPa | | | Cylindrical Pads | | | | | |
|---|---|---|---|---|---|---|---|---|---|
| | Pad 1 | Pad 2 | Average | Pad 1 | Pad 2 | Average | Pad 1 | Pad 2 | Average |
| | Min | Min | Min | Max | Max | Max | Range | Range | Range |
| 1 Hz | -539.5 | -544.2 | -541.8 | 570.4 | 593.2 | 581.8 | 1109.8 | 1137.4 | 1123.6 |
| 5 Hz | -108.1 | -88.0 | -98.0 | 123.2 | 119.8 | 121.5 | 231.3 | 207.8 | 219.6 |
| 10 Hz | -72.8 | -72.8 | -72.8 | 70.5 | 90.3 | 80.4 | 143.3 | 163.2 | 153.2 |
| 1Hz/10Hz | 7.4 | 7.5 | 7.4 | 8.1 | 6.6 | 7.2 | 7.7 | 7.0 | 7.4 |

| | $\sigma_a$ =250 MPa | | | Cylindrical Pads | | | | | |
|---|---|---|---|---|---|---|---|---|---|
| | Pad 1 | Pad 2 | Average | Pad 1 | Pad 2 | Average | Pad 1 | Pad 2 | Average |
| | Min | Min | Min | Max | Max | Max | Range | Range | Range |
| 1 Hz | -651.9 | -676.1 | -664.0 | 737.9 | 746.6 | 742.2 | 1389.8 | 1422.7 | 1406.3 |
| 5 Hz | -102.7 | -95.7 | -99.2 | 176.6 | 154.8 | 165.7 | 279.3 | 250.4 | 264.9 |
| 10 Hz | -79.2 | -96.0 | -87.6 | 99.7 | 106.1 | 102.9 | 178.9 | 202.1 | 190.5 |
| 1Hz/10Hz | 8.2 | 7.0 | 7.6 | 7.4 | 7.0 | 7.2 | 7.8 | 7.0 | 7.4 |

# APPENDIX D

Georgia Institute of Technology Fretting Fatigue Data

Table D.1: Fretting fatigue data from prior work performed at Georgia Institute of Technolgy (Wallace, 2001; Swalla, 2002).

| Specimen | R | $\sigma_a$ MPa (ksi) | $p_{flat}$ MPa (ksi) | $p_{cyl}$ MPa (ksi) | $\delta_n$ μm (mils) | $\delta_{t,cyl.}$ μm (mils) | $\delta_{t,flat}$ μm (mils) | $N_i$ (Cycles) | $N_T$ (Cycles) |
|---|---|---|---|---|---|---|---|---|---|
| 113-S411 | 0.8 | 60 (8.7) | 69 (10) | 345 (50) | 7.1 (0.3) | 4.5 (0.2) | 4.3 (0.2) | 1,000,000 | 1,004,000 |
| 113-S322 | 0.5 | 105 (15.2) | 69 (10) | 345 (50) | 12.5 (0.5) | 7.4 (0.3) | 6.4 (0.3) | 403,000 | 403,000 |
| 113-S412 | 0.1 | 120 (17.4) | 69 (10) | 345 (50) | 14.2 (0.6) | 8.5 (0.3) | 7.7 (0.3) | 381,000 | 387,809 |
| 113-S321 | 0.5 | 120 (17.4) | 69 (10) | 345 (50) | 14.2 (0.6) | 8.4 (0.3) | 7.7 (0.3) | 170,000 | 195,000 |
| 113-S323 | 0.1 | 150 (21.8) | 69 (10) | 345 (50) | 17.8 (0.7) | 10.4 (0.4) | 10.0 (0.4) | 160,000 | 170,000 |
| 113-S312 | 0.5 | 150 (21.8) | 69 (10) | 345 (50) | 17.8 (0.7) | 10.7 (0.4) | 9.6 (0.4) | 64,000 | 77,000 |
| 113-S311 | 0.1 | 150 (21.8) | 110 (16) | 436 (63) | 17.8 (0.7) | 9.7 (0.4) | 8.8 (0.3) | 170,000 | 171,815 |
| 113-S421 | 0.5 | 150 (21.8) | 110 (16) | 436 (63) | 17.8 (0.7) | 9.7 (0.4) | 9.2 (0.4) | 80,000 | 82,000 |
| 113-S511 | 0.1 | 200 (29.0) | 30(4.4) | 228 (33) | 23.7 (0.9) | -- | -- | -- | 85,035 |
| 113-S512 | 0.1 | 200 (29.0) | 30(4.4) | 228 (33) | 23.7 (0.9) | -- | -- | -- | 73,236 |
| 113-S513 | 0.1 | 200 (29.0) | 10(1.5) | 131 (19) | 23.7 (0.9) | -- | -- | -- | 135,225 |

# REFERENCES


Ahmad, J., and Santhosh, U., 2003, "Small Scale Yielding in Fretting Fatigue," *Proceedings of the 9th National Turbine Engine High Cycle Fatigue (HCF) Conference*, Monterey, CA., Published by Universal Technology Corp., Dayton, OH.

Ahmad, J., and Santhosh, U., 2004, "On Stress Singularity at Contact Boundaries and Application to Fretting Fatigue," submitted for publication.

Anton, D.L., 1999, "Simultaneous Fretting and Fatigue of α/β Ti-6Al-4V," *4th National Turbine Engine High Cycle Fatigue Conference*, Monterey, California.

Antoniou, R.A. and Radtke, T.C., 1997, "Mechanisms of Fretting-Fatigue of Titanium Alloys," *Materials Science and Engineering*, Vol. A237, pp. 229-240.

Blanpain, B., Mohrbacher, H., Liu, E., Celis, J.P. and Roos, J.P., 1995, "Hard Coatings under Vibrational Contact Conditions," *Surface and Coatings Technology*, Vol. 74-75, pp. 953-958.

Cortez, R., Mall, S., and Calcaterra, J.R., 2000, "Interaction of High-Cycle and Low-Cycle Fatigue on Fretting Behavior of Ti-6-4," *Fretting Fatigue: Current Technology and Practices, ASTM STP 1367*, D.W. Hoeppner, V. Chandrasekaran, and C.B. Elliot, Eds., American Society for Testing and Materials, West Conshohocken, PA.

Donachie, M.J., 2000, *Titanium: A Technical Guide,* Second Edition, ASM International, Materials Park, OH.

Dowling, N.E., 1999, *Mechanical Behavior of Materials,* Second Edition, Prentice-Hall, Upper Saddle River, NJ.

Dunyak, T., 1999, U.S. Air Force High Cycle Fatigue Program Database.

Eylon, D., 1998, "Summary of the Available Information on the Processing of the Ti-6Al-4V HCF/LCF Program Plates," University of Dayton, Dayton, OH.

Farris, T.N., Harish, G., McVeigh, P.A. and Murthy, H., 2000, "Prediction and Observation of Fretting Fatigue of Ti-6Al-4V Subjected to Blade/Disk Type Contacts," *Proceedings of the 5th National Turbine Engine High Cycle Fatigue (HCF) Conference of CD*, Session 13, 11 pages, Chandler, AZ, March 2000, Published by Universal Technology Corp., Dayton, Ohio.

Fouvry, S., Kapsa, Ph., Vincent, L. and Dang Van, K., 1996, "Theoretical Analysis of Fatigue Under Dry Friction for Fretting Loading Conditions," *Wear*, Vol. 195, pp. 21-34.

Fu, Y., Loh, N.L., Batchelor, A.W., Liu, D., Zhu, X., He, J. and Xu, K., 1998, "Improvement in Fretting Wear and Fatigue Resistance of Ti-6Al-4V by Application of Several Surface Treatments and Coatings," *Surface and Coatings Technology*, Vol. 106, pp. 193-197.

Giannakopoulos, A.E., Lindley, T.C., and Suresh, S., 2000, "Applications of Fracture Mechanics in Fretting Fatigue Life Assessment," *Fretting Fatigue: Current Technology and Practices, ASTM STP 1367*, D.W. Hoeppner, V. Chandrasekaran, and C.B. Elliott, Eds., American Society for Testing and Materials, West Conshohocken, PA.

Glaeser, W.A. and Lawless, B.H., 2001, "Behavior of Alloy Ti-6Al-4V Under Pre-Fretting and Subsequent Fatigue Conditions," *Wear*, Vol. 250, pp. 621-630.

Golden, P.J. and Grandt Jr., A.F., 2004, "Fracture Mechanics Based Fretting Fatigue Life Predictions in Ti-6Al-4V," *Engineering Fracture Mechanics*, Vol. 71, pp. 2229-2243.

Harish, G., McVeigh, P.A., and Farris, T.N., 1999, "The Tribological and Fatigue Performance of Ti-6Al-4V Fretting Contacts," *4th National Turbine Engine High Cycle Fatigue Conference*, Monterey, California.

Hattori, T., Nakamura, M. and Watanabe, T., 2003, "Simulation of Fretting-Fatigue Life by using Stress-Singularity Parameters and Fracture Mechanics," *Tribology International*, Vol. 36, pp. 87-97.

Hills, D.A. and Nowell, D., 1994, *Mechanics of Fretting Fatigue*, Dordrecht, The Netherlands: Kluwer Academic Publishers.

Hoeppner, D.W., and Goss, G.L., 1974, "A Fretting-Fatigue Damage Threshold Concept," *Wear*, Vol. 27, pp. 61-70.

Iyer, K.A. and Mall, S., 1999, "Fretting Fatigue of Ti-6Al-4V Under Variable Amplitude Loading," *4th National Turbine Engine High Cycle Fatigue Conference*, Monterey, California.

Iyer, K. and Mall, S., 2000, "Effects of Cyclic Frequency and Contact Pressure on Fretting Fatigue under Two-Level Block Loading," *Fatigue and Fracture of Engineering Materials and Structures*, Vol. 23, pp. 335-346.

Jaffee, R.I. and Lutjering, G., 1987, "Effect of Microstructure and Loading Condition on Fatigue of Ti-6Al-4V," *Proceedings of the TMS-AIME Annual Symposia on Effect of Microstructure on Fracture Toughness and Fatigue Crack Growth Rate in Titanium Alloys*, Denver, CO.

Johnson, K.L., 1985, *Contact Mechanics*, Cambridge University Press, New York.

Lindley, T.C., 1997, "Fretting Fatigue in Engineering Alloys," *International Journal of Fatigue*, Vol. 19, Supplement Number 1, pp. S39-S49.

Liu Dao-Xin, Tang Bin, Chen Hua, He Jia-Wen, 2001, "$MoS_2$ Composite Films on Ti Alloy Prepared by Ion-Beam-Enhanced Deposition," *Chinese Journal of Nonferrous Metals*, Vol. 11, No. 3, June, pp. 454-60.

Lutynski, C., Simansky, G. and McEvily, A.J., 1982, "Fretting Fatigue of Ti-6Al-4V Steel," *Materials Evaluation Under Fretting Conditions, ASTM STP 780*, American Society for Testing and Materials, pp. 150-164.

Lykins, C.D., Mall, S. and Jain, V, 2000, "An Evaluation of Parameters for Predicting Fretting Fatigue Crack Initiation," *International Journal of Fatigue*, Vol. 22, pp. 703-716.

Martinez, S.A., Sathish, S., Blodgett, M.P., and Shepard, M.J, 2003, "Residual Stress Distribution on Surface-treated Ti-6Al-4V by X-ray Diffraction," *Experimental Mechanics*, Vol. 43, No. 2, June, pp. 141-147.

MILHDBK, 2003, *Military Handbook: Metallic Materials and Elements for Aerospace Vehicle Structures*, MIL-HDBK-5G, 2 Vols., U.S. Department of Defense, MIL-HDBK-5 Coordination Activity, Wright-Patterson AFB, OH.

Mindlin, R.D., 1949, "Compliance of Elastic Bodies in Contact", *ASME Journal of Applied Mechanics*, Vol. 16, pp. 259-268.

Naboulsi, S. and Mall, S., 2003, "Fretting Fatigue Crack Initiation Behavior using Process Volume Approach and Finite Element Analysis," *Tribology International*, Vol. 36, pp. 121-131.

Nakazawa, K., Sumita, M. and Maruyama, N., 1992, "Effect of Contact Pressure on Fretting Fatigue of High Strength Steel and Titanium Alloy," *Standardization of Fretting Fatigue Test Methods and Equipment, ASTM STP 1159*, M. Helmi Attia and R. B. Waterhouse, Eds., American Society for Testing Materials, Philadelphia, pp. 115-125.

Namjoshi, S.A, Mall, S. and Jain, V.K., 2002, "Effects of Shot-Peening on Fretting-Fatigue Behavior of Ti-6Al-4V," *Journal of Engineering Materials and Technology*, Vol. 124, No. 2, pp. 222-8.

Namjoshi, S.A, Mall, S., Jain, V.K. and Jin, O., 2002, "Fretting Fatigue Crack Initiation Mechanism in Ti-6Al-4V," *Fatigue and Fracture of Engineering Materials and Structures*, Vol. 25, pp. 955-964.

Neu, R.W., Pape, J.A. and Swalla, D.R., 1999, "Methodologies for Linking Nucleation and Propagation Approaches for Predicting Life under Fretting Fatigue," *Fretting Fatigue: Current Technology and Practices, ASTM STP 1367*, D.W. Hoeppner, V.

Chandrasekaran, and C.B. Elliot, Eds., American Society for Testing and Materials, West Conshohocken, PA.

Nicholas, T., Hutson, A., John, R. and Olson, S., 2003, "A Fracture Mechanics Methodology Assessment for Fretting Fatigue," *International Journal of Fatigue*, Vol. 25, pp. 1069-1077.

Nix, K.J. and Lindley, T.C., 1985, "The Application of Fracture Mechanics to Fretting Fatigue," *Fatigue and Fracture of Engineering Materials and Structures*, Vol. 8, No. 2, pp. 143-160.

Pape, J., 1997, "Design and Implementation of an Apparatus to Investigate the Fretting Fatigue of PH13-8 Mo Stainless Steel," M.S. Thesis, Georgia Institute of Technology, Atlanta, GA.

Pilkey, W.D., 1997, *Peterson's Stress Concentration Factors*, 2nd ed., John Wiley & Sons, Inc.

Prevey, P.S., Gabb, T.P., Telesman, J. and Kantzos, P., 2002, "Surface Enhancement of Metallic Materials," *Advanced Materials and Processeses*, Jan., pp. 69-72.

Ruiz, C., Boddington, P.H.B. and Chen, K.C., 1984, "An Investigation of Fatigue and Fretting in a Dovetail Joint," *Experimental Mechanics*, Vol. 24, No. 3, pp. 208-217.

Shepard, M.J., Prevey, P.S. and Jayaraman, N, 2003, "Effects of Surface Treatment on Fretting Fatigue Perfomance of Ti-6Al-4V," *Proceedings of the 8th National Turbine Engine High Cycle Fatigue (HCF) Conference*, April 14-16, Monterey, CA.

Suresh, S., 1998, *Fatigue of Materials*, 2nd Ed., Cambridge University Press, New York, NY.

Swalla, D.R., 2002, unpublished data.

Swalla, D.R., 2003, "Microstructural Characterization of Titanium Alloys with Fretting Damage," Ph.D. Dissertation, Georgia Institute of Technology, Atlanta, GA.

Szolwinski, M.P. and Farris, T.N., 1996, "Mechanics of Fretting Fatigue Crack Formation," *Wear*, Vol. 198, pp. 93-107.

Szolwinski, M.P, Harish, G., Farris, T.N. and Sakagami, T., 1999, "In-situ Measurement of Near-surface Fretting Contact Temperatures in an Aluminum Alloy," *Journal of Tribology*, Vol. 121, no. 1, pp. 11-19.

Van Stone, R.H., Lawless, B.H., Hartle, M., Slavik, D.C., and Gilbert, M.S., 1999, "HCF Fretting in Ti-6Al-4V," *4th National Turbine Engine High Cycle Fatigue Conference*, Monterey, California.

Vingsbo, O. and Soderberg, D., 1988, "On Fretting Maps," *Wear*, Vol. 126, pp. 131-147.

Walker, K, 1970, "The Effect of Stress Ratio during Crack Propagation and Fatigue for 2024-T3 and 7075-T6 Aluminum," *Effects of Environment and Complex Load History on Fatigue Life*, ASTM STP 462, American Society for Testing and Materials, West Conshohoken, PA, pp. 1-14.

Wallace, J.M., 2001, "Fretting Fatigue Crack Nucleation in Ti-6Al-4V," M.S. Thesis, Georgia Institute of Technology, Atlanta, GA.

Wallace, J.M. and Neu, R.W., 2003, "Fretting Fatigue Crack Nucleation in Ti-6Al-4V," *Fatigue and Fracture of Engineering Materials and Structures*, Vol. 26, pp. 199-214.

Waterhouse, R.B., 1992, "Fretting Fatigue," *International Materials Reviews*, Vol. 37, No. 2, pp. 77-97.

Waterhouse, R.B. and Lindley, T.C., Eds., 1994, *Fretting Fatigue*, European Structural Integrity Society Publication Number 18. London: Mechanical Engineering Publications Ltd.

Wharton, M.H. and Waterhouse, R.B., 1980, "Environmental Effects in the Fretting Fatigue of Ti-6Al-4V", *Wear*, Vol. 62, pp. 287-297.